Title

Outer Forearc Dynamics Offshore Costa Rica From 3d Seismic Imaging: Challenging Long Held Assumptions Of Non-Accretionary Convergent Margins

Author

Edwards, Joel Hunter

Publication Date

2018

UNIVERSITY OF CALIFORNIA
SANTA CRUZ

OUTER FOREARC DYNAMICS OFFSHORE COSTA RICA FROM 3D SEISMIC IMAGING: CHALLENGING LONG HELD ASSUMPTIONS OF NON-ACCRETIONARY CONVERGENT MARGINS

A dissertation submitted in partial satisfaction
of the requirements for the degree of

DOCTOR OF PHILOSOPHY

in

EARTH SCIENCES

by

Joel H. Edwards

December 2018

The Dissertation of Joel H. Edwards is approved:

Professor Eli A. Silver

Jared W. Kluesner

Professor Emily Brodsky

Professor Susan Schwartz

Lori Kletzer
Vice Provost and Dean of Graduate Studies

List of Figures

List of Tables

Abstract

OUTER FOREARC DYNAMICS OFFSHORE COSTA RICA FROM 3D SEISMIC IMAGING: CHALLENGING LONG HELD ASSUMPTIONS OF NON-ACCRETIONARY CONVERGENT MARGINS

JOEL H. EDWARDS

Understanding the links between subducting slabs and upper-plate dynamics is a longstanding goal in the field of tectonics. Upper-plate dynamics are thought to result from processes that drive forearc growth or recession, which are important for understanding the evolution of the continental crust, recycling of fluids, petrogenesis of arc magmatism and earthquake nucleation and propagation. However, where converging plates first meet at subduction zones are marine environments, limiting data collection density and resolvability. Costa Rica, a relatively well-studied convergent margin, is thought to be in a state of recession, where erosion and removal of the underside of the forearc dominates and causes forearc retreat. Recently collected 3D seismic reflection data offshore the Osa Peninsula, Costa Rica, yields a rare opportunity to assess this model and to characterize the internal structure of the outer forearc and underthrusting plate of a subduction zone. This dissertation investigates the Pleistocene to present evolution of the outer forearc and the in situ properties of the megathrust. Chapter 2 utilizes sequence stratigraphy methods to extract Pleistocene vertical motions across the slope and shelf and finds that the timing and rates of these motions conflict with the commonly accepted model of continuous subsidence tied to basal erosion. Importantly, Chapter 2 demonstrates that the outermost forearc has not migrated landward during the Pleistocene as previously proposed. Chapter 3 is a study of the geometry and physical properties of the megathrust, showing for the first time in situ corrugations and abandonment and reestablishment of the megathrust up-section, which transiently increases roughness and may inhibit earthquake propagation. Chapter 4 quantifies the in situ material exchange between the plates across the outermost 10 km of the forearc and discovers a state of equilibrium where accretive and erosive processes are variable in space but when integrated are approximately balanced. In this accounting, sediment subduction is the dominant process. When scaled up to the length of the forearc, basal erosion cannot wholly account for the observed record of slope subsidence and trench embayment. Collectively, these studies characterize in 3D a margin with characteristics thought to be tied to net forearc erosion but are likely tied to subducting plate dynamic changes and shortening across the forearc. Because this is the first 3D seismic reflection dataset imaging a non-accretionary convergent margin, these results may be indicative of processes ongoing at other margins.

To my parents, for all their love, support and ethusiam.

Acknowledgements

This is a tricky section to write. It has taken 10 years of college to get to this point, and I have had the good luck and fortune of coming across and working with many, many talented people. First off, thank you to anyone who has helped me in any way.

Thank you to my advisors Eli A. Silver and Jared Kluesner, who I am both the last and the first graduate student of. Eli, you have been incredibly patient and supportive and the best and most critical reviewer of my numerous drafts (which many were filled with nonsense). Jared, thank you for looping me into the USGS and their fantastic offshore seismic imaging group and onto many cruises and for the many nudges along the way. You both are incredible scientists and mentors and your guidance has made me a better scientist and person. Thank you.

Thank you to my committee. Emily Brodsky, for including me in the seismology group and for impressing on me the importance of signal processing and first principles. Casey Moore, for your enthusiasm and incredible intellect on all things subduction zones. Susan Schwartz, for discussions on Costa Rica.

Thank you to all fellow undergraduate and graduate students over the years. The social support and general care and concern you have given me made this doable. Thank you to my USGS cubicle mates out in “cube-land”, those water cooler discussions looking out on the railroad tracks broke up many longs days. Thank you to all those scientists and crew I voyaged with on the open seas, for the company on those long watches, the philosophical discussions on science and the competition in whatever games were available. Those cruises were formative times.

Thanks to the geology departments at Brigham Young University, University of Nevada-Reno and at University of California, Santa Cruz for all the mentoring and guidance inherit in these programs, particularly the seminars, field trips, course offerings and the opportunities to teach. I'm very lucky these programs exist and to have been included, despite my inadequacies.

This dissertation would not have been possible without the crew and scientists who collected the 3D seismic reflection volume offshore Costa Rica in April / May 2011, well before I started grad school. Thank you to all those involved in that project, especially Nathan Bangs.

Finally, I must thank my parents, Jody and Dave Edwards, and my siblings and many, many nieces and nephews, who have always supported me through undergrad, grad and grad school again. It has been a long and distant path since leaving Iowa 13+ years ago, and you have been cheering me on the whole way.

Published content and contributions

Edwards, Joel H., Kluesner, Jared W., Silver, Eli A., and Bangs, Nathan L. (2018) Pleistocene vertical motions of the Costa Rican outer forearc from subducting topography and a migrating fracture zone triple junction, *Geosphere*, vol. 14, no. 2

Edwards, Joel H., Kluesner, Jared W., Silver, Eli A., Brodsky, Emily E., Brothers, Daniel S., Bangs, Nathan L., Kirkpatrick, James D., Wood, Ruby, and Okamoto, Kristina (2018) Corrugated megathrust revealed offshore from Costa Rica, *Nature Geoscience*, vol. 11, pg. 197-202

Edwards, Joel H., Lauer, Rachel, Kluesner, Jared W., Silver, Eli A., Bangs, Nathan L., Boston, Brian, A balanced Costa Rican margin: blurring the lines between accretionary and erosional margins, *Geology* (in prep)

Chapter 1. Introduction

Convergent margins (CMs; Scholl and von Huene, 2009), where oceanic lithosphere dives underneath neighboring lithosphere, have been classified into one of two types, accretionary and erosional (Figure 1.1; von Huene and Scholl, 1991). Accretionary CMs are those where net accretion (lower plate offscraping) at the deformation front (Seely et al., 1974; Karig and Sharman, 1975) or underplating at depth (Kimura et al., 2010) effectively recycle upper plate magmatism allowing the CM to grow over million year timescales (Moore and Silver, 1987), whereas erosional (or non-accretionary) CMs are those where the upper plate recedes (Rutland, 1971) by frontal prism removal (Ranero and von Huene, 2000) and / or basal erosion of the underside of the upper plate (von Huene et al., 2004). Estimates of the global distribution of non-accretionary versus accretionary CMs vary, but some studies suggest up to 75% of CMs are non-accretionary and only 25% are accretionary (Scholl and von Huene, 2009; Stern, 2011), making tectonic erosion a more important process in the evolution of CMs. (Clift et al., 2009). However, as will be briefly discussed in this introduction, there are many assumptions that go into the non-accretionary model, and much of this dissertation will explore whether such assumptions are valid in light of new 3D imaging and recent IODP drilling offshore southern Costa Rica (a CM widely considered to be an end-member non-accretionary margin).

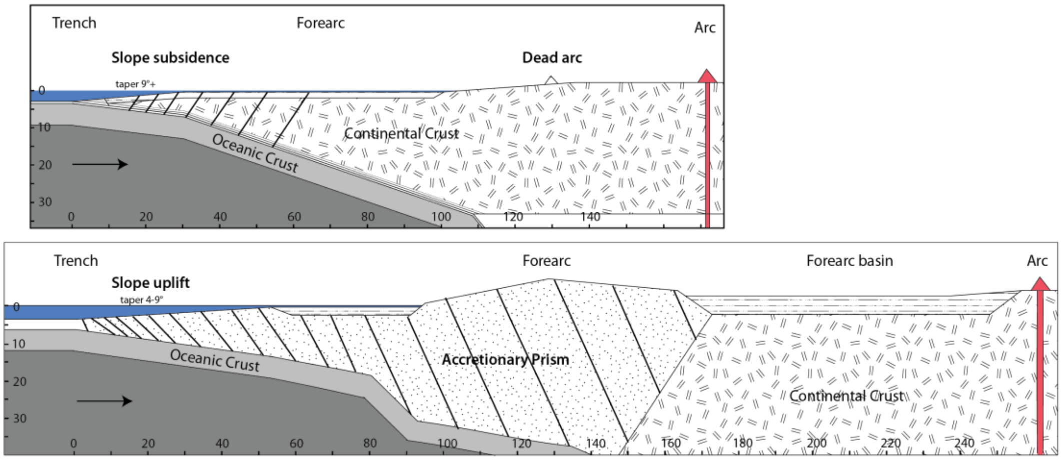

Figure 1.1 Schematic models of erosive- and accretive-type CMs (bottom figure adapted from Calvert, 2004). The top (erosive-type) and bottom (accretive-type) models are drafted after the Costa Rica and Cascadia margins. Note modeled differences, including the trench to arc distance, the presence or absence of an accretionary prism, the geometry of major upper plate structures (landward vs. seaward dipping), the steepness of the dip direction of the subducting plate, the taper of the upper plate and importantly slope subsidence vs. uplift and the resulting forearc basin thicknesses and spatial distribution.

1.1 Non-Accretionary Subduction Zone Model

Non-accretionary (erosive-type) CMs are those margins considered to be undergoing net volumetric crustal loss, and thus should exhibit progressive landward retreat of the outer forearc. However, landward retreat of the outer forearc is difficult to observe over geologic timescales as erosive processes inherently destroy the rock record. Several upper plate processes that can be observed are thought to be linked to a receding upper plate and have been used to categorize large portions of CMs as non-accretionary. Such proxies are briefly described below.

1.1.1 Absence of a Middle Prism

Those CMs that feature continental rock within ~40 km of the trench are considered to be missing a middle prism (Figure 1.1). Middle prisms are defined as significant accumulations of lower plate material accreted to the seaward edge of continents (Scholl and von Huene, 2009). Many margins considered to be lacking a middle prism have, however, frontal prisms, which are described as bodies of landward thickening sediments ~10 – 40 km wide, and are thought to be composed of either accreted lower plate material or shortened slope debris (Scholl and von Huene, 2009). Examples of such CMs thought to be lacking middle prisms include NE Japan (von Huene et al., 1980), Guatemala (Coulbourn, 1982; Aubouin and von Huene, 1985), and Peru (Suess and von Huene, 1988), which all recovered Mesozoic and Paleozoic metamorphosed and crystalline (i.e., continental) rocks along the inner trench wall within ~10 – 15 km of the trench.

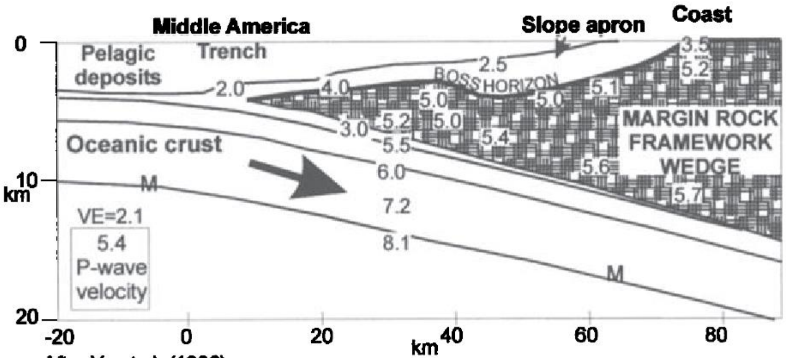

Figure 1.2 Velocity model and interpretation of outer forearc offshore Nicoya Peninsula, Costa Rica from Ye et al., (1996). Model shows an interpreted lack of an accretionary middle prism where the continental framework rock extends to within kilometers of the trench.

1.1.2 Slope Subsidence

Slope subsidence is observed across a significant portion of CMs globally. Slope subsidence is marked by poorly deformed sediments that drape the slope. Slope sediments often overlie a subaerial unconformity, providing a clear net subsidence marker. Slope subsidence is used to estimate net volumetric crustal losses along CMs by assuming a constant subducting plate geometry and overlying wedge taper (Clift and Vannucchi, 2004) that must migrate landward in response to subsidence (Figure 1.3). The method models the landward migration of the trench over some time interval by taking the slope subsidence observed at some point (constrained by drilling) and wholly assigning that subsidence to the landward migration of the outermost wedge (from trench to shelf break typically; Figure 1.3). By quantifying the timing and rate of subsidence, it is then trivial to derive a cross sectional crustal loss that can then be scaled up to a volume by the along strike length of that subsiding CM.

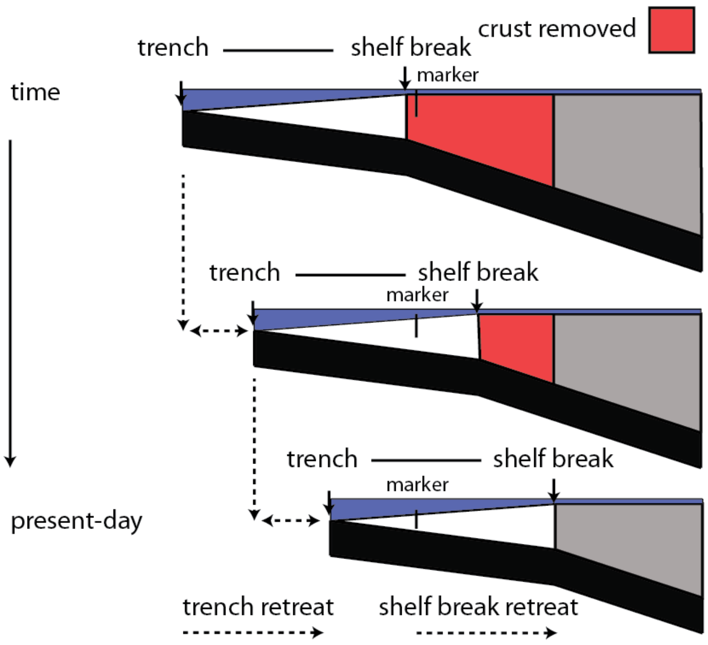

Figure 1.3 Schematic of slope subsidence model modified from (Vannucchi et al., 2003). The model assumes a constant wedge taper and subducting plate dip during slope subsidence, allowing for an easy estimation of net crustal loss (red). Grey regions demarcate the outer edge of the continent, red crustal loss, and white the landward migrating outer wedge.

Huene and Lallemond (1990) first used the method offshore Peru and Honshu (NE Japan) to estimate both volumetric losses / km along strike / my and trench retreat rates. The method has also been applied to >50% of CMs, including Guatemala (Vannucchi et al., 2004), Nicaragua (Clift and Vannucchi, 2004), northern Chile (von Huene and Ranero, 2003) and Tonga (Clift and MacLeod, 1999), resulting in models that approximate global crustal losses due to basal erosion (e.g., Stern and Scholl, 2010).

1.1.3 Landward Deflected Trench

The deflection of the trench axis landward relative to neighboring trench axis trends, also frequently called margin re-entrants, is thought to signify frontal / basal erosion. Such deflections occur over a broad range of along strike length scales, ranging from tens of meters (e.g., recently imaged offshore New Zealand; Bangs, 2018) to hundreds of kilometers (e.g., from offshore Nicoya Peninsula to offshore Osa Peninsula, Costa Rica; Vannucchi et al., 2013). Some reentrants are linked to subducting plate relief (anomalous to surrounding bathymetric depths) that is thought to plow forearc material out of its way, leaving a ‘shadow zone’, or evacuated area, in its wake, thereby deflecting the trench landward (Dominguez et al., 1998). Individual conical seamounts can deflect the trench several km (Ranero and von Huene, 2000) and analogue modeling suggests conical seamounts can entrain lower slope material up to ~2x the volume of the seamount (Dominguez et al., 2000). Aseismic ridges can deflect the trench tens of kms (e.g., Cocos Ridge, up to ~60 km; Ranero and von Huene, 2000). Trench deflections over longer wavelengths have been used to estimate forearc losses by estimating the trench perpendicular and parallel lengths of deflections for both the trench and shelf edge and the thickness of the wedge at the shelf edge and calculating the missing volume (Vannucchi et al., 2013).

1.1.4 Landward Arc Migration

If the geometry of the subducting plate remains constant over time, then the landward migration of an arc (Figure 1.1) is thought to signify basal erosion and overall net crustal recession. Such migration due to basal erosion is thought to have occurred across much of central American, including within northern Costa Rica (Clift and Vannucchi, 2004), Peru (von Huene and Scholl, 1991) and northern Chile (Rutland, 1971; von Huene and Ranero, 2003).

1.2 Accretionary Subduction Zone Model

Accretionary CMs are those which have forearcs that are considered to be growing, or widening, over long time scales, by recycling sediments shed off continents by offscraping those sediments from the lower plate at the deformation front and / or underplating at various forearc depths (Scholl and von Huene, 2009). Because accretion inherently preserves the rock record within the forearc, it was one of the earliest CM forearc processes recognized (Dickinson, 1970), including offshore Cascadia (Silver, 1971). Accretionary CMs are thought to form where relative convergence rates are low (< 50 km / my) and incoming sediment thicknesses are large (> 1 km) and the conveyance occurs over long time scales (>10 my; Clift and Vannucchi, 2004). A diagnostic feature of accretion is a record of slope uplift, particularly at the shelf break, or inner / outer wedge transition. Such uplift results in prominent, long-lived forearc basins (e.g., Aleutians, Cascadia and Barbados).

1.3 Costa Rica Non-Accretionary CM

The Costa Rica CM, with much of the early work focused offshore the Nicoya Peninsula (Buffler, 1982; Aubouin and von Huene, 1985), has been a margin of competing models, with early researchers advocating for both net accretion (Moore et al., 1986; Shipley and Moore, 1986; Shipley et al., 1990; McIntosh and Silver, 1996) and net erosion (Azema et al., 1985). The early debate centered around whether the oceanic crustal rocks observed across the Nicoya Peninsula extended farther seaward toward the trench, predominantly composing the margin wedge, or whether that space is occupied by an accreted mass. Detailed velocity work found high P-wave velocities within ~10 – 15 km of the trench (Figure 1.2; Ye et al., 1996; Stavenhagen et al., 1997), suggesting the edge of basement continental rocks extends to the near the trench. Subsequent drilling results from well site 1042 (within the lower slope ~7 km landward of the trench) recovered carbonate cemented chert-basalt breccia (Kimura et al., 1997b), suggesting kilometers of Neogene slope subsidence. These results seemed to support next CM recession.

Coeval seafloor imaging and seismic reflection profiling across much of central Costa Rica revealed a seafloor littered with seamounts, seamount chains and plateaus, and an inboard continental slope that mimicked the rugged subducting seafloor with seamount scars (von Huene et al., 1995b). Such imaging efforts also revealed that the record of slope subsidence seen offshore Nicoya extended across the entire Costa Rica margin with Miocene to present slope sediments offshore Nicoya and Pleistocene to present slope sediments offshore Osa. This led to a broadening of the erosive interpretation to across the entire Costa Rica margin (Ranero and von Huene, 2000).

However, recent drilling (IODP Exp. 334 and 344; Vannucchi et al., 2011; Harris et al., 2013a) efforts inboard of the NW shoulder of the Cocos Ridge within southern Costa Rica penetrated the margin wedge at well sites U1379 (outer shelf; Vannucchi et al., 2012) and U1380 (upper slope; Harris et al., 2013d) and recovered

Pliocene sediments, not continental framework rock. If ophiolites variably exposed across the Osa Peninsula do not extend seaward towards the trench, is that space then composed of accreted materials?

Costa Rica has all of the major forearc proxies thought to be linked to basal erosion, including 1) continental rocks near the trench (possibly offshore Nicoya; Ye et al., 1996), 2) widespread slope subsidence (throughout the Neogene (Ranero and von Huene, 2000), 3) landward deflection of the trench (von Huene et al., 2000) and 4) arc migration (Cordillera Aguacaste to Cordillera Central; Marshall et al., 2003). Yet confidently resolving whether the forearc has been under a state of net growth or recession, has remained remarkably elusive, considering all the onshore and offshore work to date. Part of this uncertainty is due to the submarine environment, which effectively limits access and data density. However, the 2011 3D seismic volume collected inboard of the NW shoulder of the Cocos Ridge yields up to meter scale horizontal and vertical resolvability across the shelf, slope and subducting plate (Figure 1.4; Kluesner et al., 2013; Bangs et al., 2014). This dataset, coupled with IODP drilling, provides the chance to not only characterize the evolution of the upper plate, but also to examine material exchange in 3D *in situ*.

In the 2nd chapter of this dissertation, I explore the Pleistocene to present day sediments that drape the slope and shelf. Using sequence stratigraphy methods, I extract the vertical motions of the upper plate and the timing of extension and shortening and use those results to dissect the basal erosion model and provide better links to other drivers. In the 3rd chapter, I map the detailed topography of the interface between the upper and lower plates, the megathrust, and end up discovering characteristic slip surface corrugations along well developed and long lived portions of the megathrust. Furthermore, I clearly image both accretionary (at the deformation front) and erosional (along the underside of the frontal prism) processes in situ and image for the first-time, generations of megathrusts. In 4th chapter, I use those mapping results to quantify the exchange of material across the outermost 10 km of the margin (across the frontal prism) and find it to be at an approximate equilibrium.

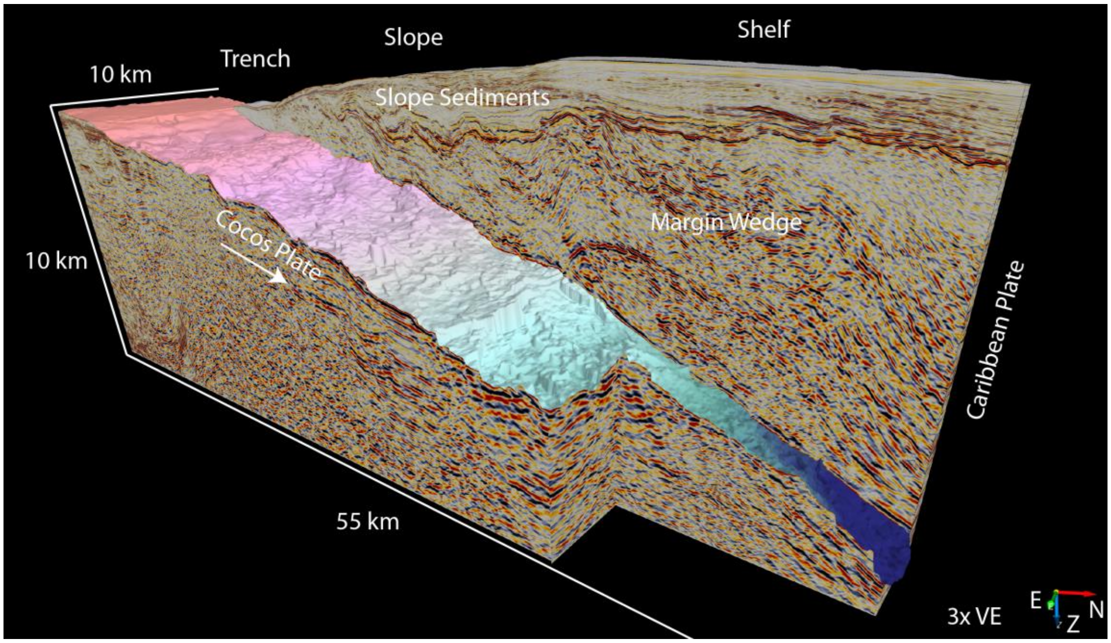

Figure 1.4 Upslope perspective view of the 3D pre-stack depth migrated seismic reflection volume with the upper plate partially removed. Note the internal structure of the margin wedge (deformed but layered) and its most seaward extent (almost to the trench). Also note the thickness of the overlying slope sediments (up to ~2.5 km thickness).

Chapter 2. Pleistocene vertical motions of the Costa Rican outer forearc from subducting topography and a migrating fracture zone triple junction

2.1 Introduction

The Costa Rica convergent margin (CM) is thought to be an end member type erosive margin (von Huene and Scholl, 1991; Ranero and von Huene, 2000; Clift and Vannucchi, 2004), where basal erosion (von Huene et al., 2004) is driving widespread Costa Rican outer forearc subsidence (Hinz et al., 1996; Vannucchi et al., 2013). However, a recently collected 3D seismic reflection volume offshore southern Costa Rica (CRISP seismic experiment; Kluesner et al., 2013; Bangs et al., 2014) reveals structures that conflict with the generic erosional model, showing a margin wedge that is composed of a layered fabric that is pervasively folded and thickened by thrusting. Subsequent IODP drilling successfully penetrated the margin wedge and recovered clastic sediments (Vannucchi et al., 2011; Harris et al., 2013a), consistent with the layered fabric seen in 3D seismic imaging. These results have led some to propose a temporary phase of recent accretion (Bangs et al., 2016) or a new type of CM, a depositionary margin, where extreme, episodic basal erosion removes forearc basement that then drives subsidence and rapid terrigenous sedimentation (Vannucchi et al., 2016).

Reconciling Pleistocene outer forearc subsidence with shortening and thickening offshore Costa Rica requires a detailed investigation into the timing and amounts of outer forearc vertical motions and shortening. For example, work offshore

Honshu found a spatiotemporal link between outer forearc subsidence, backarc spreading and plate kinematic changes (Regalla et al., 2013). Regalla et al., (2013) proposed that changes in the shallow slab geometry could drive outer forearc subsidence. Shallow slab geometry changes can result from two possible mechanisms: (1) an increase in slab effective elastic thickness or (2) a change in slab buoyancy. Both mechanisms can be driven by a change in the convergence rate; specifically, an increase in the convergence rate can either increase the radius of slab curvature or drive negative slab buoyancy, both potentially producing downward flexing of the slab under the outer forearc (Furlong et al., 1982; Buiter et al., 2001; Regalla et al., 2013). Furthermore, although subducting topography can remove and/or tectonically erode the frontal prism and lower slope (Lallemand and Pichon, 1987; Ballance et al., 1989; von Huene and Scholl, 1991; Sak et al., 2004), the effects of subducting topography farther downdip are less known. Analog sandbox models suggest lower slope removal, middle and upper slope uplift, scaled to the size of the subducting feature, and ensuing rapid subsidence (Dominguez et al., 1998). These findings and models provide alternative mechanisms to basal erosion for outer forearc subsidence.

Here we report on a detailed 3D mapping of unconformities and a subdivision of Pleistocene strata into depositional sequences on the southern Costa Rica subduction margin, utilizing the newly collected 3D seismic reflection volume (CRISP) and drilling results from IODP Expeditions 334 and 344. The integration of seismic and well data allow us to temporally constrain sedimentation, vertical motions and shortening (e.g., Ladd and Schroder, 1985). We show evidence for three main mechanisms controlling Pleistocene vertical motions: 1) regional subaerial erosion and rapid subsidence linked to the southeastward Panama Fracture Zone triple junction migration, with associated abrupt bathymetric variations and plate convergence changes, 2) transient, kilometer-scale uplift and subsidence due to inferred subducting plate topography, and 3) outer wedge shortening accommodated by landward- and seaward-dipping thrust faults and fold development due to the impinging Cocos Ridge. Our results underscore the importance of 3D seismic imaging and integration of well data in the documentation and decoupling of complex convergent margin histories.

2.2 Tectonic Setting

Subduction processes offshore Costa Rica likely began during the Late Cretaceous, when andesitic volcanism initiated near the present-day volcanic arc (Lundberg, 1991). The Caribbean Plate is thought to have formed either ‘in situ’ (Frisch et al., 1992) or to the west and then subsequently emplaced piecemeal beginning in the Late Cretaceous and extending through much of the Cenozoic (Burke, 1988; Pindell and Barrett, 1990). The Cocos and Nazca Plates are thought to have their origins from the splitting of the Farallon Plate around ~27 Ma, based on early magnetic and bathymetric studies (Hey, 1977; Lonsdale and Klitgord, 1978), although later work revised this event to ~23 Ma (Lonsdale, 2005). The present-day Cocos Plate is subducting under the Caribbean Plate with a convergence direction approximately normal to the Middle America Trench (MAT) at ~70-90 km/m.y.

(depending on which velocity model is used) and dipping ~19˚ (offshore Osa Peninsula), while the Nazca Plate is moving 37 – 48 km/m.y. to the ENE relative to the Caribbean Plate and is subducting more steeply at ~33˚ (Figure 2.1; Morell 2015; Morell, Fisher, and Gardner 2008; DeMets et al. 1990; Demets et al. 1994; DeMets 2001; Demets, Gordon, and Argus 2010; Kobayashi et al. 2014; Argus, Gordon, and Demets 2011). The Caribbean plate can be subdivided further with its Panama-southern Costa Rica portion referred to as the Panama microplate (Marshall, Fisher, and Gardner 2000), which moves relative to the Caribbean plate at 7.5 km/m.y. to the NE (Kobayashi et al., 2014). From this, Morell (2015) calculated a Cocos-Panama convergence rate of ~70 km/m.y. and a Nazca-Panama convergence rate of ~20 km/m.y.

The differing Cocos and Nazca relative plate motions are accommodated by the north-striking Panama Fracture Zone (PFZ), a distributed right-lateral transform plate boundary with sharp bathymetric steps (Figure 2.1; von Huene et al., 2000). The PFZ transition separates large crustal thickness differences (Sallarès, 2003) and drives lateral offsets of the MAT (Moore and Sender, 1995). The PFZ has been migrating southeastward along the MAT at ~30-55 km/m.y. since the middle Pliocene (Silver et al., 1990; McIntosh et al., 1993; Morell et al., 2008; Morell, 2015). This southeastward migration has been linked to inner forearc shortening (Morell et al., 2008; Morell et al., 2013), outer forearc shortening (McIntosh et al., 1993; Morell et al., 2011), outer forearc uplift (Morell et al., 2011), outer forearc subsidence

(Corrigan et al., 1990), and possibly to the ~2 km high, ~100 km wide and ~150 km long Coiba Ridge, forming as a result of compression (MacMillan et al., 2004).

The Cocos-Nazca spreading center ridge (CNS) generated new crust through three sequential ridge orientations, all while interacting with the existing Galapagos hot spot, which emplaced thick sequences of volcanic rocks on the north and south sides of the ridges (Meschede et al., 1998). This process resulted in the formation of the NE-trending Cocos Ridge (Figure 2.1) and the E-trending Carnegie Ridge (located on the Nazca Plate) (Barckhausen et al., 2001). The Cocos Ridge is a ~2 km high, ~250 km wide and >20 thick NE-trending ridge that extends from the CNS to the MAT and is truncated on its eastern side at the PFZ (Sallarès, 2003), exhibited by an ~2 km bathymetric scarp (Figure 2.1). The Cocos Ridge broadly deflects the MAT landward over ~350 km along strike. The Cocos Ridge is oriented ~10° clockwise from the Cocos-Caribbean relative plate motion vector (~N24E°; Nuvel-1A model), resulting in a slow NW migration of the Cocos Ridge across the MAT with continued subduction (Barckhausen et al., 2001). Timing of the initiation of subduction of the Cocos Ridge is debated, with ages ranging from ~0.5 – 8 Ma (Gardner et al., 1992; Abratis and Worner, 2001); however, recent studies have narrowed in on ~2 – 3 Ma (Morell et al., 2012; Morell, 2015). The Cocos Ridge exhibits strong controls on upper plate deformation processes, including landward deflection of the MAT and increased horizontal velocities (LaFemina et al., 2009), outer forearc uplift (Corrigan et al., 1990; Gardner et al., 1992; Sak et al., 2004; Morell et al., 2011), inner forearc shortening (Fisher et al., 2004; Sitchler et al., 2007), and backarc shortening (Collins et al., 1995).

West of the Galapagos hot spot, oceanic crust generated along CNS results in a dense array of seamounts (~40% of surface area), while Cocos Plate crust generated farther west and north along the East Pacific Rise results in a smoother topography (Figure 2.1; Ranero and von Huene, 2000). The zone of seamounts consists of discrete, conical seamounts up to ~2 km high and ~20 km diameter and broad, flat seamounts and plateaus up to ~2 km high and ~40 km in width (e.g., the Quepos Plateau) (Figure 2.1; von Huene et al., 1995, 2000). The zone of seamounts is estimated to have begun subduction ~3 – 4 Ma (Morell, 2015). Cocos Plate variations outboard of the MAT (i.e., changes in bathymetric roughness and thickness) parallel the along strike changes of the outer forearc (e.g. changes in margin wedge thickness and width, slope continuity and trench geometry; Figure 2.1) (Hinz et al., 1996; Fisher et al., 1998; von Huene et al., 2000; Sak et al., 2009). These variations also parallel tectonic changes (e.g., coastal uplift, fault kinematics, arc migration) within the onshore inner forearc and volcanic arc (Gardner et al., 1992; Marshall and Anderson, 1995; Fisher et al., 1998; Marshall et al., 2000; Gardner et al., 2001; Marshall et al., 2003; Fisher et al., 2004; Sak et al., 2004).

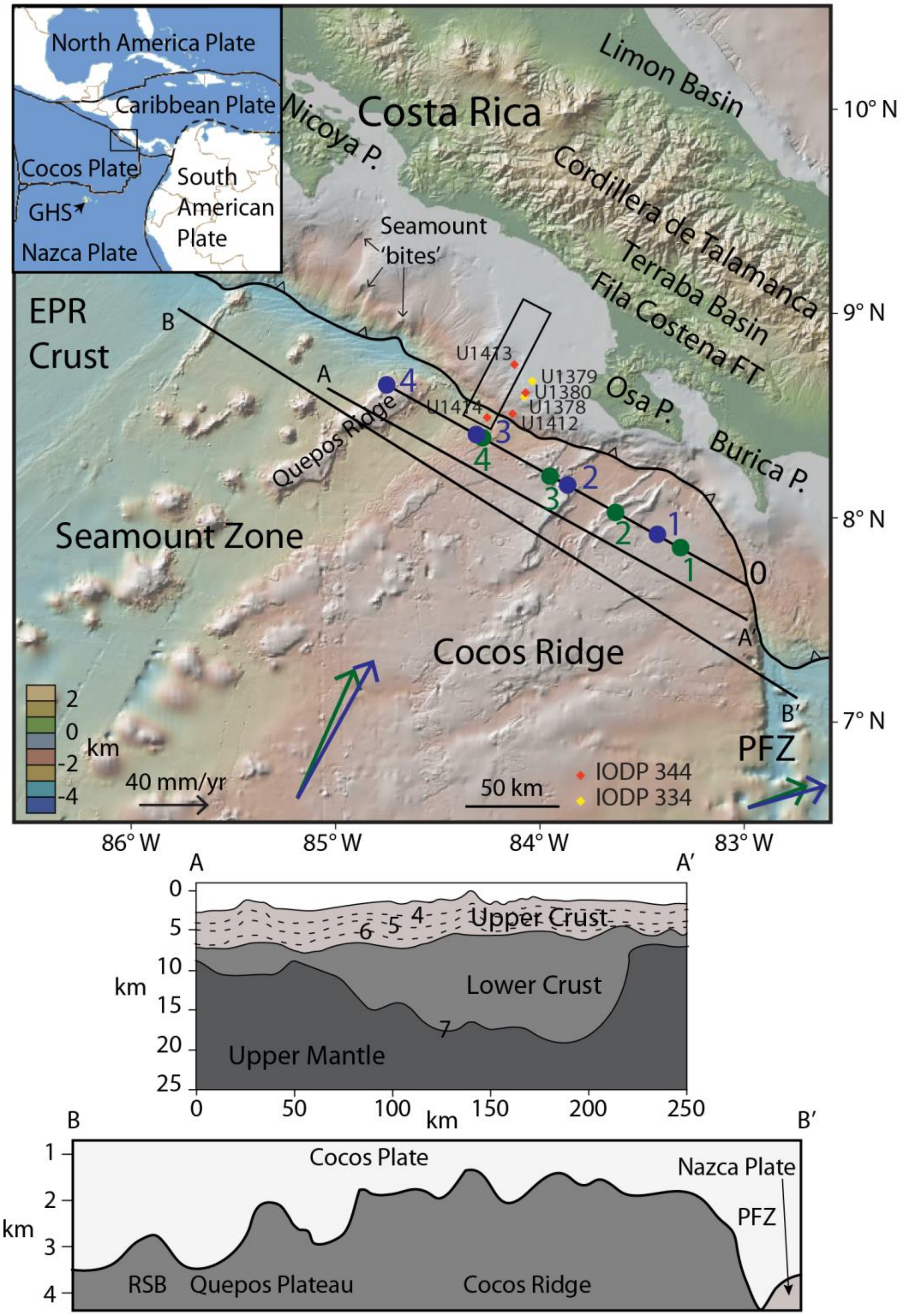

Figure 2.1 Topographic map of Costa Rica convergent margin. Well locations from IODP Expeditions 334 (yellow) and 344 (red) are shown as diamonds. Blue velocity

vectors are based on the NUVEL-1 model and green velocity vectors on the MORVEL model, both relative to the Caribbean plate. Panama Fracture Zone (PFZ) SE migration is shown with rates from NUVEL-1 (blue) and MORVEL (green) models. Subset A is cross section of the Quepos Plateau and Cocos Ridge, modified from Sallares et al., (2003), with seismic velocities overlain. Subset B is a topographic profile of the Quepos Plateau, Cocos Ridge, PFZ and rough smooth boundary (RSB). GHS is Galapagos hot spot. Note the large thickness and abrupt bathymetric changes across the Quepos Plateau, Cocos Ridge and PFZ and the slight clockwise rotation of the Cocos Ridge axis relative to either of the relative plate motion models.

A regionally extensive seismic discontinuity, known offshore the Nicoya Peninsula as the Base of Slope Sediment (BOSS) reflection (Vannucchi et al., 2001), extends across the entire outer forearc offshore Costa Rica (Hinz et al., 1996) and is correlative to the onshore Mal Pais unconformity (Vannucchi et al., 2001). This regional unconformity demarcates a surface along which widespread regional erosion occurred, although not occurring at the same moment in time. The unconformity offshore the Nicoya Peninsula separates an early-middle Miocene margin wedge from an overlying middle Miocene to present sedimentary apron (Kimura et al., 1997a), while offshore the Osa Peninsula, the unconformity separates an Early Pleistocene to Pliocene margin wedge from Early Pleistocene to present slope and shelf sediments (Vannucchi et al., 2011; Harris et al., 2013a). The overlying sediments typically contain a fining upward section, recording deepening water depths (Kimura et al., 1997a; Vannucchi et al., 2011; Harris et al., 2013a). To the SE of the CRISP volume, ~15 km, Vannucchi et al., (2013) found Pliocene deep water sediments overlain by nearshore sediment facies and benthic foraminifera, recording rapid uplift from ~1 km below sea level (bsl) to sea level. The nearshore sediments are then overlain by a fining upward section, recording deepening water depths (Vannucchi et al., 2013). This regional unconformity demonstrates widespread regional surface erosion followed by subsidence.

2.3 Previous seismic reflection studies and IODP drilling

Multichannel seismic reflection data offshore Costa Rica were first collected ~35 years ago (Crowe and Buffler, 1983), followed by Sea Beam multibeam sonar and high resolution water gun seismic reflection (Shipley and Moore, 1986) and limited deep tow seismics (Moore and Shipley, 1988). Many different models were suggested for the internal structure of the forearc margin, including (1) the margin is a sedimentary body with young offscraping (Crowe and Buffler, 1983; Shipley and Moore, 1986), (2) the deformed wedge is much older than the undeformed veneer of sediments and therefore is non-accretionary (Crowe and Buffler, 1983), or (3) the deformed wedge is a result of growing thrust duplexes with the undeformed veneer of sediments protected by roof thrusts (Silver et al., 1985). 2D and 3D seismic reflection data were later collected offshore the Nicoya Peninsula (Stoffa et al., 1991) and these data revealed evidence of possible offscraping at the trench, duplexing and out-of-sequence faulting, large variability in fault spacing and reflector geometry, and young, active faults cutting the sea floor (Shipley et al., 1992; McIntosh and Silver, 1996).

Drilling efforts offshore Costa Rica continued concomitantly with these early bathymetric and reflection studies, with ODP Legs 170 and 205 (Kimura et al., 1997a; Morris et al., 2003). Leg 170 proved especially valuable, revealing that all incoming strata offshore Nicoya were subducted (Kimura et al., 1997a; Silver, 2000), in contrast to previous accretionary margin models (Shipley et al., 1990; Shipley et al., 1992).

Further geophysical investigations included broad 2D multichannel seismic reflection surveys (e.g., SO-76, SO-81 and BGR99) that covered large portions of the Costa Rica convergent margin (Hinz et al., 1996; von Huene et al., 2000; Ranero et al., 2008). These studies revealed information suggesting abundant fluid-flow along the shallow portions of the plate boundary interface within the subduction zone (Ranero et al., 2008), subduction of sparse trench sediments (Ranero and von Huene, 2000), a transitional backstop (von Huene et al., 2000), and spatially episodic accretionary and erosional processes (von Huene et al., 2000).

Recent drilling efforts have focused offshore the Osa Peninsula with IODP Expeditions 334 and 344 (Vannucchi et al., 2011; Harris et al., 2012). IODP Expedition 334 drilled wells along 2D multichannel seismic reflection lines to the southeast of the CRISP 3D volume while IODP Expedition 344 drilled wells within the 3D volume (Figure 2.1), with the exception of a re-entry and deepening of well U1380 from Expedition 334.

IODP Expedition 334 efforts to drill through the sedimentary cover and into the margin wedge within the slope failed; however, Site U1379 (located on the outer shelf in ~125 water depth; Figure 2.1) drilled to ~960 mbsf, penetrating margin wedge material at ~880 mbsf, documenting the entire shelf sedimentary cover sequence (Vannucchi et al., 2011). Site U1379 recovered margin wedge material consisting of early Pleistocene (ca. 2.5 Ma) middle bathyal paleodepth rocks (800-1200 mbsl), exhibited by interpreted forearc basin sediment facies and benthic foraminifer assemblages, overlain by nearshore sediment facies (Vannucchi et al., 2013). Per Vannucchi et al., (2013), rapid uplift, followed by rapid subsidence occurred during Early Pleistocene (~2.5 – 2.0 Ma), subsequent to moderate uplift from ~1.9 Ma to the present (Vannucchi et al., 2013). Sites U1378 and U1380 are located on the upper slope in ~500 m water depths and were drilled to depths of ~500 meters below the seafloor (mbsf). They encountered ~1.5 Ma rocks and sediment facies and benthic foraminifera assemble changes that show abyssal paleodepth rocks (>2000 mbsl), overlain by sequentially shallower paleodepth rocks to the present (Vannucchi et al., 2013). Sites U1378, U1379, and U1380 all encountered generally coarsening sediments down well, with sandy intervals becoming more frequent and more massive with depth (Vannucchi et al., 2011).

Expedition 344 revisited site U1380 from Expedition 334 and extended it to the margin wedge, and drilled two wells within the CRISP 3D seismic reflection volume, Site U1414, located seaward of the trench and on the down-going Cocos Plate, and Site U1413, located within the upper slope (Figure 2.1; Harris et al., 2013a). Site U1414 drilled through the overlying hemipelagic and pelagic sediments and into basalt flows at ~375 mbsf to well bottom at ~465 mbsf (Harris et al., 2013c), documenting the shallowest material being carried into the subduction system. Site U1413 drilled to ~584 mbsf and encountered terrigenous sediments of sedimentary and magmatic origins with grain sizes that generally increase at greater depths, punctuated by turbidite sands, tephras, general mass transport deposits and major benthic foraminifera assemble changes (Harris et al., 2013e). U1380 was extended to ~800 mbsf, encountering terrestrially sourced sediments of similar structure and composition to slope sediments from U1413. U1380 also penetrated ~250 m into the Pliocene margin wedge and encountered sediments similar to margin wedge sediments from Exp. 334 U1379, namely clays and silts with occasional thin sand layers (Harris et al., 2013d).

2.4 Methods

In 2011, we collected an 11 x 55 km^2 3-D seismic reflection data volume offshore the Osa Peninsula (Figure 2.1) to study the subduction thrust zone and processes governing seismogenesis of an erosive convergent margin (Kluesner et al., 2013; Bangs et al., 2014). Seismic reflections were generated using two 27-gun arrays with a separation of 75 m and a 3200 liter displacement operating in flip-flop mode. Data were recorded using four 6 km long streamers spaced 150m apart, resulting in a bin size of 12.5 x 18.75 m with ~60 fold (Bangs et al., 2014). Subsequent processing of the data removed multiples and suppressed noise using standard seismic processing workflows (Yilmaz, 2001). Post stack time migration was then performed. These data were then used to generate a 3D velocity model that was utilized in a full pre-stack depth migration (Bangs et al., 2014). The dataset images the subducting Cocos plate and overlying Caribbean plate down to depths >10 km.

We utilize seismic sequence stratigraphy techniques (Vail and Mitchum, 1977) for stratigraphic interpretation of the young, up to 2.5 km thick, stack of reflections that drape the margin wedge. As such, strata are subdivided into depositional sequences, which are bounded by subaerial unconformities and their correlative marine conformities (Figures 2.2 and 2.3).

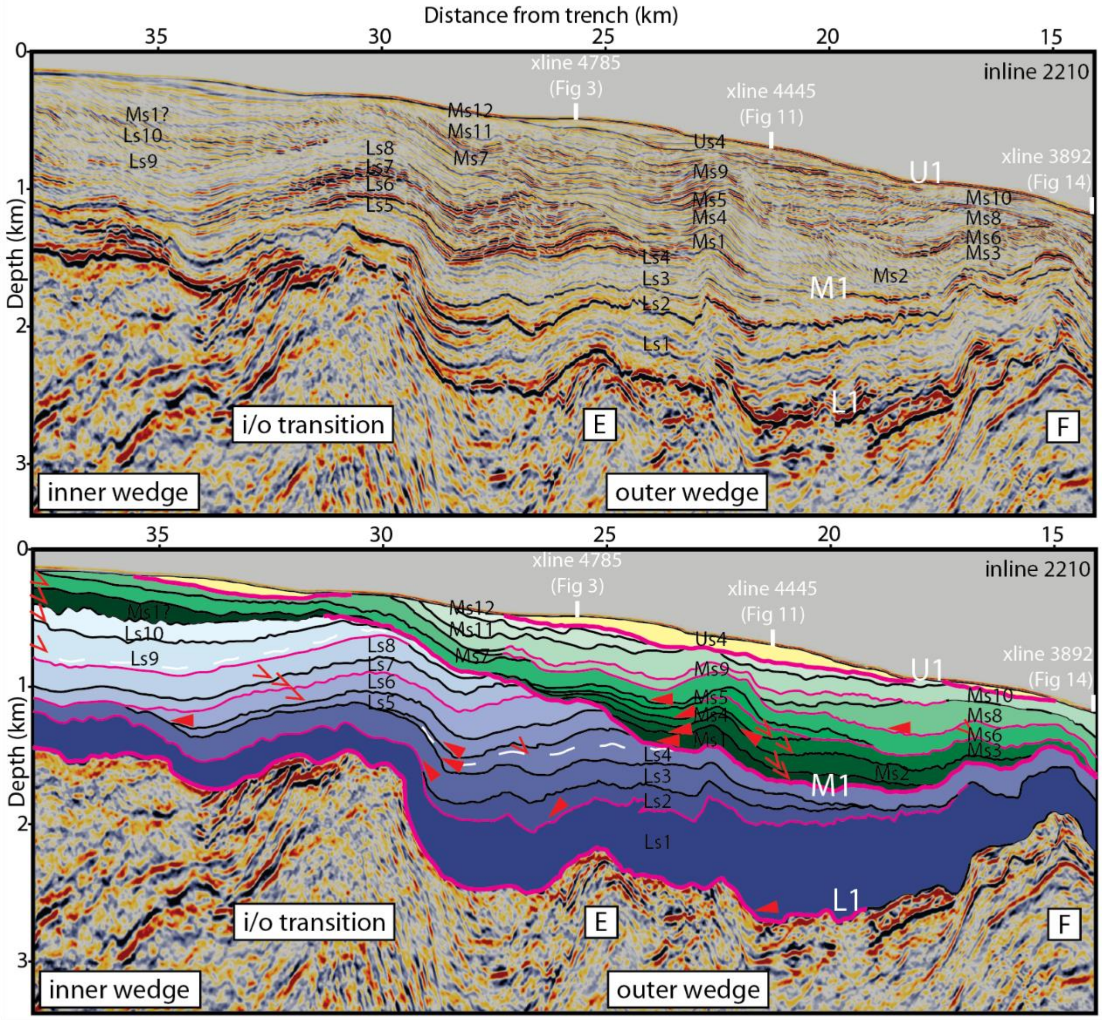

Figure 2.2 Inline 2210 sequence stratigraphy of Pleistocene slope sediments. Top inline 2210 without interpreted sequences overlain. Inline 2210 with interpreted sequences overlain and general structures labeled. Bottom figure is wheeler diagram of sequences (time versus distance parallel to slope) covering 1 – 2.5 Ma. Blue sequences are Lower Strata, green sequences are Middle Strata, and yellow sequences are Upper Strata. Older sequences are darker shades, younger are lighter shades (e.g., Lower Strata depositional sequence 1 is labeled Ls1 and is dark blue and Lower Strata depositional sequence 10 is labeled Ls10 and is light blue). Major erosional

events that separate the stratal domains are shown with thick pink lines and unconformities that truncate underlying strata are shown with thin pink lines. White dashed lines denote maximum flooding surfaces. Solid red arrows denote most seaward point of onlapping clinoforms and open red arrows denote most landward point of downlapping clinoforms, both for individual depositional sequence. Crossline locations from figures 3, 11 and 13 shown for reference. Crosslines increase in number from right to left (landward). Vertical exaggeration (VE) is 3.

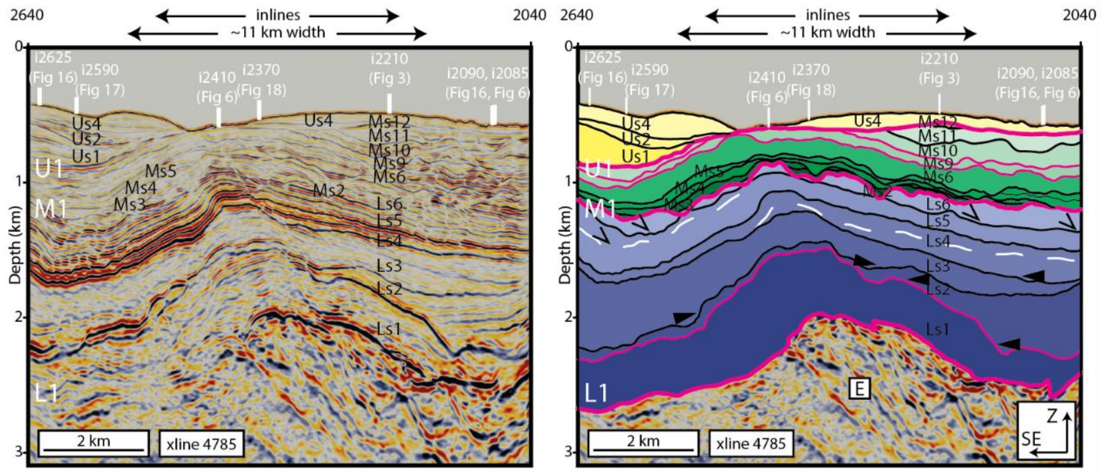

Figure 2.3 Crossline 4785 sequence stratigraphy of Pleistocene slope sediments. Color references, sequence labeling and lines are same as figure 2, with Lower Strata as blue, Middle Strata as green and Upper Strata as yellow. Black solid arrows denote prominent onlapping clinoforms and open arrows denote downlapping clinoforms. Inline locations from figures 3, 6, 16, 17 and 18 shown for reference. Inlines increase in number from right to left (southeast). VE is 3.

We pick the marine correlative conformity in our study as the seafloor at the onset of relative base level fall (Kolla et al., 1995). We describe stratal stacking patterns as one or a combination of the following: upstepping, forestepping, backstepping and downstepping (Figure 2.4). In shallow water environments, these stacking patterns express three types of shoreline shifts: forced regression (forestepping and downstepping), normal regression (forestepping and upstepping) and transgression (backstepping) (Figure 2.4; Catuneanu et al. 2011).

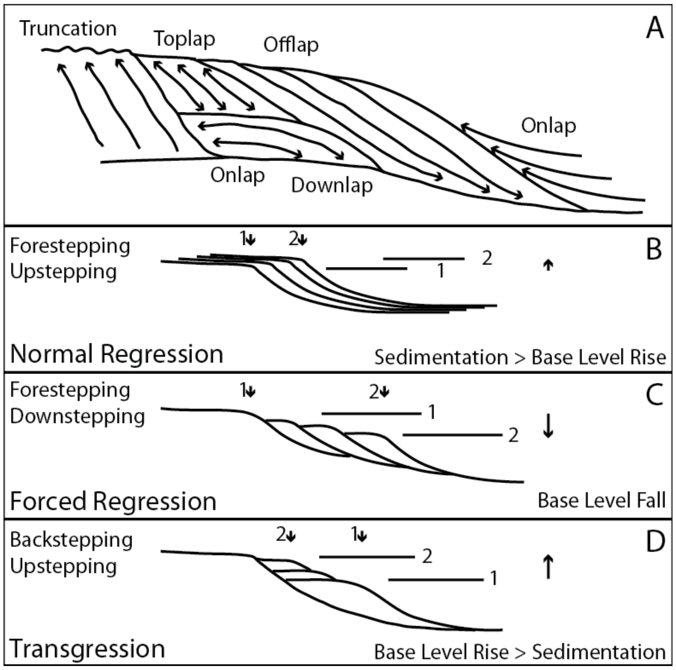

Figure 2.4 Stratal stacking patterns. Inset A is stratal stacking patterns with terminating reflectors and associated naming. Insets B, C and D are normal regression, forced regression and transgression models of shoreline changes (numbers with arrows), stratal stacking patterns and associated naming conventions. Modified from Catuneanu et al., (2011).

Synchronous reflections are thought to represent either stratal surfaces, which follow geologic time lines, or discontinuities, such as unconformities, which signify geologic time gaps (Vail et al., 1977). These stratal or unconformable reflections have low diachroneity in the dip direction of the slope, but can be more diachronous along strike (e.g., the Miocene to Pleistocene regional shelf and slope unconformity that extends across Costa Rica) (Catuneanu, 2002). Diachronous reflections, such as the methane hydrate related bottom simulating reflector, are often fluid-rich interfaces, or can be representative of diagnetic changes, such as the transition from Opal A to Opal C/T (Vail et al., 1977). Fluids, especially gas, can attenuate the acoustic signal and fluid pathways can cause zones of chaotic, low-energy reflections (Loseth et al., 2009). Within the CRISP 3D survey region, there are abundant indicators for fluid-rich zones, fluid migration and seafloor seepage across the slope and shelf (Kluesner et al., 2013) and they limit our ability to map depositional sequences across portions of the data.

The application of seismic stratigraphy methods to deep water settings (e.g., slope) is challenging, especially along the Costa Rican convergent margin, which has high orthogonal convergence rates of 70-90 km/m.y. There is the possibility of physical disconnections between shallow water portions of depositional sequences and their deep-water equivalents, usually due to slope instability and mass transport deposits, which can lead to lateral instead of vertical stacking patterns (Catuneanu et al., 2011). Furthermore, relative base level changes are only seen indirectly in deep water settings, although notable exceptions occur. In spite of these challenges, deep-water sequences can include several important shallow-water equivalent surfaces, including those that form at the points of maximum shoreline regression and transgression (Catuneanu et al., 2011). These deep water equivalent surfaces are mappable in the 3D volume.

We focused our mapping efforts on unconformities and their correlative conformities, referred to as events (e.g., L1, L2, M1, M2, etc.; Figures 2.2 and 2.3), and in mapping them in high resolution (every 5 to 10 crosslines and 5 to 10 inlines). Mapping was performed within OpendTect 6.0.5 seismic interpretation software. This effort resulted in well constrained gridded horizons that show significant detail (e.g., Figure 2.5), such as folding and thrusting (Figures 2.5 and 2.6) and paleo drainage networks (Figures 2.5 and 2.7). Once horizons were mapped, a gridding algorithm was utilized to interpolate between picks and generate 3D surfaces. The gridding algorithm was augmented by a calculated dip-steered volume, which is a 3D volume of local dip and azimuth data for each seismic sample that structurally guides interpolation. Gridded horizons were then examined, exposing mapping errors or inconsistencies, which were then reassessed iteratively. Once satisfactory, we applied a median filter with a 2x2 step-out (inline, crossline) to the gridded horizons to subdue acquisition footprint noise and other gridding artifacts. We then calculated vertical thicknesses between horizons (isopachs) and projected those thicknesses onto the younger horizon (e.g., Figure 2.7). Isopach results were utilized to estimate sedimentation rates during depositional intervals. Note that isopachs are vertical thicknesses, thus if strata are dipping or offset, isopach results will show apparent thicknesses, which are greater than real thicknesses (e.g., some isopach results along the limbs of thrusts A, B, C and D; Figure 2.7). Thus, thickness values used for sedimentation rates are not always maximum observed thicknesses, but are those more closely interpreted to be real thicknesses.

We integrate drilling results from IODP Expedition 344 to the 3D prestack depth migrated volume. Depth imaging allow correlation to U1414 and U1413 magnetostratigraphy, lithostratigraphy, and recovered benthic foraminfera assemblages. Incomplete biostratigraphic data limit some magnetic polarity interval correlation; however, several polarity intervals are well correlated (e.g., the Olduvai

Subchron to the normal polarity section of 480 – 520 mbsf in U1413) (Harris et al., 2013e).

2.5 Results

2.5.1 Shelf and Slope Sediment Stratigraphy

We separate the ~0.7-2.5 km thick shelf and slope sediment stratigraphy into three stratal domains: Lower Strata, Middle Strata, and Upper Strata (Figures 2.2 and 2.3). These stratal domains are separated by three large erosional events: Lower Unconformity 1 (L1), Middle Unconformity 1 (M1), and Upper Unconformity 1 (U1) (Figures 2.5, 2.10 and 2.13). Lower, Middle and Upper Strata are bounded by these three large erosional events and the seafloor (i.e., L1 and M1 bound Lower Strata, M1 and U1 bound Middle Strata and U1 and the seafloor bound Upper Strata). Depositional sequences within each stratal domain are named sequentially upsection, with each depositional sequence number bearing the same number as its underlying sequence boundary number (e.g., L1 (Lower Unconformity) and its overlying Ls1 (Lower Sequence 1), L2 (Lower Unconformity) and Ls2 (Lower Sequence 2), M1 and Ms1, M2 and Ms2, etc.; Figures 2.2 and 2.3).

2.5.1.1 L1 Unconformity

L1 (Figure 2.5) is a regional erosional event that shows a high acoustic impedance contrast, producing a strong, positive polarity reflection that separates the margin wedge from the overlying shelf and slope sediments. L1 is mappable to the landward extent of the CRISP volume, and trenchward to the middle slope, a length of ~35 – 42 km and an area of ~430 km^2, at which point L1 terminates against underlying reflections or is lost due to poor reflectivity between steeply dipping forelimbs of anticlinal thrusts. L1 is unconformable across the shelf, upper slope and partially the middle slope, overlying discontinuous margin wedge reflections and truncating landward- and seaward-dipping margin wedge reflections (e.g., Figures 2.2 and 2.3). Its correlative conformable reflection is observed variably downslope. L1 depths range from ~0.85 – 2.9 km below sea level (bsl; Figure 2.5). IODP drilling results constrain L1 to the Early Pleistocene, ~2.5 Ma (Vannucchi et al., 2011; Harris et al., 2013a).

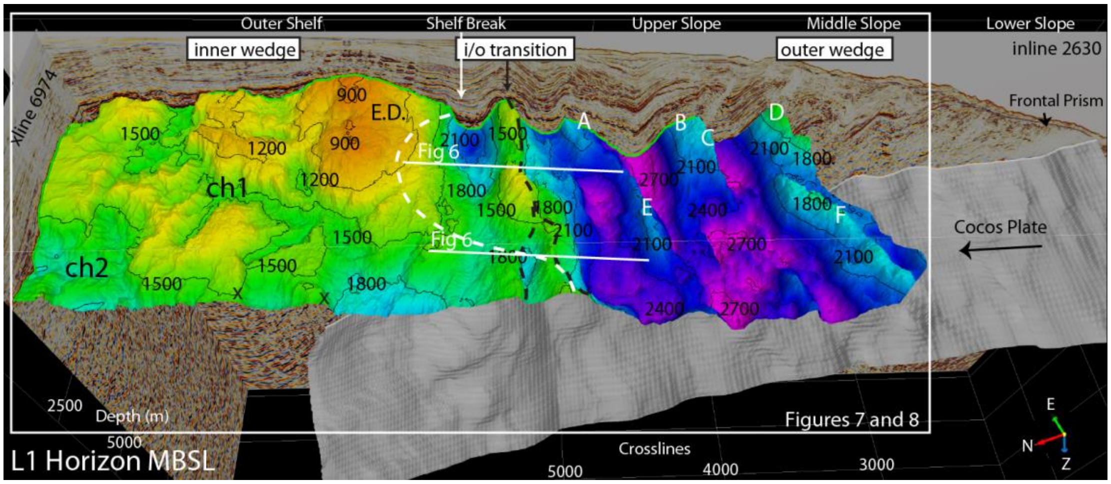

Figure 2.5 The L1 horizon with an oblique perspective view looking southeast. Inline 2630 and crossline 6974 are shown for reference. Colors and labeled contours on CRISPL1 denote meters below sea level (mbsl) and blues to purples are greater depths and greens to yellows to reds are shallower depths. The downgoing Cocos Plate is shown in gray. The two prominent channel systems of the L1 shelf are labeled ch1 and ch2. Middle and upper slope anticlinal thrusts are labeled A – F (G and H are shown with M1 horizon). The dashed black line is the inner/outer wedge transition (i/o transition) and the dashed white line is the projected present day shelf break on the L1 horizon. The eastern dome is labeled as E.D. Two small offset, out of sequence thrusts within the western shelf are labeled as x. Vertical exaggeration is 6. Note the alignment of the present-day shelf break and the eastern dome to the east and the alignment of the shelf break and inner/outer wedge transition to the west.

L1 displays a remarkable topographic contrast between its slope and shelf portions, where it is densely deformed across the slope and is undeformed and channelized across the shelf (Figure 2.5). This contrasting L1 topography marks the inner wedge (limited contractile deformation) and the outer wedge (folded and thrusted; Figure 2.5), analogous to inner and outer wedges seen along other margins (Wang and Hu, 2006). The transition between these wedges is singular and steeply dipping to vertical within the central to eastern portion and distributed (two thrusts) and shallowly landward-dipping to the west (Figures 2.5, 2.6 and 2.7). This transition is coincident with the present-day shelf break along the western portion of CRISP, but deviates from the landward deflected portion of the shelf break, i.e., the scalloped or arcuate shelf bite mark, by up to ~4 km, across the eastern portion of CRISP (Figure 2.5).

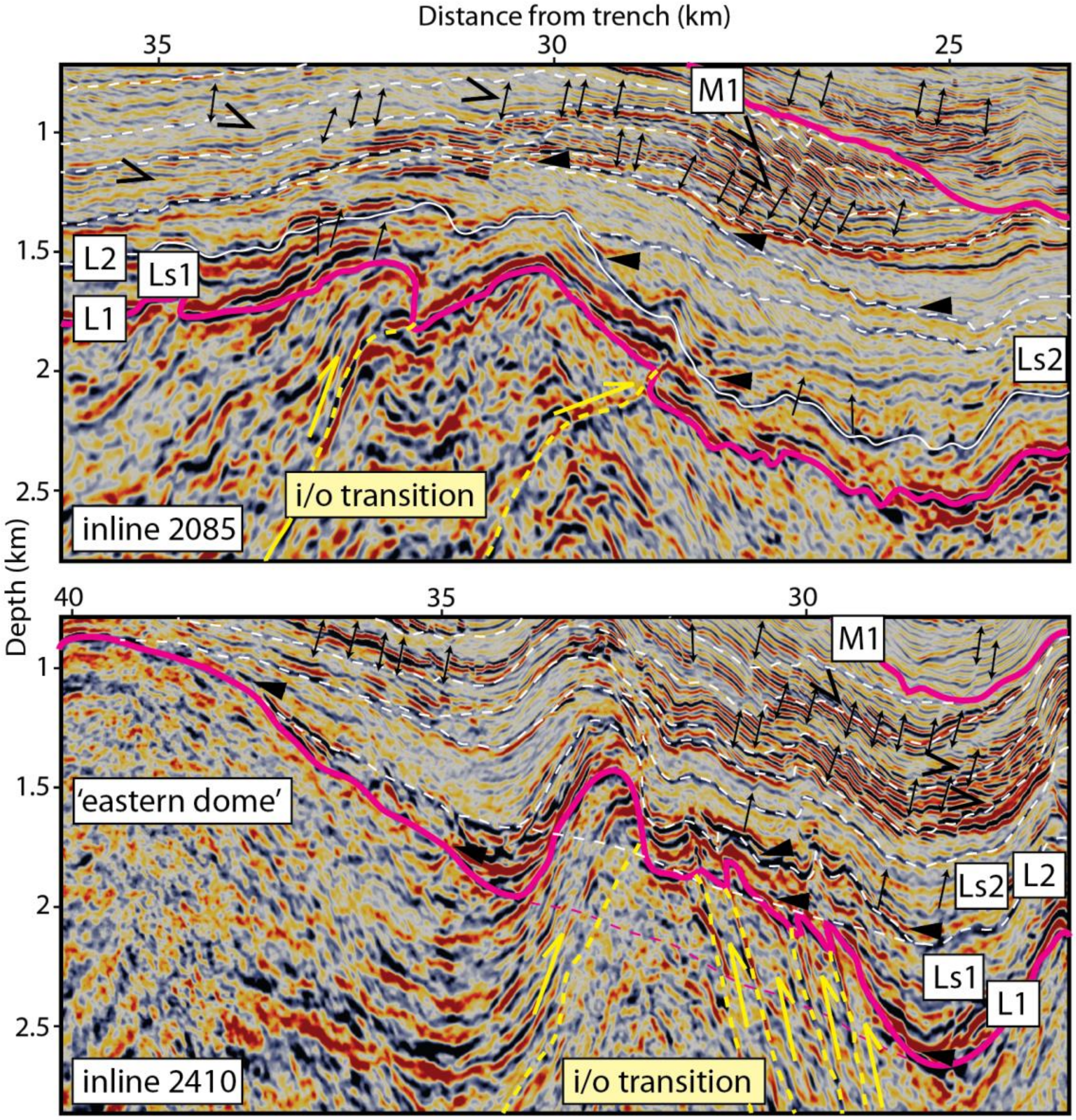

Figure 2.6 Inner / outer wedge transition shown on inlines 2085 and 2410. Thick pink lines denote major erosional events L1 and M1. Dashed yellow lines are prominent thrusts. Solid white line is the L2 unconformity. Dashed white lines are younger lower strata unconformities. Solid black arrows are prominent onlapping clinoforms and open black arrows are downlapping clinoforms. Two sided arrows show normal faults and one side arrows denote depths at which those normal faults terminate. Lower Strata Sequences 1 and 2 (Ls1 and Ls2) are labeled. Note the consistent thickness of Ls1 across the i/o transition at inline 2085 and the thinning of Ls1 up the eastern dome (projected eastern dome slope is shown with thick dashed pink (L1) and white (L2) lines). Vertical exaggeration is 6. Note the thinning Ls2

across the i/o transition within both inlines. Also note the small offsets (<100 m) of normal faults and the depths that they cut to (shallower than L1 and mostly L2).

Two major channel systems are observed across the L1 shelf (Figures 2.5, 2.7 and 2.8). The main channel system, with its tributaries, encompasses >80 km^2, generally trends southwest, and extends >8 km in length adjacent to an old domal uplift, which we refer to as the 'eastern dome' (Figures 2.5 and 2.6). This main channel system cuts to ~500 m depth, relative to adjacent, average L1 depths (Figures 2.5 and 2.7). The other L1 channel system, which occupies the NW corner of the volume and is only partially revealed, encompasses a minimum area of > 16 km^2 and cuts to ~400 m depth (labeled ch2; Figures 2.5 and 2.7). These channel systems feature branching, rugose tributaries with high relief at acute to nearly orthogonal confluence angles (Figure 2.5), in contrast to present-day slope channels with straighter, anastomosing profiles and lower relief (Kluesner et al., 2013). Furthermore, well U1379 from IODP Exp. 334 recovered nearshore sands overlying L1 (Vannucchi et al., 2013). Thus, the observed channel systems likely formed due to fluvial incision and subaerial erosion of a formerly subaerial landscape.

2.5.1.2 Lower Strata Depositional Sequences

Immediately overlying the L1 event, Ls1 onlapping reflectors are observed ~10-15 km downslope from the present-day shelf break (Figure 2.2). These Ls1 onlapping clinoforms backstep to, then against and over the inner/outer wedge transition, transgressing the shelf (Figures 2.2 and 2.6), but do not transgress the 'eastern dome' (Figures 2.6 and 2.7). Ls1 shelf clinoforms transgress landward of CRISP and then upstep until an abrupt seaward shift, L2 (Figure 2.2). Ls1 reaches thicknesses of ~850 m within the slope and ~500 m within the shelf (where L1 channels are filled), which are the largest thicknesses of any Pleistocene depositional sequence, and mark a transgressive succession >36 km in horizontal length (Figure 2.7; greater than the landward extent of CRISP imaging). Ls1 reflectors demonstrate that the 'eastern dome' pre-dates earliest Pleistocene sedimentation and that the inner/outer wedge transition established itself soon after L1, along the eastern portion, and soon after L2, along the western portion (Figures 2.2, 2.6 and 2.7).

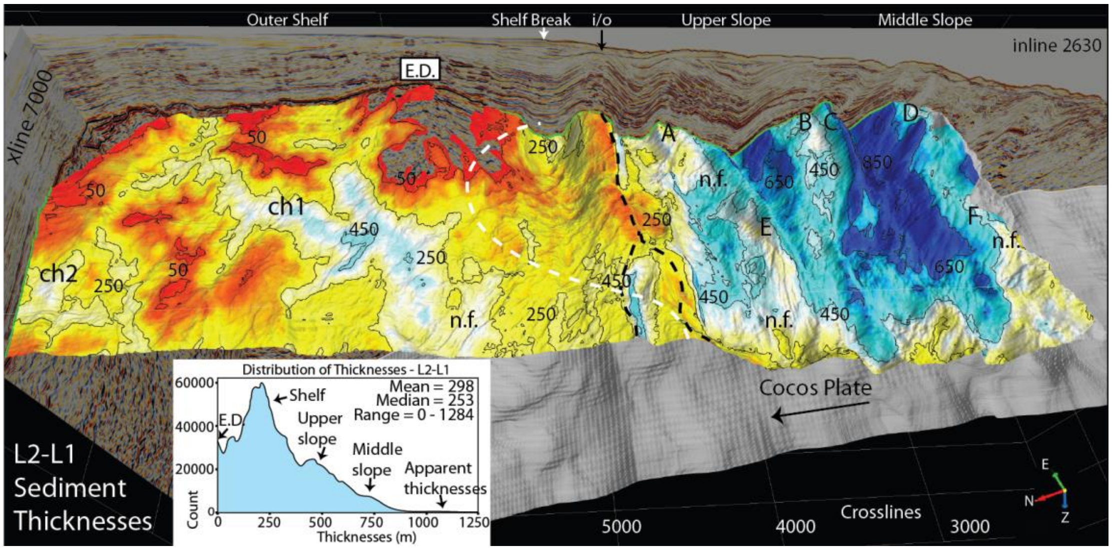

Figure 2.7 L2 to L1 isopach with oblique perspective view looking southeast across the L2 horizon. Inline 2630 and crossline 7000 are shown for reference. Colors and labeled contours on L2 denote calculated vertical thicknesses between L1 and L2 horizons. Color scheme is 'pastel', with whites to blues denote greater thicknesses and yellows to reds smaller thicknesses. Other labels are same as figure 5 (including black dashed line denoting inner/outer wedge transition and white dashed line the shelf break). A histogram of thicknesses is also shown, with mean, median and range of values. Example normal faults, which are seen across the horizon as subtle, parallel, shadowed ridges that vary in geometry, are labeled with 'n.f.' Note the area devoid of Ls1 sediments over the 'eastern dome' (E.D.). Also note the decrease in thicknesses from middle slope to shelf.

Generally, the first half of Lower Strata depositional sequences, Ls1 – Ls6, feature repetitive successions of backstepping clinoforms that build to, against and over the inner/outer wedge transition (except Ls2), until abrupt seaward, or regressive, shifts (Figure 2.2). These early backstepping clinoforms and their equivalent down slope reflections are truncated by the younger M1 slope erosional event, although we see a portion of forestepping and upstepping clinoforms of Ls4 - Ls6 (Figure 2.2). The regressive shifts are interpreted as maximum regressive surfaces at the onset of transgression (i.e., most seaward onlapping reflector) and are measured between this seaward point and their preceding most landward point (often extends landward of survey, thus giving minimum value). Notable regressive shifts are L2, with an ~30 km regressive shift, L4, with an ~25 km regressive shift, and L7 which broadly truncates underlying Ls6 reflectors. The subsequent depositional sequences, Ls7 – Ls10, onlap L7 sequentially across the shelf, with coeval forestepping and upstepping clinoforms across the outer shelf and uppermost upper slope (down slope continuity is obscured due to truncation by M1 unconformity; Figure 2.2). Generally, Lower Strata features a succession of backstepping clinoforms and equivalent down slope/shelf forestepping and upstepping clinoforms that are separated by marked regressive shifts. It is suggested by the coherent vertical stacking patterns, good lateral continuity and large landward transgressions and seaward shifts that Lower Strata backstepping reflectors represent coastal onlap.

Lower Strata stack in patterns consistent with sequence stratigraphy models. At times, rapid Early Pleistocene tectonic subsidence did not outpace sedimentation (e.g., forestepping and upstepping clinoforms of Ls8) and at times subsidence did not outpace eustatic fall (e.g., every abrupt seaward shift and correlative unconformity, L2, L3, L4, etc.). In total, Lower Strata sedimentation produced at least ~1.6 km thick deposits across the middle and upper slope (before major slope erosional events) and ~1.3 km thicknesses across the shelf (Figure 2.8).

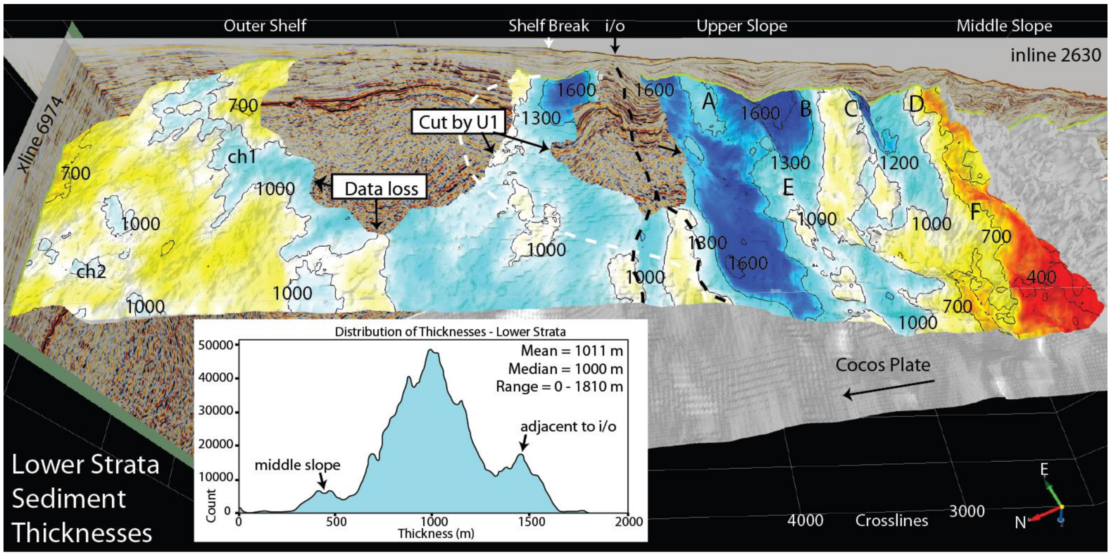

Figure 2.8 Lower strata isopach with oblique perspective view looking SE across the M1 horizon and M1 – L1 isopach values overlain. Inline 2630 and crossline 6974 are shown for reference. Colors and labeled contours on M1 denote calculated vertical thicknesses between M1 and L1 horizons. Color scheme is 'pastel', with whites to blues to denote greater thicknesses and yellows to reds progressively smaller thicknesses. Other labels are same as Figure 7. Note the high isopach values along the flanks of the inner/outer wedge transition, as these values are the most representative of slope Lower Strata thicknesses before the M1 erosional event. Also note how thicknesses decrease downslope, demonstrating the down slope limits of the Lower Strata basin.

During IODP drilling, ~80 m of Lower Strata were encountered at site U1413 and were composed of fine to medium sandstone to conglomerate from ~500 mbsf to well bottom (Figure 2.9). Magnetostratigraphy constrains Lower Strata to the Olduvai subchron and its reversal and older (>1.78 Ma; Harris et al., 2013d). This, coupled with magnetostratigraphy results from wells U1379 (shelf) and U1380 (middle slope) ~15 km to the SE, which date the regional unconformity at 2.2 Ma, constrain Lower Strata to the Early Pleistocene (Harris et al., 2013d; Vannucchi et al., 2013).

Lower Strata stacking patterns are important for several reasons, including: 1) they demonstrate vertical stacking patterns and good along strike continuity, relative to Middle and Upper Strata, 2) the inner/outer wedge transition established itself right after L1 and L2 and continued activity during Lower Strata deposition, 3) the 'eastern dome' is a long lived area of uplift that may represent a pre-L1 shelf break, and 4) even though the slope outpaced the shelf, subsidence was fairly coherent, broad (shelf to at least middle slope) and generally flat-lying (seen by large horizontal regressions and transgressions).

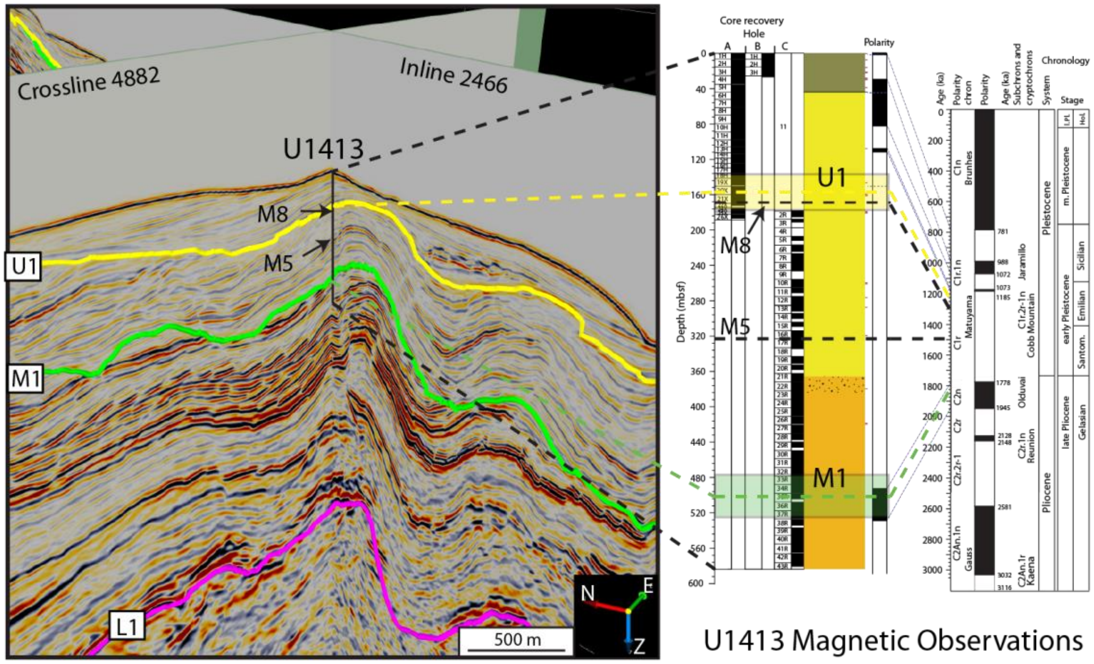

Figure 2.9 Well U1413 shown with inline 2466 and crossline 4882. Well is correlated to lithostratigraphy and magnetostratigraphy results from Proceedings of Integrated Ocean Discovery Program Initial Reports 344. Note that the well intersects both M1 and U1 unconformities.

2.5.1.3 M1 Unconformity

Deposition of Lower Strata was interrupted by the slope M1 erosional event. M1 is a variably reflective event (positive and negative polarity, or absent reflectivity), that truncates Lower Strata and margin wedge material (lower slope) across the entire slope (Figures 2.2, 2.3 and 2.10), and is itself truncated locally updip by the U1 event (Figure 2.10). Its downcutting portion is generally bounded on its landward side by the inner/outer wedge transition, while its correlative conformity extends across the shelf and is gently dipping landward, paralleling shelf strata (Figures 2.2 and 2.10). M1 truncates upper slope Lower Strata down to Ls4 (Figures 2.2 and 2.17), constraining the thickness of material removed to ~900 m. Its upper slope is characterized by linear, sinuous, anastomosing channels and levies that track parallel to the slope and deeply channelize its surface (Figures 2.2.2.3 and 2.10). Its upper slope portion is dipping seaward ~8-10˚ (Figures 2.2, 2.6, 2.16 and 2.17), more than double that of the present-day slope (~3˚). M1 then shallows to sub-parallel the underlying Lower Strata across the middle slope (close to horizontal when not offset), and then cuts down section across the lower slope until it is truncated by the seafloor (Figures 2.2 and 2.16). M1 is mappable down to within ~5-10 km of the trench (is locally obscured due to the BSR), truncating older lower slope landward-dipping thrusted sections (Figures 2.10, 2.14, 2.16 and 2.18). M1 does not truncate tightly imbricated reflections of the frontal prism (Figure 2.16). Generally, its SE middle and upper slope extent is more intensely deformed by folding (Figure 2.10).

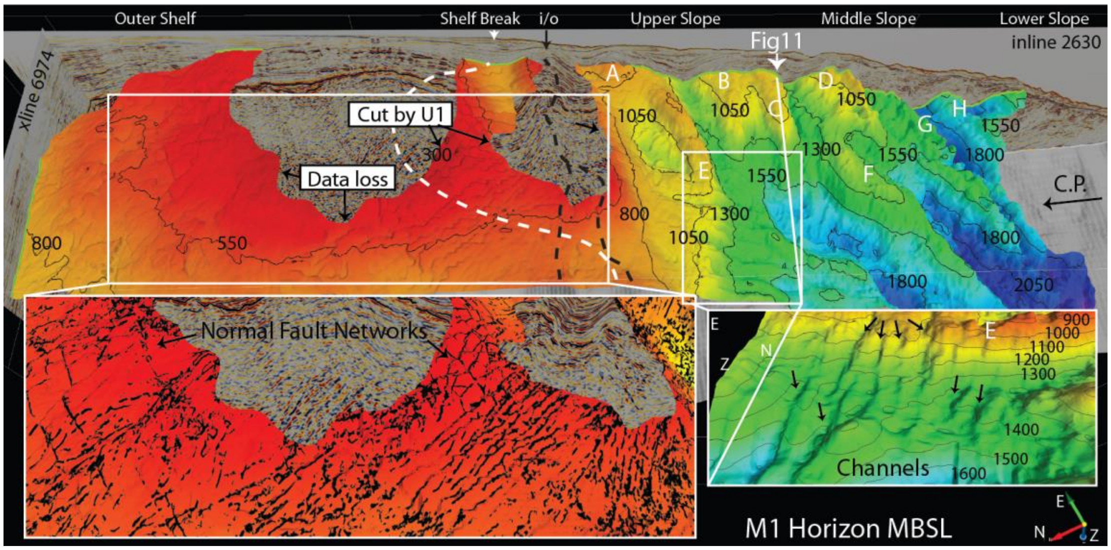

Figure 2.10 M1 unconformity with an oblique perspective view looking SE. Meters below sea level (MBSL) contours and colors (same as figure 5) are overlain. Other labels are same as figure 5 (including dashed black line as inner/outer wedge transition and dashed white line as shelf break). Lower left inset of semblance coefficient values (measure of similarity between traces) calculated with dip steering

(structurally guided) over the outer shelf. Blacker values denote lower semblance (greater dissimilarity). Semblance values are used here to highlight normal fault networks cutting the M1 horizon. Lower right subset is of channels cutting down the upper slope portion of M1, highlighted by shading and by using an upslope perspective view (looking landwards). Note thrusts folds G and H and the orientations of labeled anticlinal folds (WSW-trending).

M1 was intersected by well U1413, at ~500 mbsf, constraining the event to the Olduvai subchron (1.95-1.78 Ma) (Figure 2.9; (Harris et al., 2013e)). No lithology change marks the event; however, a significant benthic foraminifera assemblage change at ~504 mbsf is encountered, with the appearance of Brizalina cf. dilatata below M1 (Harris et al., 2013e).

It is not known whether any portion of the M1 unconformity was formed due to subaerial erosion. It is possible that some portion of the upper slope was subaerial but was then overprinted by intense channelization along a steeply dipping coastal gradient undergoing rapid subsidence. Regardless, the pervasive channelization, steep down cutting and total slope surface erosion (excepting frontal prism) suggest a major slope collapse that removed a thick section of Lower Strata and margin wedge material.

2.5.1.4 Middle Strata Depositional Sequences

Sedimentation following M1 began within the upper/middle slope, where the M1 slope shallows from 8-10° to subhorizontal. Ms1 onlapping reflectors backstep up M1 to within ~6 km of the inner/outer wedge transition while coeval forestepping clinoforms extend ~8 km downslope to the base of a middle slope anticlinal thrust (labeled F; Figures 2.2), before a small abrupt seaward shift (M2; Figure 2.2). The following Ms2 – Ms4 backstep and upstep across M1 landward and coeval clinoforms forestep down slope, with Ms3 extending across anticlinal thrust F (Figure 2.2). These early Middle Strata sequences generally stack vertically and are separated by small seaward shifts. Ms6 reflectors backstep to within ~1 km of the inner/outer wedge transition at which point they transgress the transition and forestepping clinoforms then build over the transition (Figures 2.2). The remaining sequences, Ms7 and Ms9 – Ms12, feature successions of upstepping, levied channels across the upper slope (Figure 2.3) and coeval upstepping and forestepping clinoforms across the middle and lower slope, although upstepping levies, or aggrading channels, are present locally throughout Middle Strata across the entire slope (Figures 2.3, 2.11 and 2.14). Ms8 consists of backstepping clinoforms well seaward of its earlier sequence counterparts (Ms1 – Ms7), backstepping landward until the M9 unconformity (Figure 2.2). Some lateral/seaward shifts are prominent, including M5, which truncates underlying Ms3 and Ms4 reflectors broadly, M8, which truncates Ms6 and Ms7 downslope up to ~15 km from the inner/outer wedge transition, and M9 and M10 (Figures 2.3 and 18). The upstepping portions of all Middle Strata sequences within the upper slope (proximal to the steeply dipping portion of the M1 surface) consist of channels, levies and channel fill (Figure 2.3).

Generally, the earliest Middle Strata sequences, Ms1 – Ms4, consist of successions of channelized backstepping and upstepping reflectors that transgress up the M1 event, with coeval forestepping and sometimes upstepping clinoforms across the middle slope and locally the lower slope (Figures 2.2 and 2.3). Likely, these represent gravity flow and mass transport deposits of a submarine fan complex within the new upper/middle slope basin. The remaining sequences, Ms5 – Ms12, consist of levied channels that often migrate laterally across the slope during stacking, with coeval upstepping, forestepping and sometimes downstepping clinoforms also migrating laterally down slope (Figures 2.2 and 2.3). Offlap is observed where forestepping clinoforms are truncated by channels (see M8 in Figure 2.14). These observations suggest that as the middle/upper slope basin filled, sediments either migrated laterally or traveled over the newly filled sub-basins to lower slope or trench depocenters.

Middle Strata depositional sequences show poor continuity and high variability in thickness along strike (Figures 2.11, 2.12 and 2.14), compared to the relatively continuous and consistent Lower Strata. Ms5 – Ms12 sequences thin and terminate against slope anticlinal thrusts (Figures 2.11 and 2.14), constraining the timing of initiation of many slope folds (Figures 2.11, 2.14, 2.17 and 2.18). Middle Strata thicknesses within the slope reach up to ~1000 m, while shelf thicknesses are obscured due to data loss, but are thought to vary between 0 – 450 m (Figure 2.8).

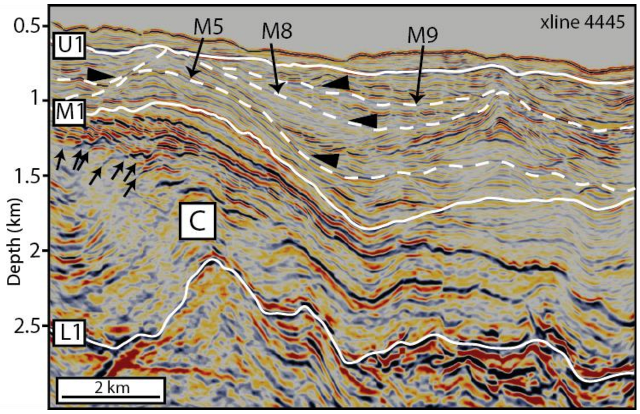

Figure 2.11 Crossline 4445 timing of initiation of fold C after the M5 sequence boundary. L1, M1 and U1 unconformities are shown with solid white lines. Important sequence boundaries are shown with dashed white lines and are labeled. Solid black arrows show onlapping clinoforms. One sided arrows denote base of normal faults, in this case likely associated with folding. Note the earliest onlapping reflectors which onlap M5 along the limb of C, and the continuation of onlapping reflectors upsection. Also note the pervasive channels, levies and channel fill within Middle Strata.

U1413 encountered Middle Strata between 180 mbsf to ~500 mbsf, constraining Middle Strata to the Cobb Mountain reversal and Olduvai sub chrons of the Matuyama chron (~1.78-1.19 Ma and ~1.95-1.78 Ma; Figure 2.9). Assuming a constant rate of sedimentation, we constrain two important Middle Strata unconformities, M5 and M8, to ~1.5 and ~1.35 Ma. Thus, U1413 shows that the bulk of Middle Strata sediments were deposited during the Cobb Mountain reversal (Harris et al., 2013e).

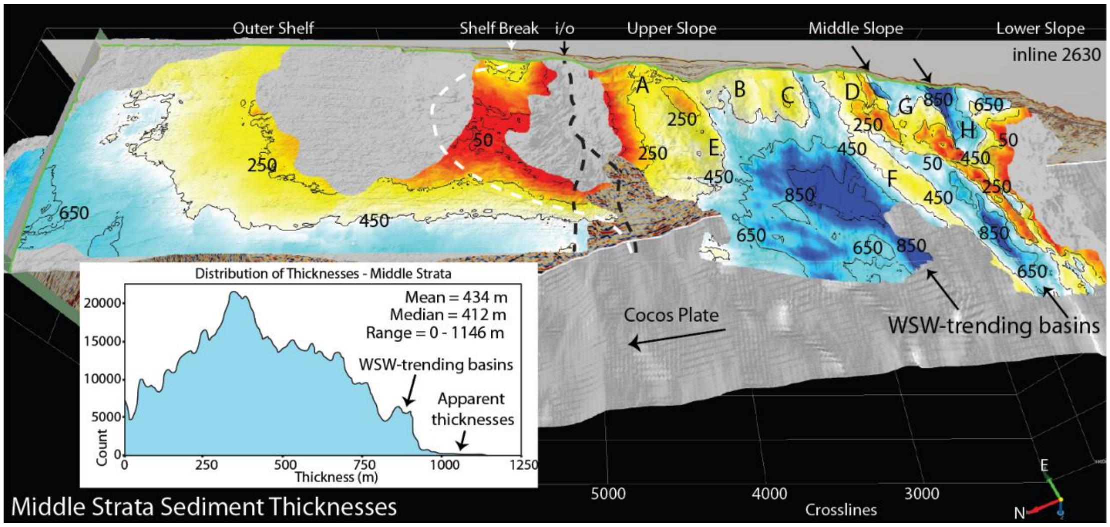

Figure 2.12 Middle strata isopach with oblique perspective view looking SE across the U1 horizon. Inline 2630 and crossline 7000 are shown for reference. Colors and labeled contours on U1 denote calculated vertical thicknesses between U1 and M1 horizons. Color scheme and other labels are same as figure 8. Inset is a histogram of thicknesses, with mean, median and range of thicknesses. Note WSW-trending basins and bounding thrusts. Also note how thicknesses decrease downslope, where more tightly spaced and active thrusting uplift Middle Strata. Lack of isopach results are either due to where U1 truncates M1 or due to data loss and lack of resolvability.

2.5.1.5 U1 Unconformity

Middle Strata deposition was interrupted by the slope U1 erosional event (Figures 2.2, 2.3 and 2.13). The U1 event is also a variably reflective unconformity (positive and negative polarity, or absent reflectivity), and extends from the outermost outer shelf to the lower slope. It is erosive across the entire slope, removing up to ~150 m thicknesses, and its correlative shelf conformity is obscured by data loss (Figure 2.13). The U1 event delineates an unconformity that broadly truncates Middle Strata across the middle and upper slope and Lower Strata across the outermost outer shelf and down the lower slope (via channelization at great water depths). Its most landward erosional extent is coincident with the inner/outer wedge transition to the

NW, and to the SE, is coincident with the ‘eastern dome’ (long lived Pleistocene domal uplift; Figure 2.10). Subhorizontal erosion extends down to at least ~1.1 km bsl and channelized erosion down >1.9 km bsl, to within ~5 km of the trench (Figures 13, 14 and 16).

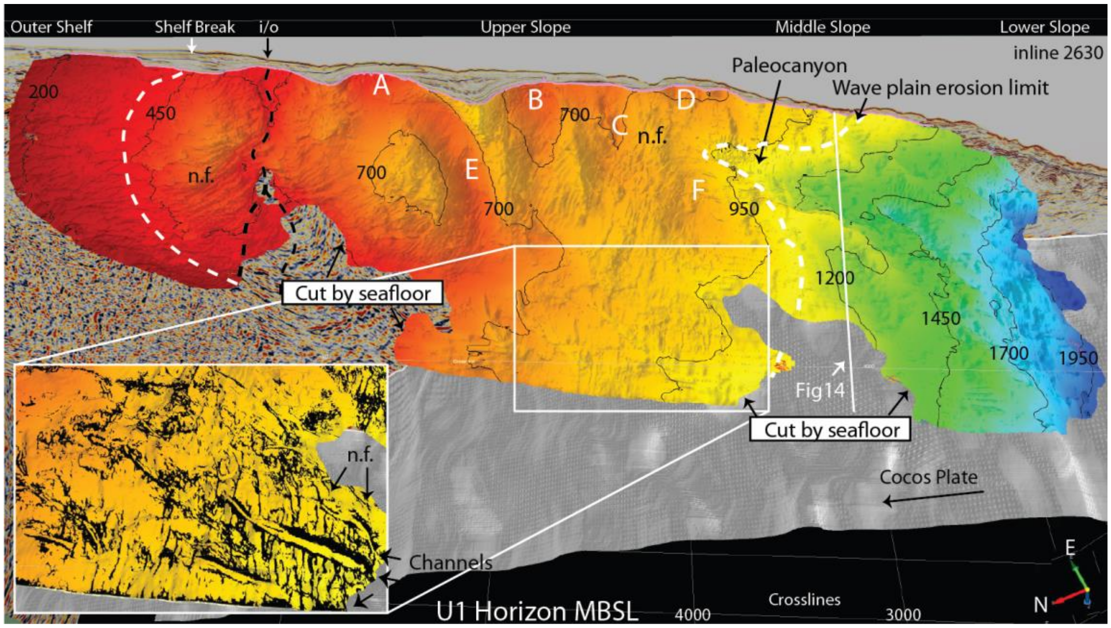

Figure 2.13 U1 unconformity with an oblique perspective view looking SE. Inline 2630 is shown for reference. Colors and labeled contours on U1 denote meters below sea level (mbsl) and blues to purples are greater depths and greens to yellows to reds are progressively shallower depths. Anticlinal thrusts are labeled with white letters. Thick white dashed line across the middle slope denotes the downslope extent of wave plain erosion. Inset is of the western upper slope and displays normal faults (oblique to perpendicular to the slope) and channels (parallel to the slope) by semblance coefficient values. Blacker values denote lower semblance (greater dissimilarity). Note the subtle, parallel shadows with varying orientations, linear to arcuate ridges that strike oblique to perpendicular to the slope and are highlighting by shading. These are small offset normal faults cutting the U1 horizon (some labeled with n.f.). Note the paleo canyon extending downslope from the middle to lower slopes.

U1 3D geometry is broad and subhorizontal, paralleling the present-day seafloor. Its surface is relatively featureless, with subtle, short channels that run generally parallel to the slope. Small offset (<25 m), orthogonal, NW- and NE-striking normal faults cut the U1 event across the upper slope (Figure 2.13). Its eastern upper slope portion is deformed by landward- and seaward dipping anticlinal thrusts (Figures 2.13 and 2.15). Its southeastern middle slope portion is overprinted by a major paleo canyon system that reaches ~350 m in relative depth (measured from bounding wall heights) and extends >7 km in length (Figures 2.13, 2.14 and 2.15). The canyon head is ~600 m wide and significantly widens downslope to beyond the width of the CRISP survey (Figure 2.15). The canyon is bounded by relatively steep walls (~13˚; Figure 2.14).

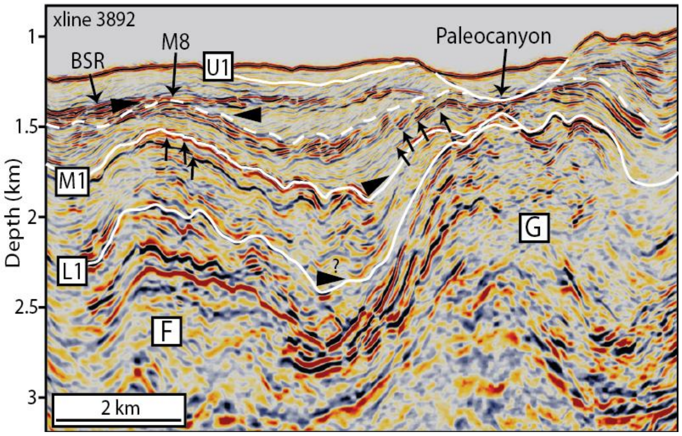

Figure 2.14 Crossline 3892 showing timing of initiation of fold F after M8 and G likely before L1. L1, M1 and U1 erosional events are shown with solid white lines. The M8 unconformity is shown with a dashed white line. Solid black arrows show onlapping reflectors (uncertainty is shown with question mark). One sided arrows denote base of some normal faults, in this case likely associated with folding. Anticlinal thrust G likely initiated before L1 and continued activity through Lower Strata and early Middle Strata. Note the paleo-canyon (down slope extent of U1) cutting Middle Strata.

Considering these observations, it is likely that the U1 unconformity was formed by subaerial erosion, via wave plain erosion or wave scour, extending across an area that now reaches down to ~1.1 km bsl. The paleo canyon system overprints the broad and flat wave plain erosion, and seems to have formed at a transient break, potentially a coastal break, or a paleo shelf break, following subsidence, analogous to many small canyon or channel systems cutting into shelf breaks along Costa Rica (Figure 2.1; von Huene et al., 2000).

2.5.1.6 Upper Strata Depositional Sequences

Upper Strata reflectors begin onlapping ~6-7 km downslope from the inner/outer wedge transition, between landward- and seaward-dipping anticlinal thrusts labeled A and B (Figures 2.3, 2.13, 2.15 and 2.17). These reflectors, labeled Us1, partially fill the synclinal depression until an abrupt seaward shift, designated U2 (Figure 2.17). Subsequent reflectors, labeled Us2, continue to onlap local synclinal basins within the central to eastern portion of the volume (mostly between anticlinal thrusts A and B, C and D) and on both the landward and seaward sides of the inner/outer wedge transition uplift (Figures 2.2, 2.3, 2.13, 2.15, and 2.17). Onlapping reflectors then abruptly shift to ~3-4 km seaward of the inner/outer wedge transition and backstep over the crest of the anticlinal thrust A (Us3) (Figure 2.17). An abrupt seaward shift truncates Us3 (U4), cutting Us3 into a lobate shape. Overlying reflectors then stack vertically to the seafloor and generally upstep across the slope (Us4; Figures 2.3 and 2.17).

Upper Strata sediments seem to be constrained to the slope, although data loss in the shallow portions of the shelf obscure any correlative conformities. Upper Strata are much thinner than Lower and Middle Strata, ranging from 0-500 m, with a median thickness of 94 m (Figures 2.8, 2.12 and 2.15). Thicknesses away from anticlinal thrusts A – E, the inner/outer wedge transition and the paleo canyon are limited to <150 m (Figure 2.15). The thickest sub basin (up to 498 m) developed between a pair of landward- and seaward-dipping anticlinal thrusts A and B, with sediment thicknesses increasing to the east (Figure 2.15).

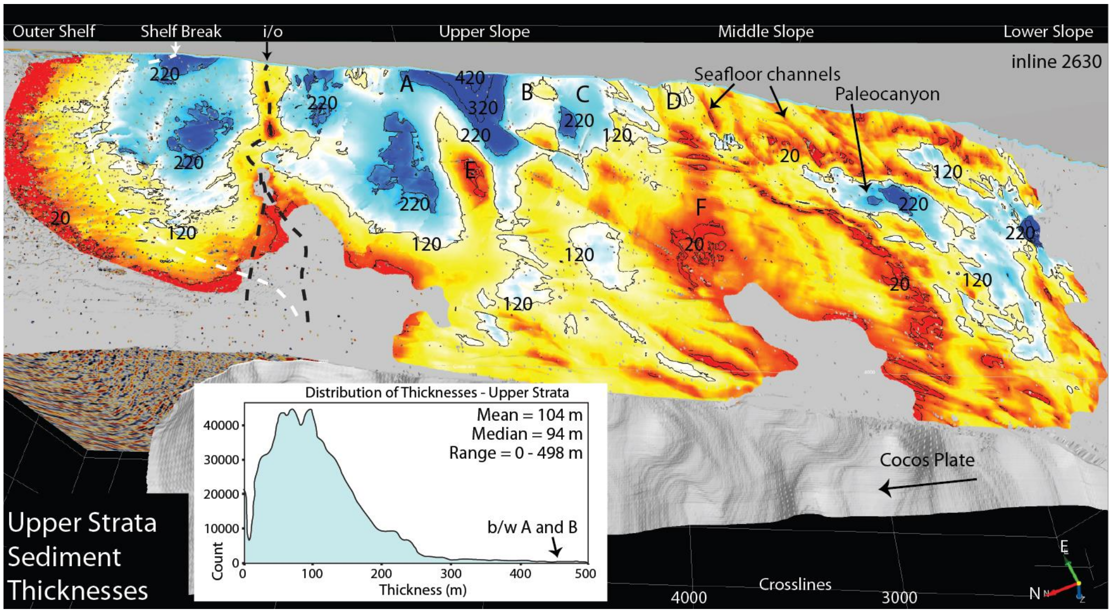

Figure 2.15 Upper Strata isopach with oblique perspective view looking SE across the seafloor horizon. Inline 2630 is shown for reference. Colors and labeled contours on seafloor denote calculated vertical thicknesses between seafloor and U1 horizons. Color scheme and other labels are same as figure 2.7. Inset is a histogram of thicknesses, with mean, median and range of thicknesses. Note the present day seafloor channels that remove Upper Strata and result in lower isopach values (reds). Also note the filled U1 paleo-canyon. Thicknesses away from active thrusts are low, ~100 m, within the slope. Thicknesses within the shelf are unconstrained due to poor shallow resolvability (i.e., not a clear correlative U1 conformable reflector).

Site U1413 drilled through ~180 m of Upper Strata, constraining these sediments to the Cobb Mountain reversal of the Matuyama chron, 1.78-1.19 Ma and younger (Figure 2.9) (Harris et al., 2013e).

2.5.2 Sedimentation Rates

Based on IODP magnetostratigraphy and biostratigraphy (Vannucchi et al., 2011; Harris et al., 2013e; Vannucchi et al., 2013) and CRISP sequence stratigraphy results, we broadly constrain sedimentation rates for each stratal domain.

2.5.2.1 Lower Strata

The L1 event, ~2.5 – 2.3 Ma (Harris et al., 2013d; Vannucchi et al., 2013), and M1 event, ~1.95 – 1.78 Ma (Harris et al., 2013e), constrain the duration of Lower Strata sedimentation to 0.35 – 0.78 m.y. This time frame, and the calculated isopach thicknesses for the shelf (up to ~1.3 km) and slope (up to ~1.6 km), constrain Lower Strata sedimentation rates for the shelf to ~1.7 - 3.7 km/m.y. and slope to ~2.1 – 4.6 km/m.y. These sedimentation rates are the highest for the margin during the Pleistocene. Furthermore, both shelf and slope rates are high and demonstrate that subsidence was broad and rapid across both domains.

2.5.2.2. Middle Strata

Middle Strata shelf and slope sedimentation rates are less constrained, due to the poor temporal constraint of the U1 event (1.78 – 1.19 Ma). We estimate that U1 occurred toward the tail end of the Cobb Mountain reversal by assuming a constant sedimentation rate, approximating the age to 1.3 Ma (Figure 2.9), constraining the duration of Middle Strata sedimentation to 0.48 – 0.65 m.y. With that estimation, and with observed max Middle Strata shelf and slope thicknesses of ~450 m and ~1000 m, we estimate a shelf rate up to 0.69 – 0.94 km/m.y. and slope rate up to ~1.5 – 2.1 km/m.y. The decline from Lower to Middle Strata in the shelf and slope sedimentation rates is approximately ten-fold to half.

2.5.2.3 Upper Strata

Because the U1 unconformity is only imaged across the slope, we can only constrain Upper Strata (~1.3 Ma – present) sedimentation rates for the slope. Upper Strata thicknesses reach up to ~500 m (between anticlinal thrusts A and B), and with an estimated U1 age of 1.3 Ma, the sedimentation rate is up to ~0.38 km/m.y. However, away from young anticlinal thrusts and the paleo canyon system, thicknesses are generally <150 m, thus sedimentation rates are generally <0.12 km/m.y., an order of magnitude less than Middle or Lower Strata. Thus, slope sedimentation rates tapered off quickly following U1, with sedimentation only occurring in the spaces created by active faulting and folding continued (i.e., eastern portion of the upper slope and downslope portions of middle and lower slopes; Figure 2.15).

2.5.3 Faulting

2.5.3.1 Thrust Faulting

The subduction thrust appears to serve as a source for a series of imbricate, landward-dipping thrust faults that extend from the toe to the inner/outer wedge transition (Figure 2.16). Thrust faults are observed to have a greater density and to accommodate greater offset nearer to the toe, or deformation front, and towards the SE portion of the volume, i.e., along strike, within the middle and upper slope (Figure 2.16). Often paired with these landward-dipping thrust faults are seaward-dipping thrust faults (e.g., anticlinal thrusts A and B, C and D), which accommodate greater offset towards the inner/outer wedge transition and to the SE portion of the volume (Figures 2.16 and 2.17). Deformation accommodated by thrust faulting has resulted in inclined folding, local uplift and subsidence, with generally tighter anticlinal and broader synclinal hanging wall thrusts (Figure 2.17). Middle and upper slope fold axes E, F, G and H are WSW-trending, while fold axes A – D are W-trending (Figures 2.5 and 2.10). Both fold trends are oblique to the NW-trending trench axis, lower slope ridges (seafloor expression of frontal prism imbricated and thrusted slices), and inner/outer wedge transition (Kluesner et al., 2013).

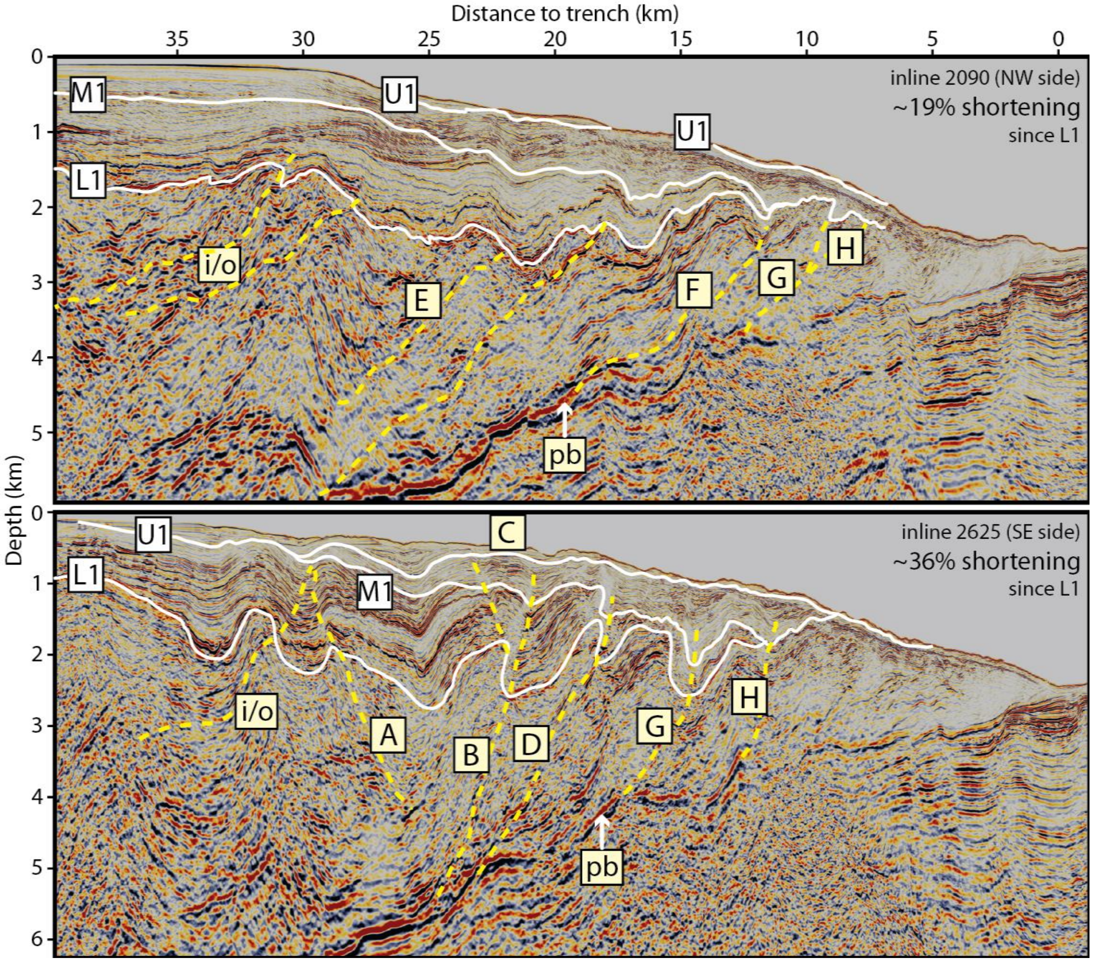

Figure 2.16 Inlines 2090 and 2625 showing increased shortening to SE nearer to the impinging Cocos Ridge. L1, M1 and U1 unconformities are shown with white dashed lines. Thrust faults are shown with dashed yellow lines and are labeled. The plate boundary (decollement) is labeled p.b. Trench is on the right side, shelf is to the left. Shortening is calculated relative to L1 change in length. Note the decrease in thrust spacing, increase in fault dip, the steepness, singularity and amount of offset of inner/outer wedge transition towards the SE (inline 2625) and the formation of seaward-dipping thrusts to the SE (inline 2625).

The inner/outer wedge transition is coincident with the shelf break along the western portion of CRISP, and deviates from the indented or deflected portion of the shelf break along the central and eastern portions (Figure 2.5). The outer wedge, generally coincident with the slope, is characterized by series of imbricate thrust faults and paired conjugate faults, while the landward portion, delineated by the shelf, is mostly absent shortening in Pleistocene strata (Figure 2.5). Interestingly, prominent Pleistocene subsidence is observed across both the inner and outer wedges (Figures 2.2 and 2.19).

The timing of middle and upper slope thrusting and folding (hence local uplift and subsidence) postdates early, rapid, broad subsidence and seems to have occurred in pulses of activity. The earliest Pleistocene shortening that is concomitant with earliest Lower Strata deposition is the inner/outer wedge transition, where there is observable thinning of Ls1 across the structure within the eastern portion of the volume (Figures 2.6 and 2.7). The central and western portions of the inner/outer wedge began shortening soon after (e.g., Ls2 thinning; Figures 2.6 and 2.7). There was a small degree of middle and upper slope shortening downslope during Lower Strata deposition, as seen by several slope basin inversions (e.g., Ls2 and Ls4 in Figure 2.17). Middle slope thrust F likely initiated during Ls1, as there is observable Ls1 thinning over its crest and the overlying Ls2 and Ls3 forestep its inclined back limb (Figures 2.2, 2.7 and 2.8). Middle slope thrust D initiated during the later stages of Lower Strata, as early Middle Strata (Ms1 – Ms3) sequences onlap and prograde over its back- and forelimbs (Figure 2.18). Thrusts A, B, and C postdate early Middle Strata (Ms1 – Ms4), and seem to have initiated after the M5 unconformity (~1.5 Ma; Figures 2.11 and 2.18), and thrust E, after M8 (~1.35 Ma; Figure 2.18). Interestingly, thrusts A, B, C, and D (which are two paired landward- and seaward-dipping anticlinal thrusts), all seem to have had a coeval pulse of activity following M5 (~1.5

Ma), and thrusts E and F, following M8 (~1.35 Ma; Figures 2.11, 2.14 and 2.16-2.18). Anticlinal thrusts A – F all bound the thickest Middle Strata basin, and thrusts D, F and G bound an adjacent, thick, downslope Middle Strata basin, all WSW-trending (Figure 12). Thrusts G and H were active during Middle Strata and were likely active during Lower Strata deposition, as Lower Strata taper out across their crests and limbs. Continued shortening during Upper Strata deposition was first accommodated by thrusts A and B, marked by Us1 (Figure 2.17). Subsequent shortening was accommodated by thrusts A – E and the inner/outer wedge transition (Figures 2.13, 2.15, 2.17 and 2.18). Thrusts A and B bound the thickest Upper Strata basin (Figure 2.15). Thrusts G and H are not well constrained during Upper Strata due to BSR interference, although it is likely they were and are active.

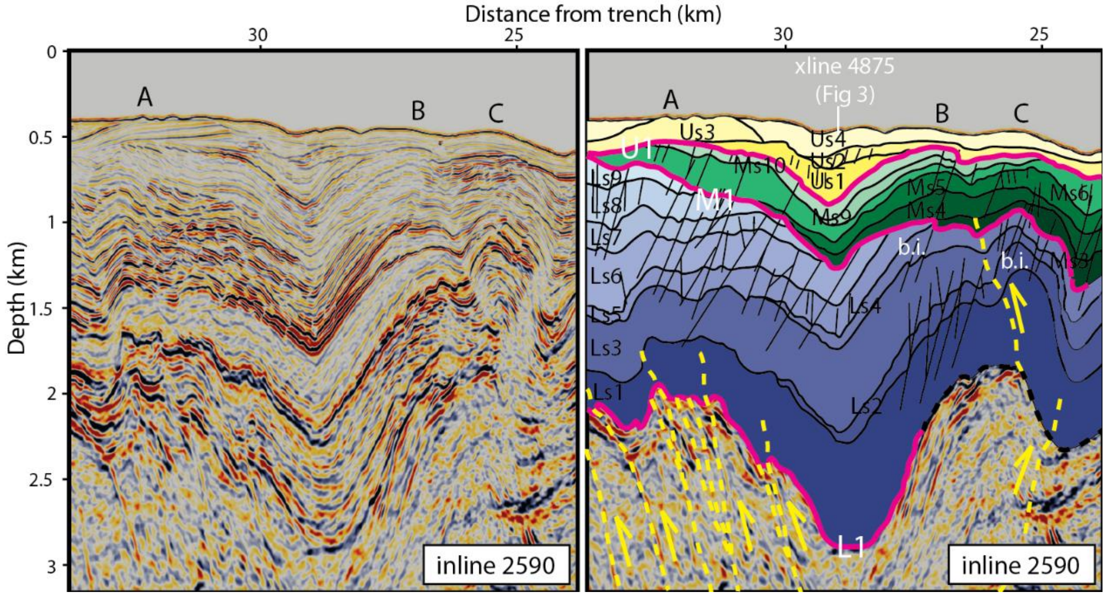

Figure 2.17 Inline 2590 thickest slope basin showing stratal domains, erosional events (thick pink lines) and depositional sequences and the thickest slope basin (~2.46 km thick). Color scheme is same as figure 2. Normal faults are shown with

thin black lines. Thrust faults are shown with yellow dashed lines. Several basin inversions are labeled as b.i. Note how the M1 erosional event cuts down to Ls4 in the upper slope (same as inline 2210 on the western side). Also note how normal faults are spatially associated with fold hinges and are shallow.

2.5.3.2 Normal Faulting

Moderately to steeply dipping discontinuities that accommodate normal motion are observed across the slope and shelf (Figures 2.6, 2.7, 2.10, 2.11, 2.13, 2.14, 2.17 and 2.18). These normal faults cut pervasively through all Pleistocene stratal domains and appear as distinct groups, or networks (Figures 2.10, 2.13, 2.17 and 2.18), suggesting that extension is episodic and occurs locally. These fault networks consist of intersecting arrays or tightly spaced parallel segments of varying geometries (Figures 2.10 and 2.13), suggesting that stresses spatially and temporally vary.

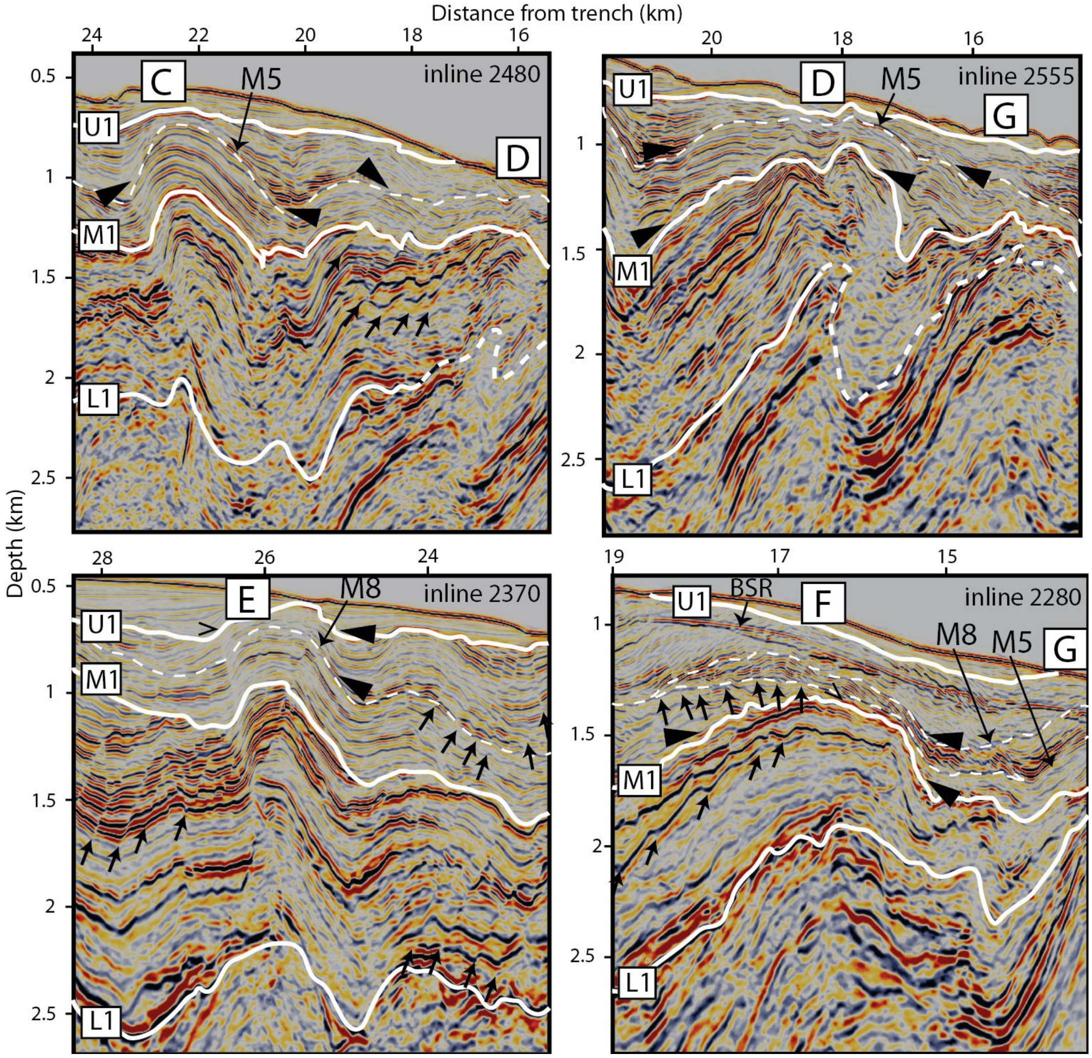

Figure 2.18 Four inlines timing of thrusting. Solid white lines show L1, M1 and U1 erosional events. Dashed white lines denote important unconformities (M5 and M8). Solid black arrows denote onlapping clinoforms. One sided arrows denote the base of prominent normal faults. Inline 2480 (upper left) shows the initiation of thrusts C and D following the M5 sequence boundary. Inline 2555 (upper right) shows the initiation of D after M1 and then another pulse of shortening following M5, continuing through Middle Strata. Thrust G initiation is less clear, but it seems to pre-dated L1 have been active through both Lower and Middle Strata. Inline 2370 (lower left) shows the initiation of E following M8. Inline 2280 (lower right) shows the initiation of F after M1 and continued during Middle Strata deposition.

Normal faults can be spatially associated with the hinges of anticlinal folds (Figures 2.11, 2.17 and 2.18), but are also prevalent across the shelf (Figure 2.10), upper slope (Figures 2.10 and 2.13), and possibly even the M1 erosional event. Normal fault activity and its control on sediment accumulation is minimal, with offsets <100 m (Figures 2.6, 2.11, 2.14 and 2.18), demonstrating that normal faults contribute little to vertical motions. Growth strata associated with normal faulting are rare, suggesting that these faults are not long lived. Normal faults are shallow and do not generally reach into the margin wedge or even rarely into Ls1 (Figures 2.6, 2.11, 2.14, 2.17 and 2.18).

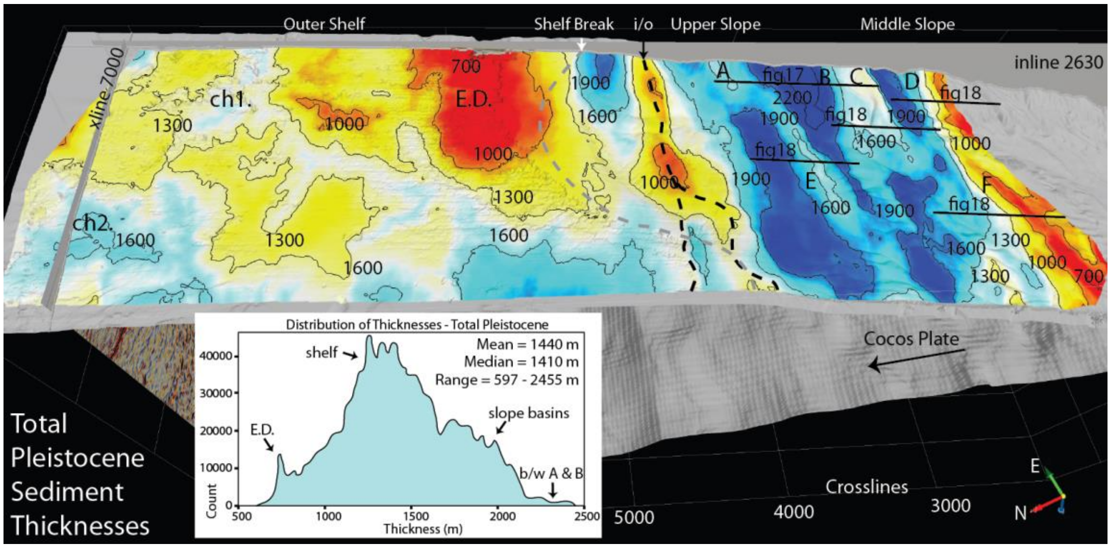

Figure 2.19 Total Pleistocene isopach with oblique perspective view looking SE across the seafloor horizon. Inline 2630 is shown for reference. Colors and labeled contours on seafloor denote calculated vertical thicknesses between seafloor and L1 horizons. Color scheme and other labels are same as figure 15. Inset is a histogram of total Pleistocene thicknesses, with mean, median and range of thicknesses. Clearly shown are the ch1 and ch2 channel systems, the eastern dome, the inner/outer wedge transition (even showing how it splays into two prominent thrusts), slope sub basins and bounding anticlinal thrusts. Note that Pleistocene strata thins downslope.

2.6 Interpretation

2.6.1 Early Pleistocene Outer Forearc Erosion and Subsidence

2.6.1.1 Panama Fracture Zone Subduction and Plate Kinematic Changes

Recovered margin wedge sediments from U1379 and U1380 demonstrate that before the L1 erosional event, the region was a marine basin filling with terrigenous sediments. Fossils and lithofacies from Vannucchi et al., [2013] suggest middle bathyal water depths (800 – 1200 m) for the present-day outermost shelf. Thus, to account for rapid uplift and broad extent of Early Pleistocene outer forearc (shelf and slope) subaerial erosion recorded by L1, we cite the spatiotemporal link of the southeastward PFZ triple junction migration across the CRISP portion of the forearc ~2 – 4 Ma (age depends on the projected paleo orientation of the PFZ and on which velocity model is used; Figure 2.1; Morell, 2016; DeMets et al., 1990; Demets et al., 1994, 2010; Kobayashi et al., 2014). How much sediments were removed is not constrained, but the broad extent of surface erosion (across the shelf and down to the middle slope) and deeply incised fluvial drainages (up to ~500 m) across the shelf suggests significant thinning of the margin wedge (Figure 2.20). There are several present-day analogue L1 erosional environments, including the Burica Peninsula, inboard of the PFZ, and Coiba and Jicarita islands, inboard of the Coiba Fracture Zone. Furthermore, Morell et al., (2011) found a temporal link between marine terrace uplift across the Burica Peninsula and PFZ SE migration. We suggest that at CRISP, the SE migration of the irregular and steep PFZ, or a related precursor to the PFZ, drove rapid, transient uplift and subaerial erosion at CRISP beginning ~2.5 Ma

(Figure 2.20). This subaerial erosion thinned the margin wedge and eroded sediments likely ended up in the trench, due to the transient steepness of the slope, where they were carried and/or subducted to the SE along with the PFZ.

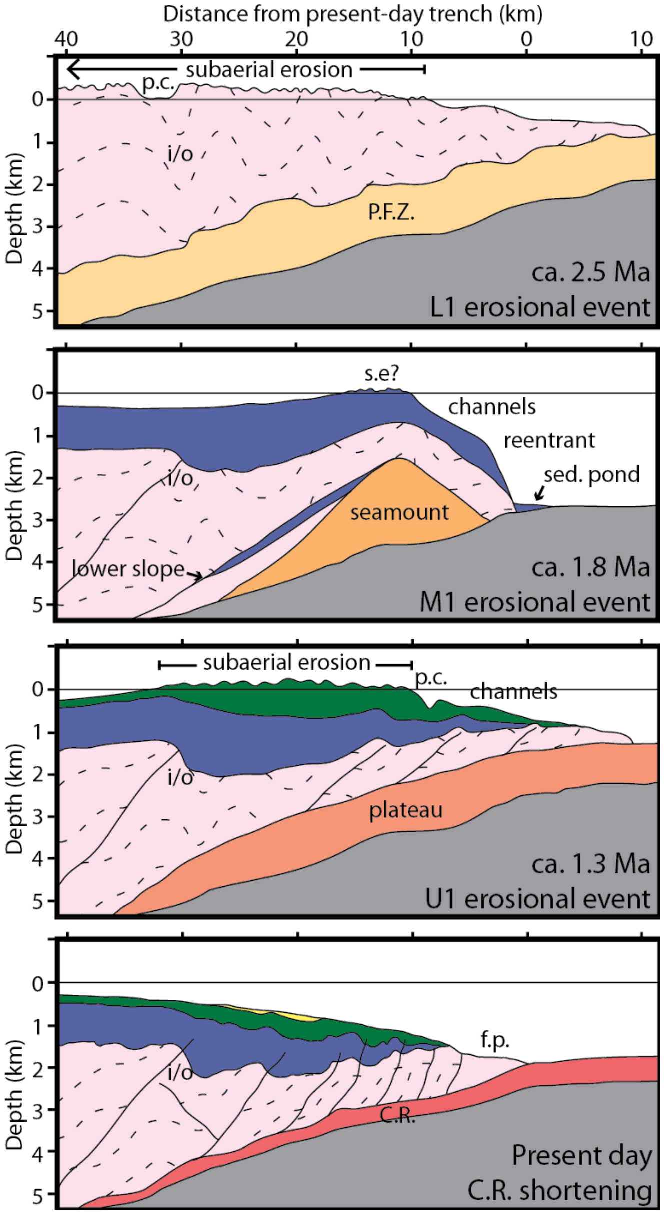

Figure 2.20 Schematic model of Pleistocene margin history of subducting topography, upper plate vertical motions, deformation, erosion and sedimentation. The margin wedge is shown in pink, Lower Strata in purple, Middle Strata in green, Upper Strata in yellow, the Cocos Plate in grey and subducting topography in oranges

and reds. P.F.Z. is Panama Fracture Zone, C.R. is Cocos Ridge, p.c. is paleo canyon, s.e. is subaerial erosion, i/o is the inner/outer wedge transision, f.p. is frontal prism, and sed. pond is sedimentary pond in the trench. Note the broad thinning of the margin wedge due to subaerial erosion during L1 and truncation of folded sediments. Note the removal of the lower slope with seamount subduction. Also note the shortening and thickening of the outer forearc due to the impinging Cocos Ridge.

To account for rapid and broad Early Pleistocene subsidence following uplift, we point to the continued SE migration and passage of the PFZ triple junction and associated bathymetric, crustal thickness and plate kinematic changes. The short timeframe (~0.5 m.y.) associated with robust subsidence (~1.6 km within the slope and ~1.3 km within the shelf) resulted in the highest sedimentation rates (shelf ~1.7 – 3.7 km/m.y. and slope ~2.1 – 4.6 km/m.y.) during any Pleistocene timeframe, and thus makes it likely that the passage of the steep topography of the PFZ was an important driver of rapid subsidence (since the margin was eroded across its surface, thinned broadly and subsided quickly). However, the three fold increase in relative convergence and decrease in crustal thickness, and the potential downward flexing of the subducting plate under the outer forearc (Furlong et al., 1982; Buiter et al., 2001), likely contributed to broad and continued subsidence as well (Lower Strata are laterally continuous and include large transgressive periods, >35 km, Ls1, and regressive shifts, >30 km, L2). To what degree each mechanism drove subsidence is not constrained, but the bulk of the observed net margin Pleistocene subsidence occurred during this Early Pleistocene ~0.5 m.y. window. Furthermore, the maintenance of the present-day position of the inner/outer wedge transition through the Pleistocene (Figures 2.2, 2.5 –2. 8, 2.10, 2.12 – 2.13, 2.15, 2.19 and2. 20), including during rapid Early Pleistocene subsidence (Figures 2.5 – 2.8), shows that the margin did not retreat landward during subsidence, as modeled by basal erosion, and suggests a link with plate boundary dynamics that do not require upper plate net material loss.

The spatiotemporal link of the PFZ triple junction migration and coincident outer forearc subsidence is also found offshore the Nicoya Peninsula (McIntosh et al., 1993). The same triple junction migration-outer forearc subsidence link is observed along other convergent margins, including Japan, Izu-Bonin, Mariana and Tonga, although backarc extension is also observed (Regalla et al., 2013).

2.6.2 Pleistocene Slope Erosional Events

Rapid Early Pleistocene subsidence is overprinted by two younger slope erosional events, the M1 and U1 events. These two large slope erosional events truncated and removed thick sections of strata, have erosional spatial footprints that extend across the entire slope, and they shifted or altered the existing states of sedimentation (Figures 2.2, 2.10 and 2.13). Each event differs in character, thickness of sediments removed and the amount of ensuing slope subsidence, but both M1 and U1 unconformities require anomalous mechanisms, as they both fall outside the window of relative base level fall and marine unconformities within the sequence stratigraphy model (eustasy, tectonics and sedimentation).

2.6.2.1 Seamount Subduction

Several observations yield insight into what may have been the driving mechanism for the earlier M1 unconformity, ~1.95 – 1.78 Ma, including: M1 has a steeply dipping upper slope geometry (8-10°) that cuts down section to Ls4, removing

~900 m thickness of Lower Strata (Figure 2.2), and it extends across the middle and lower slopes to the landward extent of the frontal prism, within ~5 km of the trench (Lower Strata included; Figure 2.10). It therefore almost extends across the entire slope (excluding the frontal prism), ~30 km in down dip length and it extends across the width of CRISP volume, ~11 km. These observations suggest that this erosional event was precipitated by a collapse of the slope and mass transport to the trench. We interpret that this collapse was driven by underthrusting topography which removed a portion of the lower slope and subsequently oversteepened the middle and upper slopes, analogous to the observed slope bite marks, collapse and subsequent infilling seen along the Costa Rican margin (Figure 2.1). These analogous slope bite marks are linked to seamount subduction (e.g., von Huene et al., 2000).

Several other observations also suggest slope oversteepening and collapse. M1 is cut by a dense, intersecting array of NW-, W-, and NE-striking normal faults, with offsets up to ~100 m, that seem to be temporally linked. This suggests that the slope area was under an episode of extension, possibly during uplift (e.g., Dominguez et al. 1998), or alternatively during deep seated downslope mass movement accommodated by fault block rotation (McIntosh et al., 1993). The thoroughly channelized M1 upper slope and overlying aggrading Middle Strata channels suggests that once the seamount passed, the upper slope/shelf edge water depth increased rapidly, and the steep slope gradient served as a pathway for sediments headed downslope, some likely refilling the deflected trench.

If we use the present-day water depths of the upper slope (300 – 700 m) and the approximate max thickness of Lower Strata removed (~900 m), we find a minimum seamount height of 1.2 – 1.6 km above surrounding bathymetric depths, if any of the slope was subaerially eroded (Figure 2.20). This height does not consider downward flexure due to an increased overlying load (i.e., isostasy), extension and thinning of Lower Strata during uplift (although this would be minor), or offscraping of seamount material during frontal prism/lower slope underthrusting. Many analogous conical seamounts of up to ~2 km heights are observed within the seamount zone of CNS generated crust seaward of the present-day trench (von Huene et al., 2000). These conical seamounts will impact the margin at some point, perhaps producing analogous local slope unconformities. However, we must note that if there was no subaerial erosion, we do not have a constraint on its minimum height, other than that it must have been of sufficient size to oversteepen the slope and drive slope collapse. Importantly, we observe that the thickness of middle and upper slope material removed is proportional to subsequent sedimentation (M1 truncated ~900 m of Lower Strata and subsequent filling with Middle Strata reach up to ~1000 m), suggesting that this discrete slope erosional event did not contribute substantially to middle and upper slope net subsidence (up to ~2.45 km; Figure 2.19).

2.6.2.2 Plateau Subduction

We interpret the later slope unconformity, U1, to also be due to underthrust seafloor topography. However, the nature of surface erosion and subsequent subsidence was notably different than the M1 event. The U1 unconformity is relatively flat, paralleling the seafloor. Its 3D surface is generally smooth, with only subtle and spare channels, small normal fault offsets, and gentle uplift and subsidence within the central to eastern portion due to younger landward- and seaward-dipping anticlinal thrusting (including the inner/outer wedge transition thrust). We interpret these observations to mean that the underthrust topography did not remove the lower slope and initiate middle and upper slope collapse. The middle and upper slope rise and fall was coherent and broad and produced an unconformity that is dipping parallel to the seafloor. The rise and fall also did not result in new accommodation space for sediments (Upper Strata sedimentation rates are generally <0.12 km/m.y.). This parallelism and subsequent lack of sedimentation suggests that the underthrust topography was broad and flat, with shallowly sloped sides. We observe that U1 removed up to ~150 m, likely via subaerial wave plain erosion, with the greatest amounts of erosion within the upper slope. Inferred wave plain erosion continues down to depths of ~1.1 km bsl (approximate seaward limit). This places a minimum underthrust topographic height of ~1.1 km, not accounting for the same unknowns as the M1 seamount height.

We interpret U1 as being due to the underthrusting and migration of a broad, flat and shallowly sloped oceanic plateau, >1 km high, around ~1.3 Ma (Figure 2.20). The underthrusting and migrating plateau would propagate a wave of forearc uplift without removing the lower slope and driving slope collapse (Martinod et al., 2013; Zeumann and Hampel, 2015). An analogous seafloor feature is the NE-trending Quepos Plateau that is generally ~1.5 km high and ~35 km wide (von Huene et al., 2000). Projecting the current NE-trend of the Quepos plateau through the trench and reconstructing relative Cocos Plate motion, a proto Quepos Plateau, or some related feature, possibly underthrusted and migrated across the CRISP portion of the margin ca. 1 – 2 Ma.

2.6.3 Pleistocene Slope Shortening

Rapid Early Pleistocene subsidence and the two major slope erosional events are conflated with progressive slope shortening. Observed middle and upper slope shortening progressed during younger Middle Strata deposition (Figures 2.11 – 2.12, 2.14, and 2.18) and Upper Strata deposition (Figures 2.15 – 2.18) and increases drastically to the SE, resulting in a relative counter clockwise rotation of fold axes and local SE Upper Strata basins (folds A to E, F, G, and H in Figure 2.10; Figure 2.15). We find that the shortening is decoupled from net subsidence and thus invoke another prominent incoming topographic feature as driving middle and upper slope shortening.

2.6.3.1 Cocos Ridge Subduction

The subduction of the Cocos Ridge has been cited as the driver of widespread Costa Rican tectonic erosion and outer forearc subsidence (e.g., Vannucchi et al. 2003). However, recent studies have shown the initiation of Cocos Ridge subduction (2 – 3 Ma) to be temporally inconsistent with outer forearc subsidence offshore Nicoya, where rapid subsidence began 5 – 6.5 Ma (e.g., Morell 2015; Morell 2016; Vannucchi et al. 2001). We observe that middle to upper slope shortening was low or absent (changes slightly along strike) during rapid Early Pleistocene outer forearc subsidence, with folding and thrusting developing after both L1 (~2.5 – 2.3 Ma) and M1 (~1.95 – 1.78 Ma) erosional events (middle and upper slope shortening generally postdates M5 and M8 unconformities, ~1.5 Ma and ~1.3 Ma; Figures 2.9, 2.17 and 2.18). We also observe that middle and upper slope shortening drastically increases to the SE (Figure 2.16), and the youngest, most active thrusts are essentially localized to the SE portion of CRISP, nearest to the impinging Cocos Ridge, resulting in local, SE Upper Strata basins up to ~500 m thick (between folds A and B; Figures 2.15 and 2.17) and rotation of middle and upper slope fold axes (WSW-trending) relative to the inner/outer wedge transition, frontal prism thrust faults and trench axis (NW-striking and NW-trending; see folds A to E, D and F in Figure 2.5 and A to E, D, F, G and H in Figure 2.10). These observations imply two important Cocos Ridge findings: 1) the Cocos Ridge is driving progressive slope (outer wedge) shortening at CRISP, starting ~1.5 Ma, as it slowly migrates from the SE to the NW along the trench with continued subduction (its geometry is slightly clockwise from relative plate motion; Figure 2.1), and 2) broad, net outer forearc subsidence is not linked to the Cocos Ridge impact with the trench nor its continued subduction (e.g., Upper Strata, which account for the last ~1.3 m.y. of slope sedimentation, generally have low sedimentation rates of <0.12 km/m.y. with average thicknesses of <150 m; Figure 2.15).

2.7 Conclusions

3D seismic sequence stratigraphy mapped within the CRISP seismic reflection volume offshore Costa Rica spatiotemporally constrains several Pleistocene outer forearc processes, including: sedimentation rates and patterns, vertical motions, and shortening. Three significant shelf and/or slope erosional events at ~2.5 – 2.3 Ma, 1.95 – 1.78 Ma, and 1.78 – 1.19 Ma, each with notable differences in spatial extent, volume removed and subsequent margin response, caused abrupt shifts in sedimentation patterns that fall outside the depositional sequence model. These shifts, coupled with vertical motions and observed shortening, reveal three primary mechanisms for Pleistocene to present shelf and slope sedimentation patterns: 1) regional subaerial erosion and rapid subsidence linked to the southeastward Panama Fracture Zone triple junction migration and associated abrupt bathymetric variations and plate kinematic changes, 2) transient, kilometer-scale uplift and subsidence due to inferred subducting plate topography passing through the subduction system, and 3) progressive outer wedge shortening accommodated by landward- and seaward-dipping thrust faults and fold development due to the impinging aseismic Cocos Ridge. Furthermore, we find that the present-day wedge geometry (to within ~3 km along strike) has been maintained through the Pleistocene, in contrast to modeled landward margin retreat. We also observe that deformation, i.e., extension and shortening, is decoupled from net margin subsidence. Our findings do not require basal erosion, and they suggest that the vertical motions of the Costa Rican outer forearc are not the result of a particular continuous process, but rather are a summation of plate to plate changes (e.g., passage of a fracture zone triple junction) and episodic events (e.g., subducting plate topography).

We have demonstrated that vertical motions and deformation offshore Costa Rica are driven in pulses of activity. Importantly, we observe that most of the Pleistocene net outer forearc subsidence occurred within an ~0.5 m.y. window during the Early Pleistocene, coincident with a migrating fracture zone and plate kinematics changes, analogous to recent findings offshore Japan. We also link anomalous slope unconformities with subducting topography and variable slope responses (e.g., M1 and Middle Strata versus U1 and Upper Strata) to topography size and shape (e.g., seamount versus plateau). We also document middle and upper slope shortening that postdates rapid Early Pleistocene outer forearc subsidence, and that shortening increases to the SE and drives counter clockwise rotation of middle/upper slope fold axes, providing a clear link to the impinging and slowly NW migrating Cocos Ridge. These findings demonstrate the advantages of 3D seismic reflection imaging, including having the ability to constrain the relative timing and rates of sedimentation, vertical motions and shortening, and coupled with drilling, can provide very well resolved basin and margin histories.

Chapter 3. Corrugated megathrust revealed offshore Costa Rica

3.1 Introduction

Faults at field and laboratory scales are observed to be non-planar, or rough, and at earthquake scales (kilometers), are inferred to be irregular and heterogenous (Aki, 1984; Scholz, 2002; Dieterich and Smith, 2009; Shi and Day, 2013). Exhumed fault surfaces commonly display corrugations or striations parallel to the slip direction (Engelder, 1974; Petit, 1987) that are observed across a broad range of spatial scales (Kirkpatrick and Brodsky, 2014; Candela and Brodsky, 2016) (μm to km), mechanical media, and geologic environments (Wright et al., 1974; John, 1987; Clark, 1993; Cann et al., 1997). For example, slip corrugations are observed along the interfaces between fast-flowing ice streams and underlying sediments (Clark, 1993; King et al., 2009). The mechanical processes proposed for corrugation formation are diverse, including: asperity ploughing and abrasion, debris streaking, and fracture/fault branching and linkage, among others (Means, 1987; Clark et al., 2003; Brodsky et al., 2016). Despite a general recognition that corrugations play a fundamental role in the behavior of faults, to our knowledge, well-defined corrugations have not been observed *in situ* at seismogenic depths along a fault surface, including across an interface of subducting tectonic plates.

The recent 2011 M_w 9 Tohoku-Oki earthquake demonstrated that coseismic slip can propagate all the way to the trench, and that maximum slip can occur along the shallowest portions of the megathrust (Lay et al., 2011). Subsequent work has shown that ruptures propagate farther along smoother faults due to smaller stress heterogeneity (Bletery et al., 2016) and fewer adjacent fracture networks available for off-fault slip (Wang and Bilek, 2011). Thus, greater fault roughness is thought to inhibit rupture propagation and has been inferred to do so offshore Costa Rica, where a zone of seamounts, plateaus and ridges are subducting, and the earthquake record lacks evidence for historic shallow coseismic slip (DeShon et al., 2003; Wang and Bilek, 2011; Chaves et al., 2017). We map with unprecedented spatial resolution the shallow 3D megathrust offshore Costa Rica and demonstrate *in situ* heterogeneity in the fault structure.

3.2 Megathrust morphology from 3D seismic reflection data

Here we utilize a 2011 3D depth-migrated seismic reflection volume offshore the Osa Peninsula of southern Costa Rica (Kluesner et al., 2013; Bangs et al., 2014), along the northwest portion of the Cocos Ridge, where the Cocos Plate dives below the Caribbean Plate. The 3D volume images the megathrust at 12.5 x 18.75 m horizontal resolution (binning size) and ~5 – 15 m shallow vertical resolution (Kallweit and Wood, 1982). Within the depth-migrated volume we mapped the megathrust (Figures 3.1 – 3.2) utilizing post stack processing, filtering (Chopra and Marfurt, 2013) and amplitude-driven tracking techniques (Tingdahl and de Groot, 2003) commonly used in oil and gas exploration. More information is provided in Appendix A.

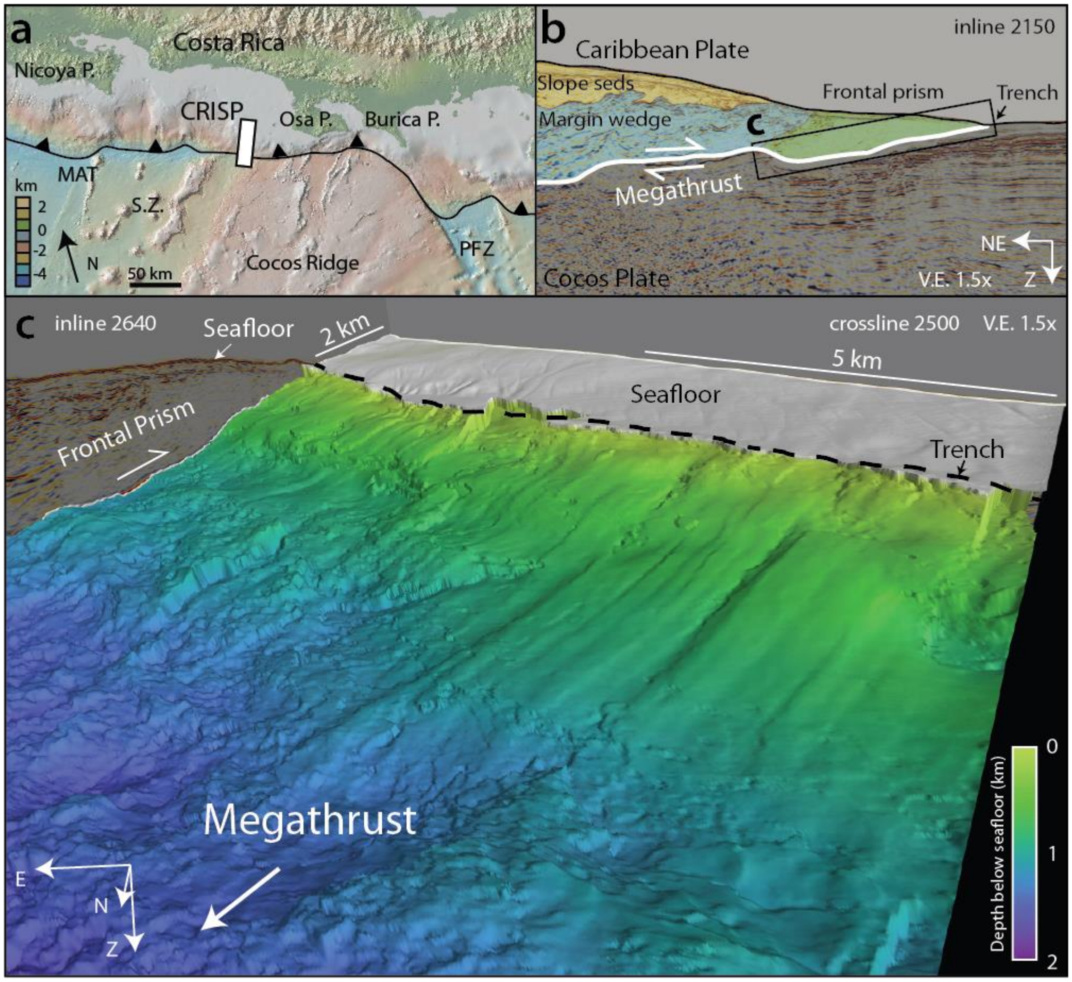

Figure 3.1 Tectonic setting, inline 2150 and upslope perspective view of megathrust. Topographic shaded relief map of the Costa Rica margin (from Global Multi-Resolution Topography (GMRT) synthesis within GeoMapApp45). The Middle American Trench (MAT) is shown with a black line and black triangles on the upper plate. 2011 The coverage of the 3D seismic reflection volume (CRISP) is shown with a white rectangle. b, Inline 2150 from the CRISP volume is showing the trench, frontal prism (green) and outer wedge with interpreted sections of slope sediments (yellow) and margin wedge (blue). c, Perspective view of the shallow megathrust looking seaward toward the trench and the frontal prism has been cut away. Inline 2640 (frontal prism) is shown for reference. Color scale is kilometers (km) below seafloor and grey denotes the seafloor. V.E. is vertical exaggeration.

The megathrust was differentiated by both its polarity and structural position, namely that it either separates landward-dipping reflections from underlying subhorizontal reflections or that it cuts across and through landward-dipping reflections (Figure 3.2b-e). We corroborate this interpreter-driven result with independently derived volumetric attributes, such as apparent dip (Marfurt, 2006) and curvature (Roberts, 2001), that extract subtle geometric variations of features from trace to trace to better constrain the detailed megathrust morphology (Appendix A; Figure 3.3). The resulting surface is the best-resolved 3D perspective of any shallow megathrust to date. It reveals a plate interface with remarkable detail and contrasts, varying from 1) smooth and well-developed to 2) rough and weakly-developed (Figures 3.1-3.3).

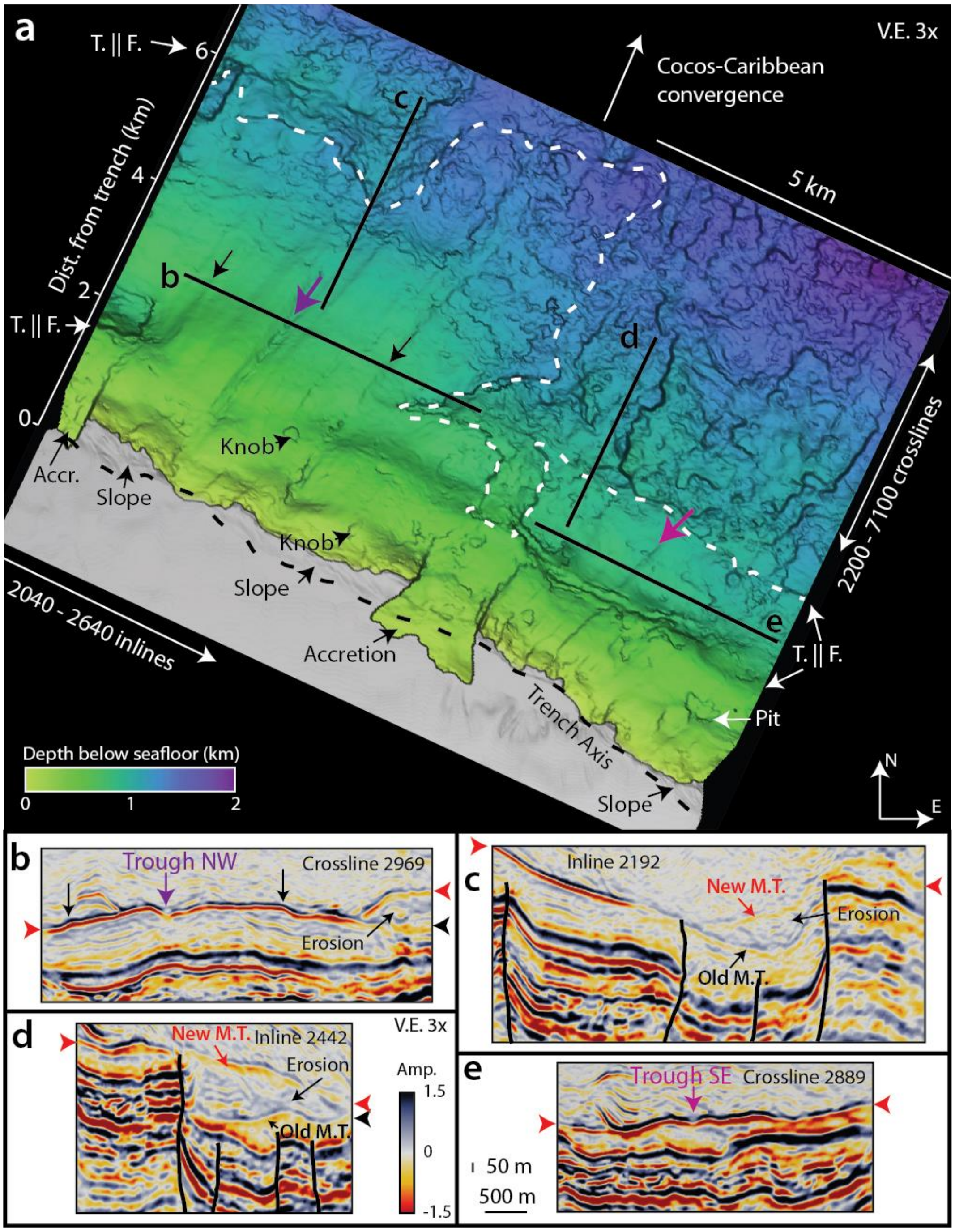

Figure 3.2 Map view of depth below seafloor along megathrust. a, Map view of shallow megathrust with depth below seafloor (km) overlain in greens (thinner) to blues (thicker). Trench is shown with dashed black line. Approximate boundary from corrugated to weakly corrugated is shown with dashed white line. Black solid lines denote locations of inlines and crosslines shown in b-e. Inline numbers increase from

left to right and crossline numbers increase from bottom to top. Black arrows denote prominent ridges in map view and in b. Purple arrow is prominent trough labeled Trough NW in map view and in b. Pink arrow is Trough SE in map view and in c. T||F is trench parallel faults. b, Crossline 2969 showing depth section of corrugated megathrust with prominent troughs (including Trough NW) and ridges. Note low amplitude reflection at center of Trough NW. c-d, Inlines 2192 and 2442 showing depth sections of down dip portion of corrugations where the megathrust steps up section in relation to large offset trench parallel faults (shown with white dashed lines). e, Crossline 2889 showing depth section of corrugations within the southeast portion, including Trough SE. Amplitude reflection color scale and vertical and horizontal scale is shown between panels d and e. M.T. is megathrust. Red arrowheads denote active megathrust and black arrowheads denote former megathrust Note change of megathrust reflection amplitude along well corrugated versus weakly corrugated portions.

Furthermore, the smooth and well-developed portions are corrugated, with corrugations that are meters to tens of meters high, extend kilometers along their long axes (length) and hundreds of meters across their short axes (width). The corrugated portions also exhibit high reflector amplitudes and reversed polarity relative to the seafloor (Figure 3.1-3.4).

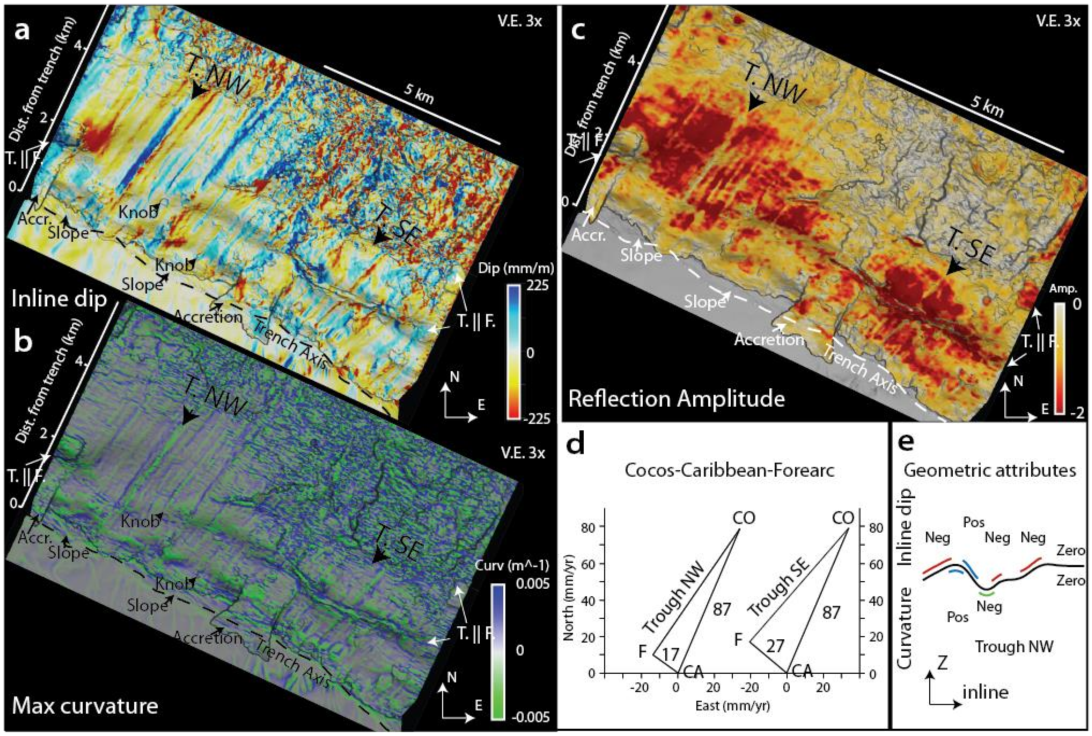

Figure 3.3 Map view of dip, curvature, reflection amplitude along megathrust and linear velocity diagram. a-c, Inline dip, maximum curvature and reflection amplitude extracted along the picked megathrust horizon. Note that with inline dip values, blues and reds meet along the axes of troughs and ridges, i.e., inline dip highlights the sides of dipping features. Whereas with maximum curvature, trough and ridge axes are highlighted by greens (troughs) and blues (ridges). Note how sensitive maximum curvature is to more chaotic portions of the megathrust and note linear streaks of low amplitudes along corrugation troughs. d, Linear velocity diagram of trench parallel slip from the orientations of Trough NW and Trough SE. CO is Cocos Plate, CA is Carribbean Plate, and F is Forearc. e, Reference diagram for inline dip and curvature. For inline dip, blues dip to the SE and reds dip to the NW. For curvature, greens denote troughs and blues denote ridges.

The corrugations are observed within hundreds of meters (>200-600 m) from the up-dip extent of the megathrust and can be seen extending down-dip >5 km to plate bending faults (~1.4 km below seafloor; Figures 3.2-3.3). At these shallow depths, corrugation distribution is heterogenous with the shallow central and eastern portions of the megathrust having a relatively chaotic morphology that lacks well-defined corrugations (Figures 3.1 – 3.3). These shallow chaotic portions generally coincide with places where the megathrust has propagated up section (relative to its original position) through tilted, fractured and consolidated strata of the frontal prism (Tobin et al., 2001; Harris et al., 2013b), capturing upper plate material and transferring it to the subducting plate (frontal prism erosion; Figure 3.2b, d and e). These newly propagated portions of the megathrust spatially coincide with large-offset (~>200 m) plate bending faults, either propagating down dip for landward-dipping faults or up dip for seaward-dipping faults (Figure 3.2). Several local plate bending faults seem to be propagating into the overlying frontal prism, possibly due to delayed initial plate bending that is landward of the trench rather than seaward of the trench. In contrast, normal faults are typically first observed at the outer rise, i.e., outer trench wall, along other Pacific convergent margins (Masson, 1991) (Figure 3.2). Newly propagated portions of the megathrust generally form proximal to plate bending faults with offsets ~>200 m, although an exception is within the most SE portion, where trench-parallel offsets are <200 m, even down to <100 m. This exception could be due to lateral propagation (along strike) of the new megathrust from the central area. Regardless, because these newer portions of the megathrust have accommodated small amounts of slip, they have not developed a well-defined surface, resulting in lower amplitude and relatively chaotic seismic reflections (Figure 3.2). These portions lack well-defined corrugations (Figures 3.1-3.3).

3.3 Scale of corrugations

We extracted corrugation widths and heights across the megathrust horizon. The corrugations have a median width and height of 160 m and 7 m, with a range of 113 – 729 m and 2.7 – 53 m (Figure 3.4).

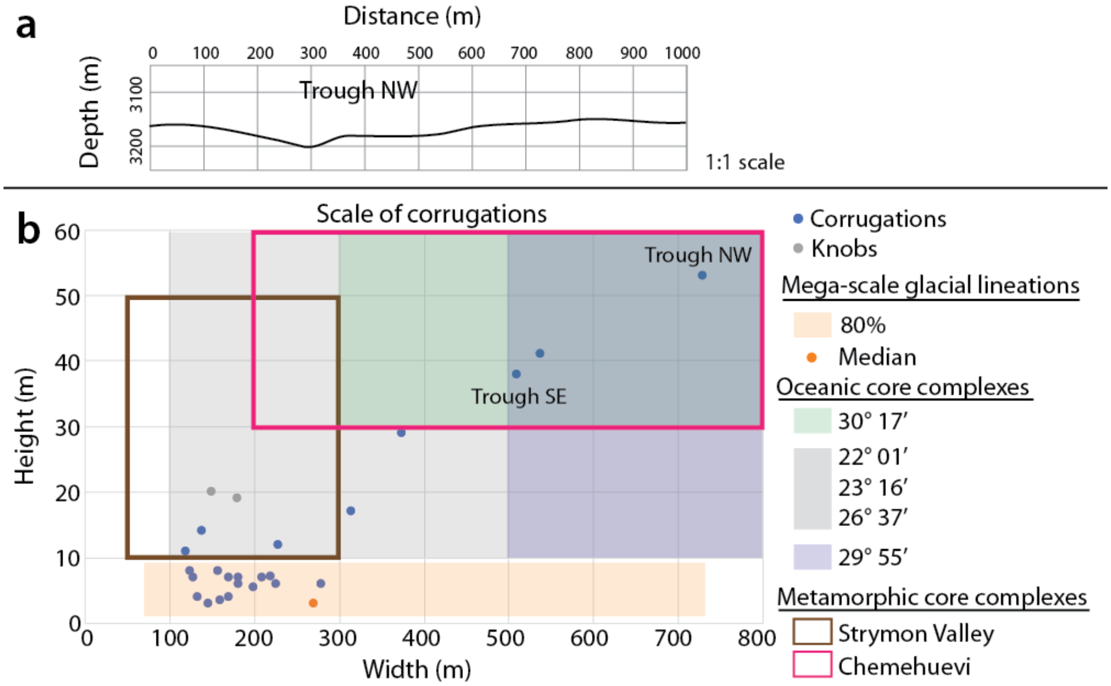

Figure 3.4 Scale of corrugations. a, A 1:1 scale of Trough NW for reference. b, Widths and heights plotted of corrugations and knobs from megathrust. Overlain are the ranges of corrugations from mega-scale glacial lineations46 (80% of measurements and median value), oceanic core complexes32 (intermediate scale) and metamorphic core.

The corrugations are at a similar scale to structures along other large-scale displacement interfaces, including intermediate-scale corrugations along onshore and offshore low-angle detachments faults (Wright et al., 1974; John, 1987; Dinter, 1998; Tucholke et al., 1998) and mega-scale glacial lineations (Clark, 1993). A best fit linear trend to the data gives a height/width aspect ratio of 0.08. This value of 0.08 is slightly larger than observed for terrestrial fault exposures (Brodsky et al., 2016), although it may be biased high because of detectability limitations (Rafaelsen et al., 2002). Heights less than the theoretical vertical resolution of ~5 m are observable due to the 3D nature of the data. In this case, the corrugations generally extend hundreds of meters to kilometers, extending beyond the Fresnel zone (horizontal resolution), making heights <5 m detectable. Figure 2.4 reports heights as low as 2.7 m. These values indicate that significant height corrugations exist that could be important for producing seismic waves, channeling fluids and controlling tremor locations as inferred from previous studies of exhumed faults (Ghosh et al., 2010; Kirkpatrick and Brodsky, 2014; Brodsky et al., 2016).

3.4 Corrugation genesis

We observe several consistencies with outcrop fault corrugations (Engelder, 1974; Petit, 1987; Kirkpatrick and Brodsky, 2014; Candela and Brodsky, 2016). The corrugations are not imaged along underthrusting, undeformed strata or in the overlying frontal prism (Figure 3.2b-e). The corrugations do not coincide with truncations and/or offset of reflections below or above the megathrust (i.e., are not coincident with trench perpendicular faulting; Figure 3.2b-e). Furthermore, they are oriented ~11 – 18˚ clockwise from plate motion vectors (DeMets et al., 2010; Kobayashi et al., 2014), making them more orthogonal to the trench and more closely aligned with regional earthquake slip vectors (DeMets, 2001). Based on these observations, and in conjunction with their continuity, distribution and scale, we interpret the corrugations to be non-penetrative slip lineations that form due to slip along the plate interface.

What slip processes drive their formation is less clear. We have imaged discrete features (we call knobs in Figures 3.1 – 3.3) that are at a similar scale as most of our observed corrugations (Figure 3.4). These knobs could act as asperities that groove or furrow adjacent rock, analogous to groove-ploughing theories (Means, 1987; Clark et al., 2003); however, they lack detectable corrugations in their wake (Figure 3.2). Alternatively, could processes thought to control meter-scale roughness, such as anastomosing and linking slip surfaces that form lenses (Brodsky et al., 2016), scale up to these hundreds of meters wide corrugations? Detailed 3D imaging of *in situ* corrugations observed here extend those observed at outcrop scales and those observed along other mechanical media and provide a new dataset for future quantitative investigations.

3.5 Implications for forearc translation

Previous work has shown compelling evidence for strain partitioning along the Costa Rica margin (DeMets, 2001; LaFemina et al., 2009), resulting in a forearc that is being translated predominantly northwestward (trench parallel). Using the orientation of two prominent troughs from the NW and SE megathrust as slip directions, and MORVEL plate velocities (DeMets et al., 2010; Kobayashi et al., 2014), we constrain the rate of northwestward translation offshore Osa to ~17 – 27 mm/yr (Figure 3.3d). These rates are higher than previous rates of 11 – 17 mm/yr from Costa Rica to Guatemala(DeMets, 2001; Kobayashi et al., 2014). We also observe a relatively continuous counter-clockwise rotation of slip, ~7˚, from the southeastern to northwestern portion (away from the Cocos Ridge), ~11 km along strike (Figures 3.2-3.3). The counter-clockwise rotation fits the regional trend of rotation of slip away from the Cocos Ridge, as seen in slope seamount scars and GPS derived velocity fields (LaFemina et al., 2009). Our observed counter-clockwise rotation of slip and lower trench parallel rates away from the Cocos Ridge support the model of the Cocos Ridge acting as a rigid indenter that drives tectonic escape and trench parallel motion (LaFemina et al., 2009; Kobayashi et al., 2014), even in areas where convergence is nearly orthogonal (southern Costa Rica).

3.6 Implications for earthquakes

These new observations demonstrate several important processes. They show that the megathrust is smoothed as it accumulates slip (i.e., matures), aligning with results seen in outcrop (Sagy et al., 2007), and that slip develops corrugations at similar scales to corrugations seen along exhumed faults in other environments (Wright et al., 1974; John, 1987; Dinter, 1998; Tucholke et al., 1998).The well corrugated portions produce notably higher amplitude negative polarity reflections, which have been linked to higher fluid content in these environments (Bangs et al., 2014). Furthermore, within these fluid-rich corrugated portions, we observe streaks of low amplitudes (Figure 3.3c), which correspond to troughs of larger individual corrugations (e.g., Troughs NW and SE; Figure 3.2b and 3.2c). These observations, coupled with findings from offshore Nicoya (Tobin et al., 2001), suggest that as fluids ascend to, or move along, the nonplanar and corrugated megathrust, they are bounded by its low cross-fault permeability and thus migrate from local lows (troughs) to local highs (ridges). This could facilitate linear zones of varying pore-fluid pressures from troughs to ridges, which have been appealed to at greater depths in prior work related to slip-parallel streaking of tremor (Ghosh et al., 2010).

It is not clear whether historical earthquakes offshore Costa Rica have slipped to the trench (e.g., 1983 Osa Earthquake M_w=7.4; Adamek and Tajima, 1987). However, well recorded earthquakes, like the 2012 Nicoya Earthquake M_w=7.6 or the 2002 Osa Earthquake M_w=6.4 (nucleated only at ~6 km depth and ~25 km from the trench), do not seem to have done so (Arroyo et al., 2014; Chaves et al., 2017). Our data show that the shallow, smooth and corrugated portions of the megathrust are bordered by younger and rougher generations of the megathrust cutting through the base of the overlying plate. If rougher and/or immature faults inhibit rupture propagation (Wang and Bilek, 2011; Bletery et al., 2016), our data may show why deeper coseismic slip offshore Costa Rica does not propagate to the trench and why earthquakes there seem to have multiple rupture patches (Wang and Bilek, 2011). Furthermore, because continued plate bending faulting with subduction is seen at other convergent margins (Isacks and Molnar, 1969), our results provide a means to assess the tendency for shallow coseismic slip elsewhere.

Novel technology and workflows (Roberts, 2001; Tingdahl and de Groot, 2003; Marfurt, 2006; Chopra and Marfurt, 2013) applied to a 3D pre-stack depth-migrated volume of a subduction zone have made it possible to document *in situ* corrugations along a megathrust within an active subduction zone for the first time.

These findings also have important implications for the net exchange of materials under the frontal prism and more broadly the exchange of material at a margin thought to be erosive. Finally, because corrugations are observed across the entire width of the 3D volume, we speculate that analogous corrugations exist along portions of subduction megathrusts globally. The previous hypotheses proposing that corrugations control slip and fluid behavior on the plate interface appear to be well-founded (Rubin et al., 1999; Ghosh et al., 2010).

Chapter 4. A balanced Costa Rican convergent margin: blurring the lines between accretionary and erosional margins

4.1 Introduction

Convergent margin forearcs, crust between trenches and arcs, are juxtaposed against subducting plates and disproportionately contribute to the growth and/or recycling of continental crust (Clift and Vannucchi, 2004). To constrain forearc mass budgets, many studies utilize offshore drilling and 2D marine geophysical imaging datasets, incorporated with the onshore record, to estimate mass budgets across ~44,000 km of ocean-margin subduction zones (e.g., Vannucchi et al., 2013). From this work, the rate of convergence and thickness of incoming sediments seem to control whether forearcs grow (accrete) or recede (erode) over million year timescales (Clift and Vannucchi, 2004). However, such studies have been limited by 1) the 1D and 2D nature of spatially sparse sampling and imaging, which limits the size of interpretable structures and is prone to spatial aliasing (Cartwright and Huuse, 2005), and 2) the inability of 2D imaging to migrate out-of-plane reflections from complex geologic structures to their correct locations and to handle lateral velocity variations (Yilmaz, 2001).

The Costa Rican margin, with its ~60 km of trench embayment (Figure 4.1) and record of Neogene slope subsidence, is considered an erosional margin (Vannucchi et al., 2013). It has thin incoming sediments (<0.5 km thickness; Harris et al., 2013b) and a fast convergence rate (80 km/my; Demets et al., 2010). However, recently collected 3D seismic reflection data image accretionary and shortening structures within the middle prism of the outer forearc (Bangs et al., 2016) and Pleistocene vertical motions (Edwards et al., 2018a) that conflict with an erosional model. To resolve this conflict, we utilize both a post-stack time migrated volume and a pre-stack depth migrated volume to quantify an in-situ mass budget of the outermost ~10 km of the forearc. We use this ~125 ka (77 km/my orthogonal convergence rate; DeMets et al., 2010) mass budget to reassess the mass budget across the entire forearc and compare our results to previous estimates.

Figure 4.1 Reference topographic map of the Costa Rica margin. Outline of 3D survey marked by white box with Figure 2 portion highlighted in blue. Projected Middle America Trench (MAT) marked by dashed black line with amount of trench embayment estimated. Major topographic features are marked, including peninsulas (Pen.) and Panama Fracture Zone (PFZ).

4.2 Quantifying 100 km^2 mass budget

The boundary along which subducting plates slide past each other can change its structural position when new incoming sediments (Moore and Silver, 1987; Huiqi et al., 1992), more favorable rheology (Ikari et al., 2018) and / or changes in geometry due to plate bending occur (Boston et al., 2014). When the megathrust does change its structural position, there is an exchange of material between the plates. If the megathrust jumps up-section, material is transferred from the upper to the lower plate (basal erosion; Hilde, 1983), and conversely, if it drops down-section (underplating;

Kimura et al., 2010), or if it steps seaward at the deformation front (Huiqi et al., 1992), material is transferred from the lower to the upper plate (Moore and Silver, 1987). The net material exchange is a sum of these megathrust positional changes,

$$A + U - E = \Delta UP \quad (1)$$

where A is accretion at the trench, U is underplating, E is basal erosion and ΔUP is the volume change of the upper plate. The total sediment subducted, S, is the sum of the remaining sediments that bypass the upper plate (UP).

4.2.1 A, E and S Volumes

We utilize pre-stack depth migrated seismic reflection data to constrain A, E and S volumes by detailed 3D mapping. We mapped these volumes by tracking the top and bottom bounding surfaces and then calculating a thickness (vertical distance) per seismogram (each seismogram is a stacked seismogram, therefore a common midpoint (CMP)). We employed post-stack processing techniques that remove noise and aid amplitude driven tracking (Tingdahl and de Groot, 2003). Mapping methods followed the same techniques as those outlined in Appendix A.

4.2.2 A, E and S Bounding Surfaces

The basal surface of A volumes is marked by foreland nucleating (present, past and proto megathrusts) at the deformation front. These thrusts are reversed polarity reflections (relative to the seafloor) immediately outboard of the principal deformation front that truncate incipient folding (i.e., stratal disruption; Figure 4.2 and B1). The top surface of accretionary volumes is the seafloor and/or the former, abandoned megathrust, which has been back-rotated to steeper angles (Figure 4.2 and B1).

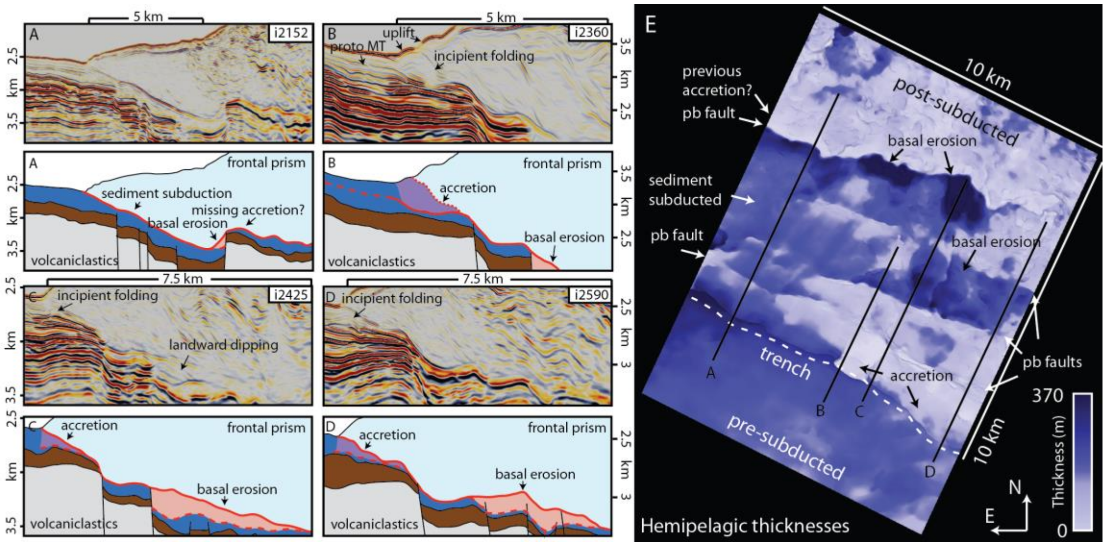

Figure 4.2 Inlines 2152, 2360, 2425 and 2590 showing material transfer. Panels from top left to bottom right (A to D) progress from NW to SE along the trench and are shown on panel E. Top panels are uninterpreted depth migrated seismic sections and bottom panels are interpreted. Purple are accreted hemipelagics and light orange are basal eroded sediments. Blue and brown are incoming and subducted hemipelagics and pelagics. Thick red line is the active megathrust and red dashed line is former or proto megathrust. All inlines are dip-steered median filtered data with a 4 x 6 (inline x crossline) stepout. Map view of hemipelagic thicknesses and labeled features (pb is plate bending) shown in panel E for reference.

Eroded volumes, E, are seen where lower portions of imbricate stacks of steeply landward dipping reflections within the frontal prism are cut by a reversed polarity subhorizontal reflection that links or bridges the megathrust up and down dip across high-angle, normal offset reflections (plate bending faults) orthogonal to the megathrust (Figs. 4.2C and B1B-C; Edwards et al., 2018b). The top bounding surface is this subhorizontal reflection, and the bottom bounding surface is a subhorizontal reversed polarity reflection that separates subhorizontal reflections below (underthrusting sediments) from steeply landward dipping reflections above (intensely deformed imbricate thrust stacks formerly of the upper plate).

S is bounded across its top by the megathrust or where present the base of E and across its bottom by the underthrusting lavas (Figure 4.2 and B1). The top of the lavas was found by a well-to-seismic synthetic tie (U1414 encountered lavas at 370 meters below seafloor; Harris et al., 2013b; Figure B2), and is marked by a positive polarity reflection overlaying discontinuous and chaotic reflections.

4.2.3 A, E and S Totals

Mapping A, E and S thicknesses utilized ~100,000 depth converted seismograms. We summed respective A, E and S thicknesses, scaled them to volume per km along trench, km^3/km, by multiplying them by the nominal bin size in the 3D volume, ~12.49 x 18.748 m, and then multiplied them by 1 – median porosity (solid portion of sediments). We used solid portions of 0.28 for A (median hemipelagic solid portion from well U1414; Harris et al., 2013b), 0.4 for E (median frontal prism sediment solid portion from well U1412; Harris et al., 2013a), and 0.3 for S (median pelagic solid portion from well U1414). We found A = 0.05 km^3/km, E = 0.09 km^3/km and S = 1.0 km^3/km.

4.2.4 Missing U

Because mapping is only capturing accretion at present at the deformation front (Figure B3), it is not accounting for underplated or previously accreted volumes, (we include both in U), transferred during the previous ~125 ka of subduction. Such volumes are difficult to map because 1) abandonment and down-stepping can occur out of sequence, although some down-stepping portions are imaged (Figure B4) and 2) the depth that landward-dipping thrusts step into the hemipelagics at the deformation front is not consistent. Thus, we modeled underthrust porosities, restored thicknesses and estimated U by measuring the shift in the distribution of thicknesses before and after subduction. And since the megathrust does not interact with the pelagic reflection (top of the pelagic section) within ~10 km of the trench, we constrain our statistical approach to the hemipelagic section.

The distribution of hemipelagic thicknesses before subduction, extracted from ~150,000 depth converted seismograms, has a range of 115 – 370 m (3σ from median), with a median thickness of 204 m. After subduction, hemipelagic thicknesses, extracted from ~450,000 depth converted seismograms, shift to thinner thicknesses, with minimum thicknesses down to <5 m and a median thickness of 82 m (Figure B5). Thinning is expected because a significant volume of sediments are offscraped at the deformation front and the overlying load increases rapidly, resulting in compaction driving fluids out (Figure B5; Moore and Vrolijk, 1992). If we can account for present offscraping at the deformation front and thinning of sediments due to compaction, we can then estimate U by quantifying the shift in the distribution of thicknesses before and after subduction. This method assumes that the past ~125 ka of incoming hemipelagics thicknesses are the same as at present, a reasonable assumption suggested by both the record of accretion of thin slices of sediments in the frontal prism (Figure 4.2 and B1) and consistent thicknesses progressively outboard of the trench (Figure B5A).

4.2.5 Restoring Subducted Thicknesses to Pre-Subducted Thicknesses

We restore thicknesses by removing the effects of compaction (i.e., porosity loss), with burial depths up to ~2.5 km below seafloor. Modeling results for these depths support our assumption that the volume of underthrust grains did not change by diagenesis and mineral dehydration (Moore and Vrolijk, 1992). We model underthrust porosities by two end-member approaches: 1) a simple 1D Athy logarthimic depth – porosity relation (Athy, 1930) and 2) geostatistical conditional simulation (i.e., stochastic inversion) of acoustic impedances (Haas and Dubrule, 1994) transformed to porosities. Modeled porosities are then used to restore thicknesses from their compacted state by the following porosity – thickness relation (Figure B6; Van Hinte, 1978),

$$T_o = \frac{(1-\varphi_n)T_n}{1-\varphi_o} \tag{2}$$

where φ_o is the median porosity (0.72) of incoming hemipelagics (Harris et al., 2013c) and Tn and φ_n are the underthrust thickness and porosity. Restored thicknesses are then compared to incoming sediment thicknesses by finding their relative deficits ($T_i - T_o$) to incoming median, 3σ below and above median (115 m, 204 m and 370 m) thicknesses, and then are scaled by the solid portions of hemipelagics, 0.28.

4.2.6 1D Athy Depth – Porosity Model

We utilized the empirical relationship that porosity logarithmically decreases with depth of burial (Athy, 1930), such that,

$$\varphi_n = \varphi_o \exp(-\beta z) \tag{3}$$

where φ_o and φ_n are the original and buried porosities, β is a constant linked to lithology and z is depth below the seafloor. By utilizing the Athy model, we ignore excess pore pressures at depth, and as such, find end-member conservative estimates of U. We applied a best fit between Equation 3 and the hemipelagic depth / porosity data from well U1414 to obtain φ_o, 0.76, and β, 6.1 x 10^{-4} (Figure B7), with z being the top of the underthrusting sediments (i.e., megathrust). Modeled porosities (Figure B8) gave restored thickness deficits, using Equation 2, that summed to conservative (115 m cut-off), median (204 m cut-off) and upper (115 m cut-off) estimates of U_{athy} = 0.01 km^3/km, 0.09 km^3/km and 0.3 km^3/km (Figure B9).

4.2.8 Geostatistical Conditional Simulation of Acoustic Impedance

We performed 90 non-unique inversions for acoustic impedance (Figure B10), by building an a priori model of impedances (Figure B11), estimating the source wavelet, computing semivariogram parameters, and using industry software provided to us (multi-point stochastic inversion tool (MPSI) from ArkCls Ltd. / Earthworks Reservoir Ltd.). More information about the geostatistical simulation is provided in Appendix B.

We transformed impedances to porosities for all 90 simulations using an empirical best linear fit derived from impedances and porosities from well U1414 (Figure B12; Harris et al., 2013b). With 90 simulated porosities per seismogram, we then quantified the probability of occurrence for 10%, 50% and 90% (P10, P50 and P90) that the restored thicknesses, using Equation 2, were less than 115 m, 204 m and 370 m (e.g., if > 81 restored thicknesses were < 115 m, than that location has a >90%

probability of having lost solids to the upper plate according to the 115 m cut-off threshold). For those locations that meet such probability thresholds, we then took the median of the remaining restored thicknesses, summed their deficits relative to incoming thicknesses (115 m, 204 m, and 370 m) and scaled them to km^3/km. P90 estimates for conservative (115 m), median (204 m) and upper (370 m) rates of U_{inv} = 0.1 km^3/km, 0.3 km^3/km and 0.6 km^3/km (Figure B9).

4.3 Results

If we sum A and conservative (115 m cut-off) estimates for U and subtract E, we find the mass balance of the frontal prism, ΔUP, to be ~0 km^3/km, within our uncertainties. Using the MORVEL plate velocity model for a 77 km/my orthogonal convergence rate (DeMets et al., 2010), we scale our measurements up to volume / km along trench / my (km^3/km/my; Table 1). If the basal erosion rate across the forearc (~102 km in the direction of convergence; Figure B13) is generally steady state (i.e., the rate of basal erosion is consistent), we can then scale our measurements up to the length of the forearc (to the base of the crust; Fig. DR13). Doing so, we find previous estimates of E rates to be 13 – 20 times our findings, A + U rates are not accounted for, S rates are 1.4 times our findings, and crustal losses of the upper plate, ΔUP, are 100 times our findings (Table 1).

Table 4. 1

Sediment delivery (km^3/km/my)	Basal erosion E (km^3/km/my)	Subduction S (km^3/km/my)	Accretion A+U (km^3/km/my)	ΔUpper Plate (no magma; km^3/km/my)
<u>Frontal Prism (this study)</u>				
7 – 12	0.7	7.8		

		Cut off*	A+ U_{athy}	
		115 m	0.4	-0.3
		204 m	0.7	0
		370 m	2.4	1.7
			A+U_{inv}	
		115 m	1.2	0.5
		204 m	2.3	1.6
		370 m	5.1	4.3
Forearc[#] (this study)				
7 – 12	7.8	87	4.5 – 13.3[§]	-3.3 – 5.5[§]
Forearc (offshore Nicoya Peninsula; Vannucchi et al., 2003)				
17	105	122	0	-105
Forearc (offshore Osa Peninsula; Vannucchi et al., 2013)				
17	153	122	0	-153

*Cut off thickness of hemipelagics used for missing hemipelagic previously accreted / underplated mass budget. 3σ below median, median, and 3σ above median.

[#] Totals from frontal prism scaled to total length of forearc subduction interface (~112 km).

[§] Totals from conservative estimates (cut off = 115 m).

4.4 Discussion

By demonstrating that thin incoming sediments, ~0.3 – 0.5 km, variably accrete along strike (Figure 4.3), with the megathrust structural position at variable hemipelagic depths (Figure 4.2), we augment the drilling results from IODP Exp. 344, which recovered incoming sediments stacked and thrust within the frontal prism (Harris et al., 2013b). The megathrust does not seem to drop into the pelagics within ~10 km of the trench (Figure 4.2), possibly due to their increased frictional strength relative to the hemipelagics at frontal prism pressures and temperatures (Kurzawski et al., 2016). Regardless, if even thin incoming hemipelagic sediments accrete, than the frontal prism is an accretionary prism, as suggested by Bangs et al., (2016), rather than a contractional structure composed of slope debris (von Huene et al., 2004). Similar, but with greater spacing and thickness, accretionary and shortening structures are imaged in the middle prism (Bangs et al., 2016). These findings imply that other margins with thin incoming sediments, typically considered “non-accretionary” or “erosive”, need a reassessment of their mass budgets to include an accretionary budget (Clift and Vannucchi, 2004).

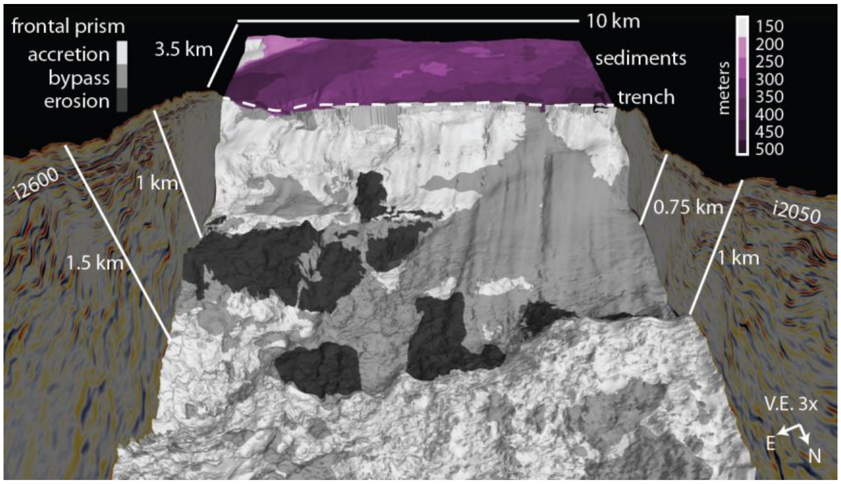

Figure 4.3 Upslope perspective of accretion, basal erosion and sediment subduction. Purples denote incoming sediment thicknesses. Inlines 2600 and 2050 shown for reference. Dash white line marks trench axis. White (accretion), grey (sediment subduction) and dark grey (basal erosion) shown overlaying megathrust horizon.

Basal erosion is collocated with the graben side of plate bending faults under the frontal prism, where if a high-angle bending fault is landward-dipping, basal erosion occurs down dip, whereas seaward-dipping, basal erosion occurs up dip (Figure 4.2A vs. Figure 4.2B-D). Several lines of evidence suggest plate bending faulting here occurs landward of the trench, including a lack of horst and graben structures observed outboard of the trench (nearest horst and graben seafloor topography is >150 km along strike to the north) and a lack of outer rise seismicity (DeShon et al., 2003). This observation is related to, but a deviation from, the model proposed by Hilde (1983), where horst and graben structures are carried into the subduction system and abrade the basal portions of the prism. Our findings negate any trench / graben filling sediments by offsetting the megathrust after subduction, rather than the seafloor before subduction. It is unlikely that abrading is the driving mechanism, as basal erosion also occurs on seaward-dipping plate bending faults where the nascent megathrust propagates up dip (i.e., to shallower depths; Figure 4.2A and B1A). We also do not see evidence for hydrofracturing along the base, because the megathrust jumps up-section by tens to hundreds of meters, proportional to the offset by plate bending faulting (Figure 4.2 and B1), rather than incrementally migrating up-section and generating a thickening subduction channel composed of former megathrusts (von Huene et al., 2004).

Plate bending faults are observed farther down dip under the middle prism in the 3D volume (Figure B13), with some possibly collocated with upstepping portions of the megathrust (Kirkpatrick et al., 2018). The Osa Experiment (temporary local network of land and ocean bottom seismometers) recorded numerous oceanic intraplate earthquakes with tensional mechanisms offshore the Osa Peninsula, with most of them spatially and temporally correlated to aftershocks following the M_w 6.9 Quepos Earthquake (i.e., such events were located within the seismogenic zone; Figure B12; DeShon et al., 2003). These observations suggest that basal erosion driven by plate bending faulting likely continues at greater depths; however, the rate at which it erodes is less constrained. If slab pull stresses and the rate of bending are somewhat steady state in the dip direction over the subduction system, then our erosion rate scales up to 7.8 km^3/km/my (Table 4.1) and thus basal erosion cannot wholly account for trench embayment and slope subsidence, even without considering underplating at greater depths (Table 4.1). We suggest trench embayment is also taken up by shortening across the forearc, including ~36 km of Pliocene – Pleistocene shortening across the inner forearc Fila Costena Thrust Belt (Sitchler et al., 2007) and >6 – 10 km of Pleistocene shortening across the outer forearc (Edwards et al., 2018a) and that slope subsidence is also linked to plate dynamic changes (Panama Fracture Zone migration) and subducting topography (MacMillan et al., 2004; Edwards et al., 2018a).

4.5 Conclusions

Our results show that even thin subducting sediments (<0.5 km) can be variably accreted and underplated along strike and that plate bending faulting under the upper plate can drive basal erosion. We find an approximate balance between accretion and erosion within ~10 km of the trench. Based on our direct observations, we find basal erosion rates to be 13 – 20 times less than previous estimates, accretion is not accounted for and total crustal losses to be 100 times less than previous estimates. Our results suggest a reassessment of forearc mass budgets globally.

Appendix A

Chapter 3 Supplementary

Methods

3D seismic reflection data

The 3D seismic reflection dataset was acquired aboard the R/V Marcus G. Langseth in 2011 using a source of two 27-gun arrays spaced 75 m apart and four 6 km long streamers spaced 150 m apart. The two 27-gun array fired every 25 m in flip-flop mode and had a volumetric displacement of 3200 liters. Each streamer consisted of 468 channels with 12.5 m channel spacing. Data were recorded for 8 s at a 2-ms sample rate. Subsequent processing of the data removed multiples and suppressed noise using normal seismic processing workflows, including: high pass and band pass filtering, noisy trace removal, spherical divergence correction, amplitude gain control, velocity analysis, deconvolution, stacking and a post-stack time migration performed by CGGVeritas and Repsol in Madrid, Spain. These data were then used to generate a 3D velocity model that was utilized in a full pre-stack depth migration performed by Repsol in The Woodlands, TX. The resulting depth-migrated dataset consists of 12.5 x 18.75 m bins with ~60 fold and images the interface between the Cocos and overlying Caribbean plates down to depths >10 km.

Post processing data conditioning

Dip and azimuth data were calculated for every sample along every trace within the volume using the Fast Fourier Transform (FFT) algorithm within

OpendTect v6.0.6 software26. The FFT iteratively transformed a moving sub-cube of 5x5x5 samples (inlines x crosslines x depth; relative to the sample and trace of interest) into the 3D Fourier Domain and found samples along adjacent traces with the same phase within the designated window. Once adjacent samples with the same phase are found, the apparent dip and azimuth (either inline or crossline direction) are recorded for that sample along that trace. This results in 3D surfaces of constant phase as recorded by a 3D volume of apparent dip and azimuth data, referred to as a steering cube, that should represent apparent geologic structure. This steering cube was then used to guide a 2x2 median filter that smoothed amplitudes and removed noise. With the 2x2 median filtered data, another iteration of FFT 3x3x5 was performed, resulting in a smoother, less noisy steering cube that preserves structure.

Volumetric attributes

Mapping efforts were performed within OpendTect v6.0.6 on the 2x2 median filtered data and were augmented by the FFT 3x3x5 steering cube. Mapping was done using an iterative workflow of interpreter picks and amplitude-driven auto tracking: 1) Pre-load an area of interest with the 2x2 median filtered data, 2) load inlines and crosslines, 3) start/load megathrust horizon, 4) pick several samples along megathrust, termed seeds, that are auto tracked along that inline or crossline, 5) adjust amplitude-driven auto tracking parameters, in this case, we used correlation threshold values that ranged from ~60-95% (algorithm compared the amplitude of the last tracked pick to the next candidate pick), and search windows of ~10-50 m, 6) 3D auto track, 7) QC auto tracked horizon, undo or delete errant portions, adjust picks and/or auto tracking parameters and re-track, 8) lock tracked seeds and repeat. During amplitude-driven tracking, a sub-sample depth value (<5 m) is achieved by fitting a quadratic polynomial to a series of 5 m sample points. Once the megathrust is tracked, the horizon is gridded to fill in remaining holes, using an algorithm that is guided by the steering cube.

Measuring corrugations

Geometries were measured manually with graphical tools in Matlab and OpendTect. In Matlab, troughs and ridges were extracted from xyz elevation data using a 20 by 20 element moving window to average all z values within the square neighborhood for every element in the matrix. These neighborhood averaged z values were then subtracted from the original elevation data. The resulting matrix consists of positive values where the central z value is greater than the neighborhood average and negative when less, corresponding to topographic highs and lows respectively. This differencing matrix helped constrain troughs and ridges. The widths of each is determined as the distance from trough to trough or peak to peak, and the amplitudes as the difference in elevation between the peak and trough, as measured graphically in Matlab and OpendTect. In Matlab, widths and amplitudes were extracted along the horizon and in OpendTect, widths and amplitudes were measured along selected crosslines. Measurements in Matlab were corroborated by measurements in OpendTect and vice versa. ~30 total bedforms were measured at discrete points along the megathrust (i.e., a representative part of the corrugation was measured). Two amplitudes <1 m were excluded.

Taper analysis

We extracted the taper of the overlying wedge from the depth converted seismic reflection volume over length scales in kilometer increments measured landward from the trench (e.g., 5 km, 6 km, etc.). A taper was extracted for every inline over each increment of length scale by extracting the elevation of the seafloor, megathrust and trench per inline. The taper angle was then solved by parameterizing a right triangle for the seafloor and megathrust dip separately then summing the angles for each inline over each length scale. Figure A1 shows the results of the taper angle and seafloor and megathrust dips for 5 km of the outermost wedge (measured 5 km landward from the trench). Rougher faults have been shown to increase fault strength (Fang and Dunham, 2013), and here we observe an increase in the taper angle of the overlying wedge over poorly corrugated (12 – 14°) versus corrugated (10.5 – 11.5°) portions (Figure 3.5). An increase in taper angle along strike, if wedge properties are consistent, suggests an increase in underlying fault strength, showing that rougher portions of the megathrust are stronger than well corrugated portions.

Supplementary Figure

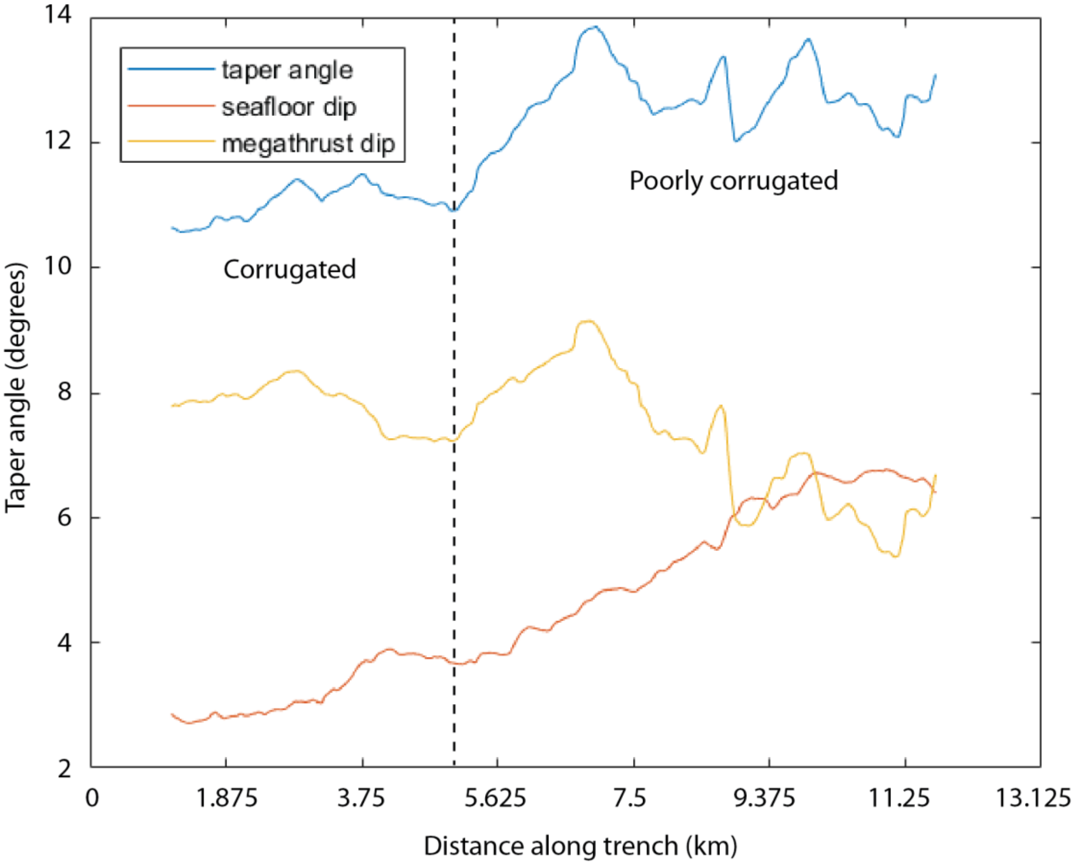

Figure A1 Taper angle, seafloor and megathrust dip along strike over 5 km of the frontal prism. The vertical dashed line marks the approximate transition from corrugated (megathrust in its original position) to poorly corrugated (megathrust in a nascent position) portions. The distance along trench is taken from each inline relative to the NW side of the volume. Note the increasing seafloor dip with increasing taper angle, suggesting the seafloor dip here is a good proxy for taper angle.

Appendix B

Chapter 4 Supplementary

Methods

Geostatistical conditional simulation of acoustic impedances

We utilized U1414 p-wave velocity data, V_p, from the P-wave caliper tool within the Whole Round Multisensor Logger, and bulk density data, ρ, taken from mass and volume determinations on cores (Harris et al., 2013c). The P-wave caliper measures P-wave velocity vertically on the sectional halves of whole cores in the horizontal direction. Both methods return measurements at different non-integer depths. We rounded depths to integers and then applied a linear interpolation between 0 and well bottom (370 m).

We then imported the well log and its physical properties and tied the well to the post stack time migrated volume (Figure B2) by applying Backus upscaling (Backus, 1962), whereby the physical properties are upscaled to seismic wavelengths. Seismic wavelengths are estimated from the seismic bandwidth and seismic velocities. There was no check-shot survey completed along the well track, so we were not able to empirically tie the depth data in the well to the time data in the seismograms. We also did not stretch or squeeze the synthetics to best fit the recorded seismograms to avoid spreading errors into wavelet estimation (White and Simm, 2003).

We calculated zero-offset acoustic impedance, I, which is,

$$\mathrm{I} = \rho * \mathrm{V_p} \tag{1}$$

where ρ is bulk density and $\mathrm{V_p}$ is P-wave velocity. Reflectivity is then the difference between adjacent impedances normalized by their sum,

$$\mathrm{r_t} = \frac{I_{t+1} - I_t}{I_{t+1} + I_t} \tag{2}$$

Reflectivity, r_t, is then used to estimate a source wavelet by forward modeling synthetic seismograms, s_t, from a convolution of the source wavelet, w_t, and r_t.

$$\mathrm{s_t} = \mathrm{w_t} * \mathrm{r_t} \tag{3}$$

We performed a best fit (minimized cross-correlation coefficient) of the synthetic to recorded seismograms by both estimating deterministic wavelets over varying lengths (60 – 120 ms), tapering and then rotating to a best fit, and rotating 40 Hz Ricker wavelets (60 – 120 ms) to best fits. We achieved a best fit with a 60 ms Ricker wavelet rotated 22 degrees (cross-correlation coefficient of 0.46) that had a synthetic to seismic scalar of 353940 (Figure B2).

We then employed a Coloured Inversion (Lancaster and Whitcombe, 2000) to estimate the maximum distance between samples at which variance is constant (semivariogram). The Coloured Inversion produces a model of relative acoustic impedances by designing an operator with a -90° phase that maps the mean seismic spectrum to the mean acoustic impedance spectrum from well U1414. This operator is then convolved with the recorded seismograms to produce an inverted model of relative impedances (Lancaster and Whitcombe, 2000). Such relative impedances are not layer properties, but are relative layer properties, and as such, cannot be transformed to physical properties such as porosity. With these relative impedances, we then performed a horizontal semivariogram analysis (Matheron, 1963) by extracting relative impedances across the seafloor / megathrust horizon, the top of the pelagics and a horizon intermediate between the two, and best fitting models that describe the maximum sample distance at which the variance of relative impedance is the same. We found this maximum sample distance, ~700 m, to be consistent in the inline, crossline and diagonal directions and therefore utilized an isotropic exponential semivariogram model. We estimated the vertical semivariogram by measuring the thickness of lithologic beds in well U1414 in time, ~10 – 20 ms. The semivariograms are then used to produce an error grid by kriging (Krige, 1951), which is a mapping of standard deviation away from well U1414. The semivariograms used as input to kriging have their sills standardized to 1, which results in a standard deviation of 0 near the well and increasing standard deviation away from the well up to 1. This constrains inverted impedances near well U1414 to values close to well values, but with increasing distance from the well, increases the weight of the recorded seismograms in the inversion.

We then built a 3D a priori model of acoustic impedances by projecting impedances from U1414 across the 3D seismic volume between and conformal to bounding horizons (Figure B11), resulting in a broadband model of acoustic impedances. Bounding horizons included the seafloor / megathrust, top of the pelagics and top of the lavas.

With the estimated source wavelet, 3D a priori model of impedances and error grid, we then performed a deterministic, model-based inversion for absolute impedance, where the broadband model impedances are smoothed (Backus upscaling; Backus, 1962) and are iteratively updated to a best fit by a generalized linear inversion (Hampson and Russell, 1984). However, because underthrust sediments exhibit strong heterogeneity (e.g., discrete regions of pore overpressure), smoothed modeling results from the deterministic approach fail to capture this heterogeneity (Francis, 2006). Furthermore, the model-based inversion is inherently non-unique (the deterministic result produces mean impedance results) , we extended our analysis to a stochastic approach whereby we produce many probable, best fit impedance models.

We utilized oil and gas industry software provided to us (Multi-Point Stochastic Inversion Plugin; Earthworks Environment and Resources Inc. / ArkCLS Inc.) to perform a suite of 90 impedance simulations. The software utilizes a hybrid inversion approach that improves the computational efficiency (important for this study as 660,000 seismograms with 1100 samples were inverted; Francis, 2003). The initial a priori model is updated by an inversion scheme that uses a 3D Fast Fourier Transform (FFT) spectral simulation within the seismic reflection band width (Pardo-Igúzquiza and Chica-Olmo, 1993). A forward 3D FFT is first applied to the whole a priori model, and then each realization is performed by adding a new random phase (Francis, 2005) and proceeding through the model and volume of seismograms randomly with an inverse FFT. The random walk is driven by a Monte Carlo random number generator (Francis, 2006). There resulting impedances are then conditioned to well U1414 impedances by kriging.

With this suite of 90 unique impedance realizations, we then used the empirical relationship from well U1414 of impedance to porosity (Figure B12) to transform these realizations to porosity, with boundary conditions of 1e^6 – 8e^6 (impedance cut-offs). We then restored thicknesses for each realization based on these porosities, thus resulting in 90 restored thickness values for each seismogram location. We then estimated the probability of occurrence for 10%, 50% and 90% for each location having lost solids to the upper plate (e.g., if 81 out of 90 realizations (90%) produce a restored thickness that is less than a certain cut-off criteria, than that sample location has a 90% probability of having loss solids to the upper plate according that cut-off). The values for each cut-off thickness were 115 m, 204 m and 370 m (3σ below median, median and 3σ above median of the incoming hemipelagic thicknesses).

Supplementary Figures

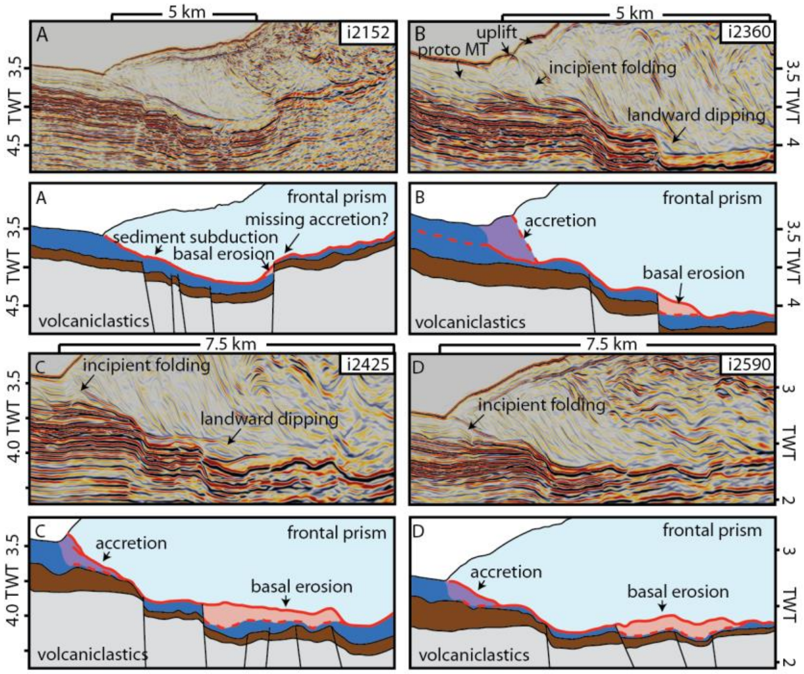

Figure B1 Inlines 2152, 2360, 2425 and 2590 from post-stack, time migrated volume. Interpreted and uninterpreted equivalent inlines from Figure 4.2 (see reference basemap from Figure 4.2E for locations) shown with time domain imaging. Time domain imaging misrepresent the geometry of the subducting plate, but better image the intensely deformed internal structure of the frontal prism. Note the tightly spaced, imbricated stacks of landward-dipping reflections within the frontal prism, particularly within eroded packages (e.g., B and C).

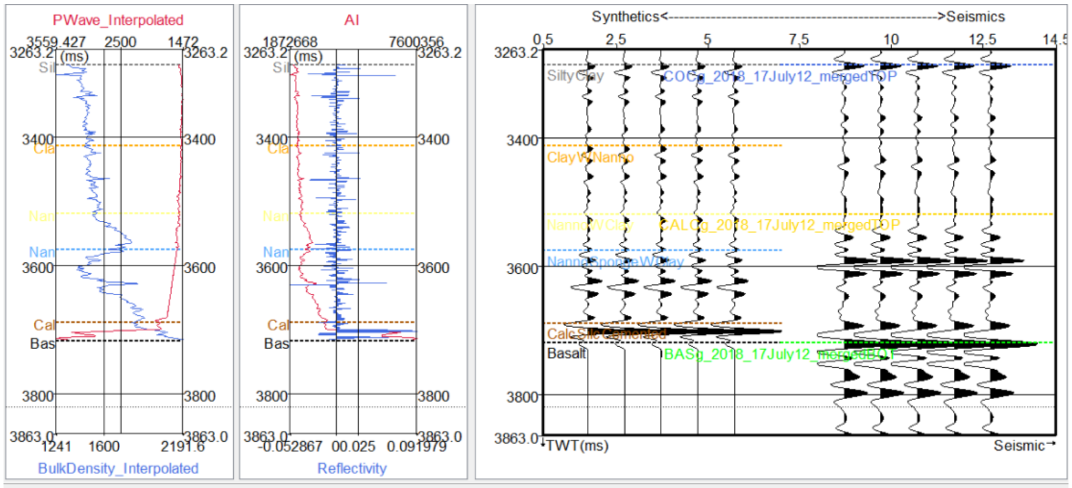

Figure B2 Well-to-seismic tie. From left to right: interpolated compressional wave (p-wave) and bulk density, acoustic impedance and coefficient of reflectivity, and 5 synthetic and observational traces, all with either unit markers from U1414 or with tracked horizons from 3D seismic volume. P-wave velocity was measured with the PWL instrument onboard Exp. 344 and bulk density was calculated by measuring the wet and dry masses and volumes of discrete samples (Harris et al., 2013). Acoustic impedance is the product of p-wave velocity and bulk density, and reflectivity at zero-offset is the layer impedance difference of neighboring layers divided by their sum. A ricker wavelet with a peak amplitude of 1 was phase rotated until a best fit between synthetic traces and seismic traces with a correlation of 0.46.

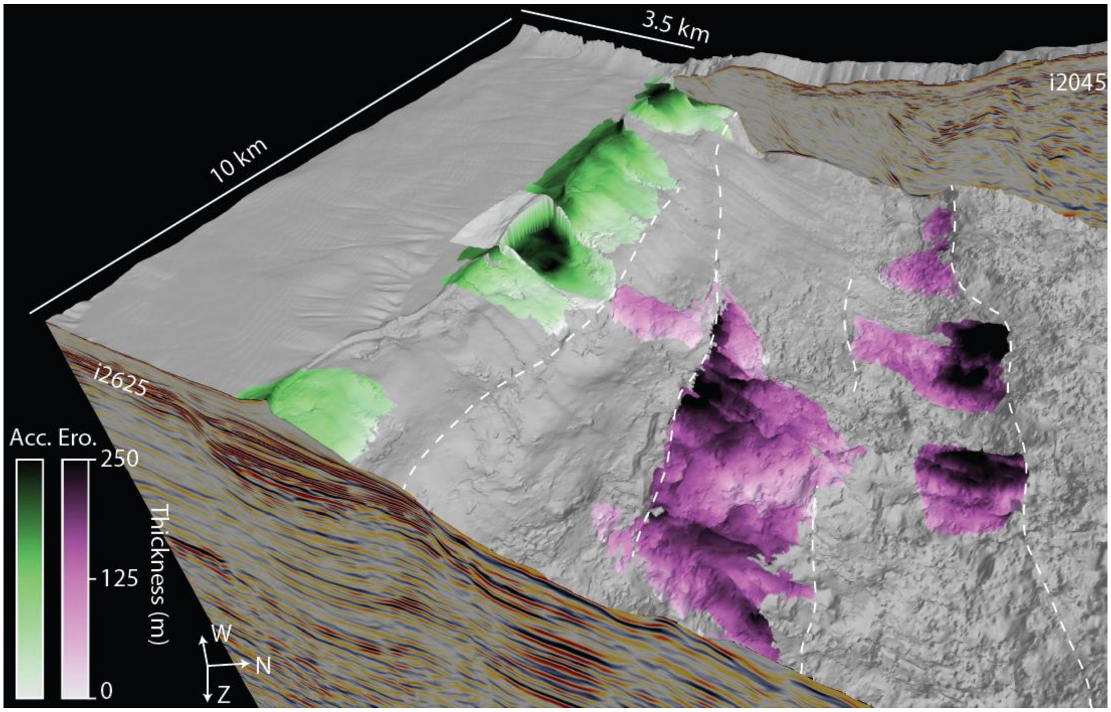

Figure B3 Accretionary and erosional sediment thicknesses from mapping. Accretionary thicknesses are shown as greens and erosional thicknesses are shown as purples overlain over greyed out megathrust and seafloor. Major plate bending faults are approximated with dashed white line. Perspective is looking west. Vertical exaggeration is 2x. Inlines 2045 and 2625 from the depth converted volume are shown.

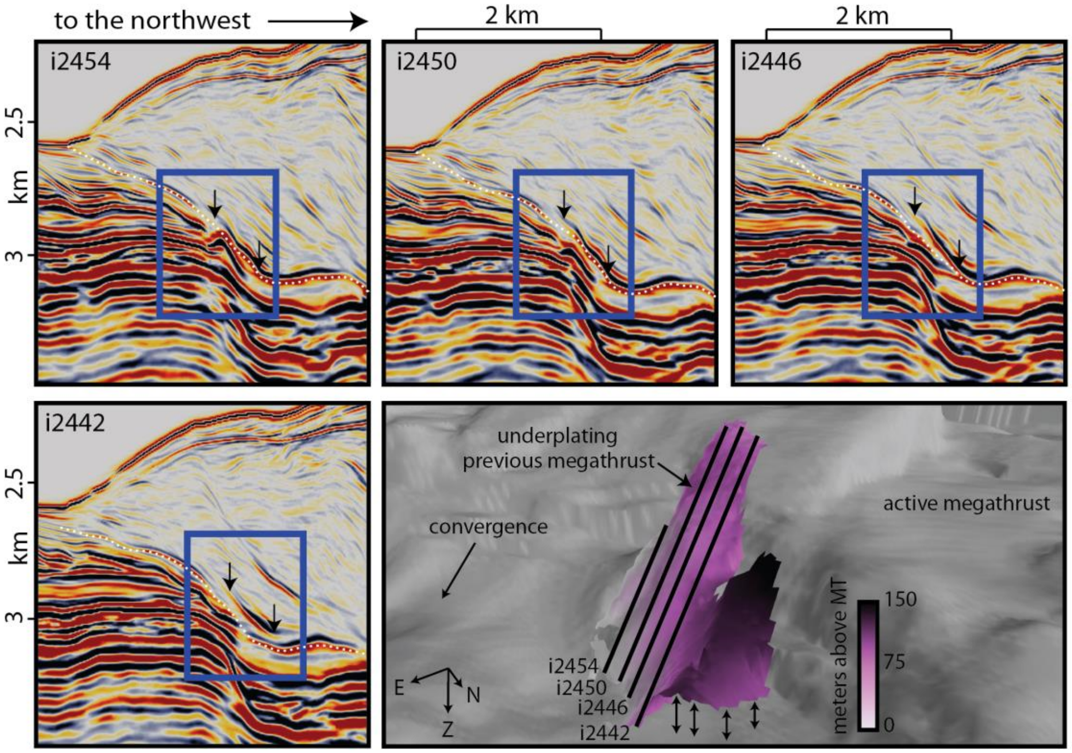

Figure B4 Inlines 2442, 2446, 2450 and 2454 imaging underplating. Possible underplating imaged as a reverse polarity reflector splayed off the megathrust and striking orthogonal to deformation front. 4 inline frames from the top left to the right moving from the SE to the NW. Inlines extracted from DSMF4x6 data and displayed at 3x vertical exaggeration. Blue boxes show the approximate area where the splaying reflector deviates progressively from the megathrust. Dashed white line marks current megathrust position. Bottom right frame showing the reflector as a horizon with vertical distance from active megathrust overlain as purples to whites (meters above megathrust).

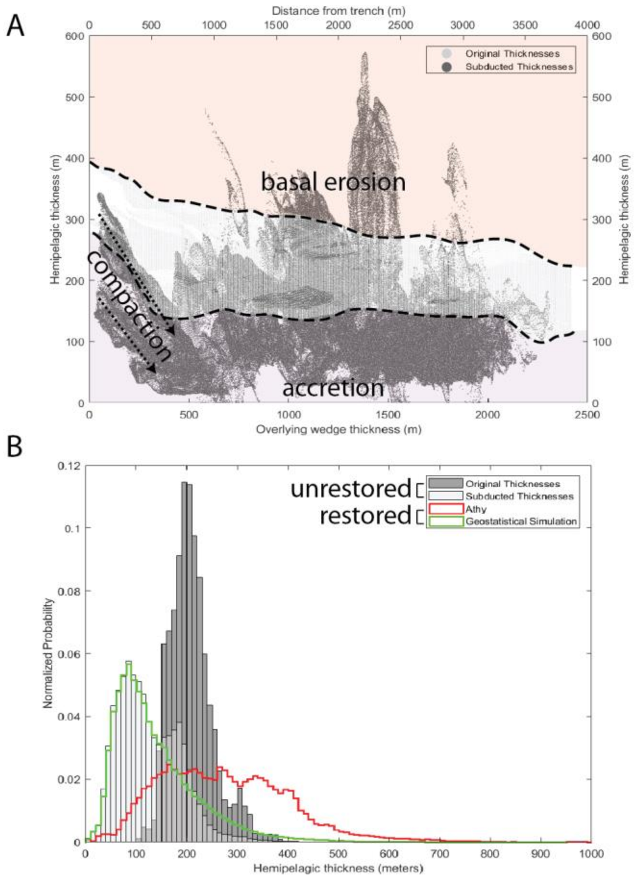

Figure B5 Before and after subducted hemipelagic and restored thicknesses. A. Distribution of incoming (light grey dots within dashed lines referenced along strike and distance outboard from trench) and subducted (dark grey dots referenced along strike and to overlying wedge thicknesses) thicknesses (unrestored). Subducted thicknesses greater than incoming thicknesses fall within the light orange region and have likely added thickness by basal erosion. Linear slope of decreasing subducted thicknesses within first 500 meters of the trench is likely due to compaction. Subducted thicknesses down to just tens of meters have likely lost thickness to the upper plate by accretion. B. Distribution of unrestored and restored hemipelagic thicknesses.

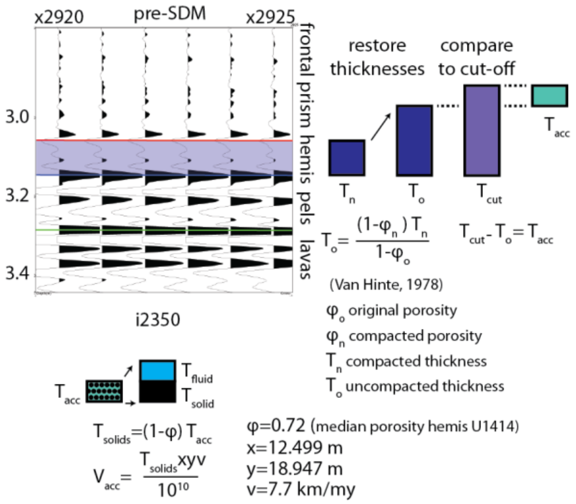

Figure B6 Schematic of methods used to restore thicknesses and estimate material exchange volumes. Also included are six example crosslines (e.g., x2920, x2921, etc.) from depth converted volume.

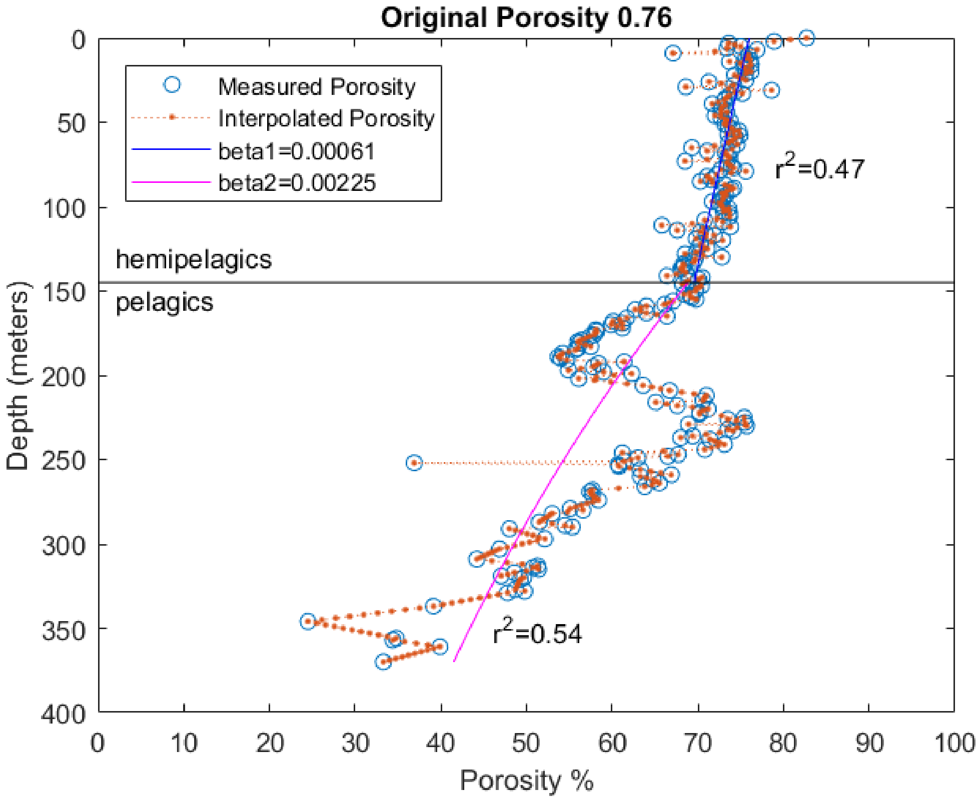

Figure B7 Athy (1930) exponential best fit to porosity / depth data from well U1414. Hemipelagic / pelagic lithostratigraphic boundary taken from well U1414 (Harris et al., 2013c). Linear interpolation applied to porosity data is shown. Least squares regression coefficients shown for both hemipelagic and pelagic best fit and associated beta coefficients.

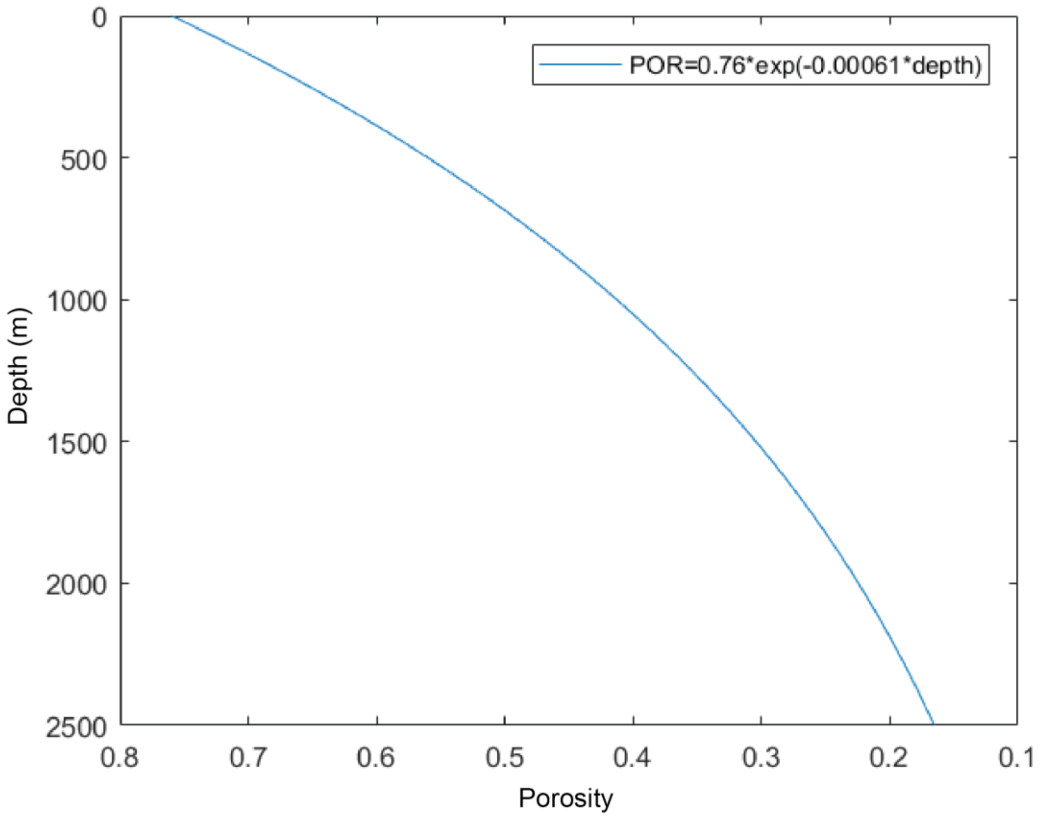

Figure B8 Athy (1930) exponential porosity / depth model. Best fit model from hemipelagics shown to 2500 meter below seafloor depths. Porosities down to <0.2 are modeled.

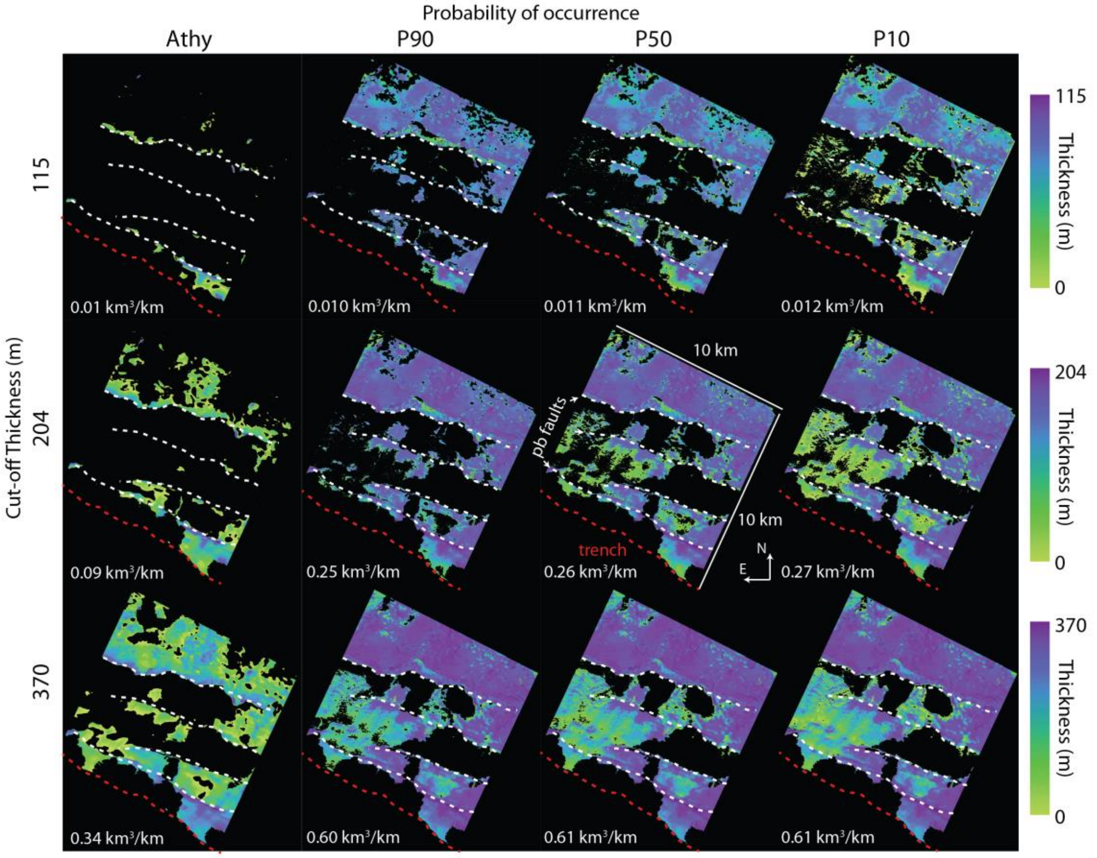

Figure B9 Model results for U restored thicknesses from Athy (1930) and geostatistical conditional simulations with various probability of occurrences Restored thicknesses for every seismogram from Athy (1930; leftmost column) and geostatistical conditional simulation for each probability of occurrence (10%, 50% and 90%) shown for cut-off thicknesses of 115 m (top row), 204 m (middle row) and 370 m (lower row). Red dashed line approximates the trench. White dashed lines approximate major plate bending faults. Restored thickness scales shown to the right. Subduction direction is generally perpendicular to the trench (to the NE).

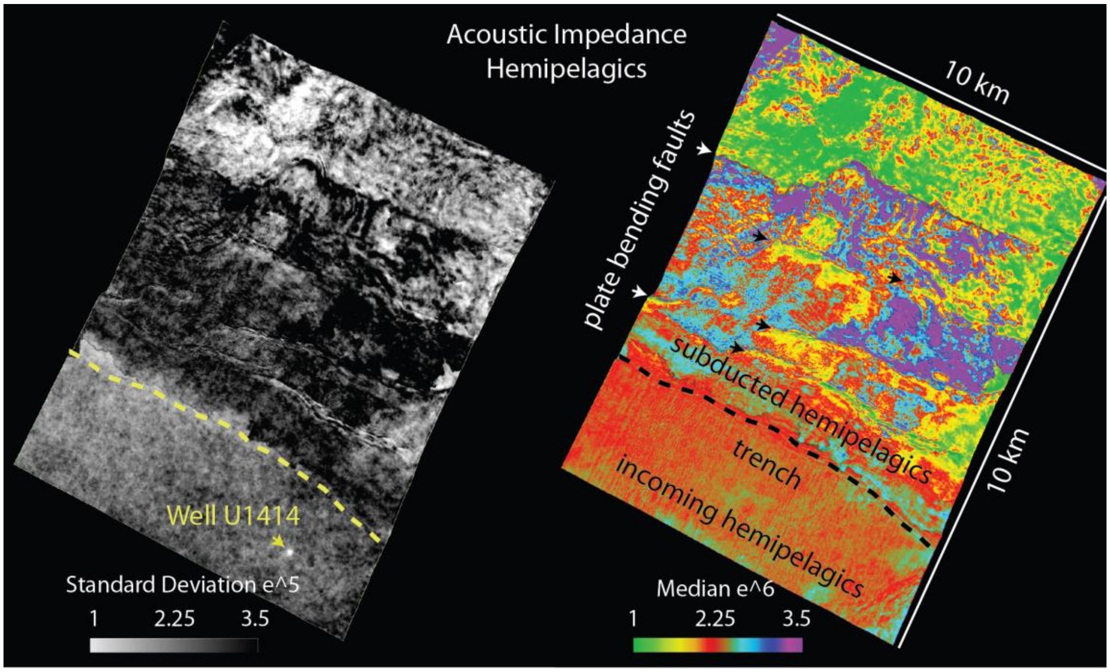

Figure B10 Median and standard deviation acoustic impedance results from 90 geostatistical conditional simulations. Figure at left shows standard deviations per seismogram (from 90 impedance simulations per seismogram) and figure at right shows median impedances per seismogram. Note the low standard deviation at the well site. Also note how median impedances generally mirror horst and graben structure (i.e., are bounded by plate bending faults (shown with short white and black arrows).

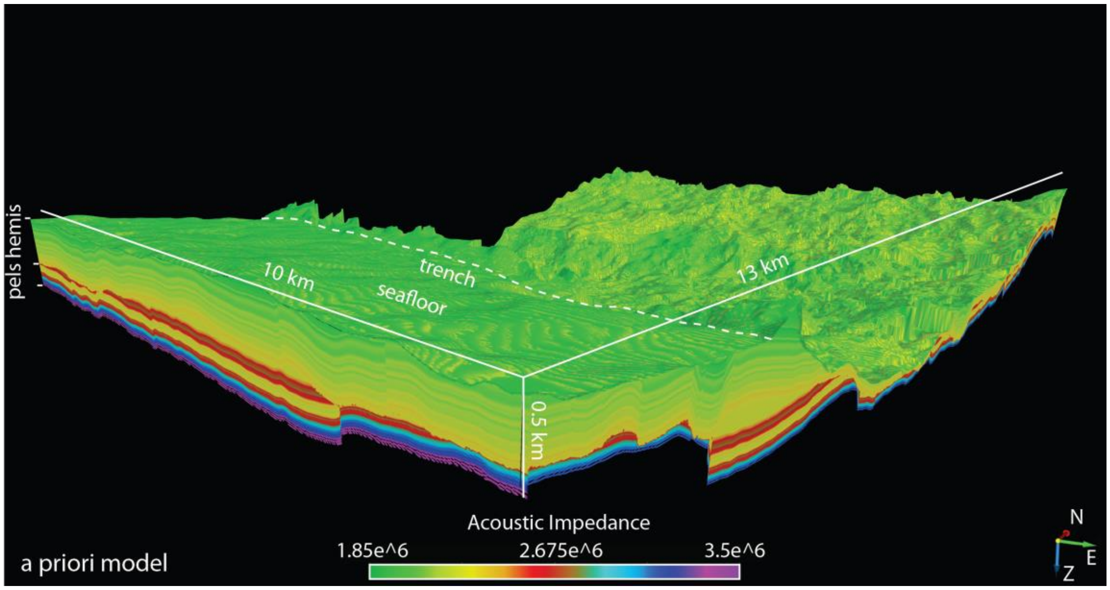

Figure B11 Low frequency, a priori model of acoustic impedances. Model extends ~13 x 10 km2 and is shown projected onto inline 2620 and crossline 2450, with thicknesses up to ~500 m. Approximate hemipelagic and pelagic lithostratigraphic boundaries shown at left. Note how pelagics generally has a larger range of impedances, while hemipelagics are remarkably consistent (~1.85 – 2.25 e^6 kg / m^2s).

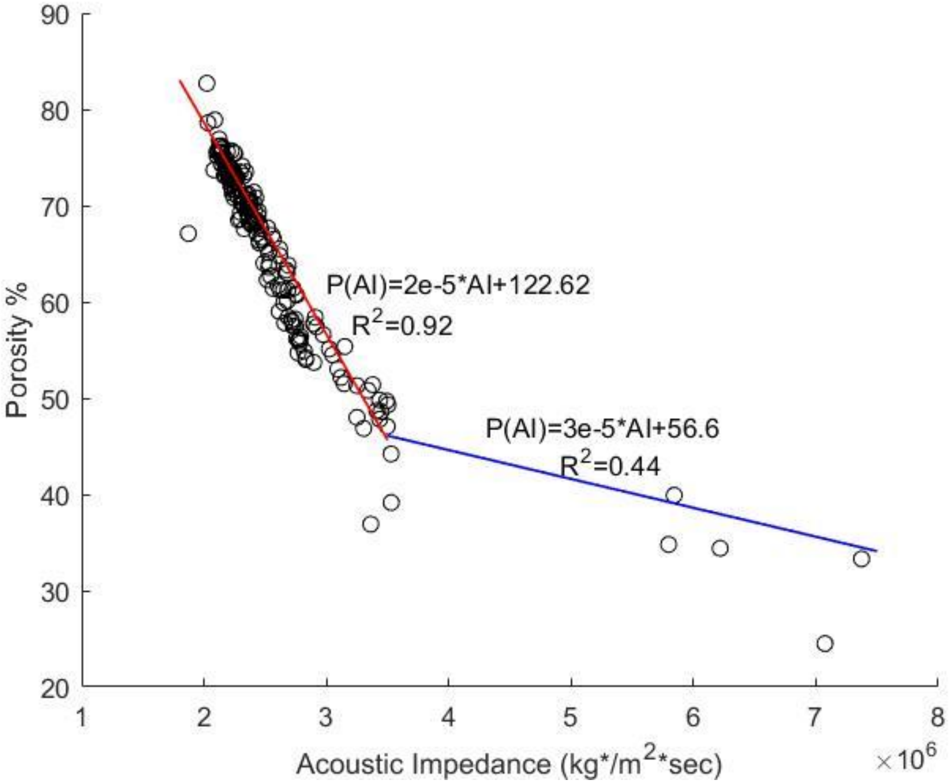

Figure B2 Acoustic impedance to porosity best linear fit from well U1414. Linear best fit to low impedances (2e5 – 3.5e6) is shown with red line and best fit to higher impedances (>3.5e6) is shown with blue line. Least squares regression coefficients shown for both best fit models.

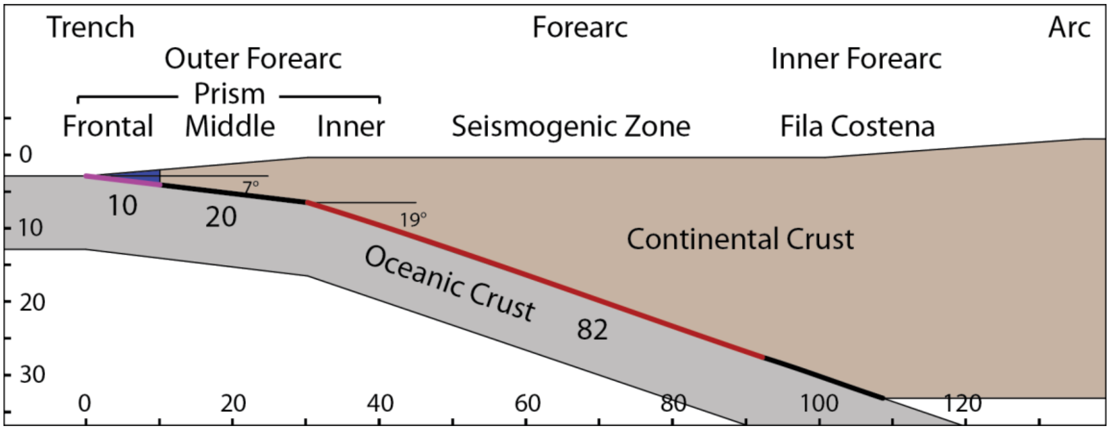

Figure B33 Model of trench perpendicular length of megathrust across forearc crust. First 30 km dip is constrained by 3D depth converted seismic reflection volume, remaining length of interface is constrained by 35 km thickness of crust and 19° plate dip (DeShon et al., 2003). Seismogenic zone is highlighted in red and frontal prism in purple. Tick marks along figure edges denote depth and length in kilometers.

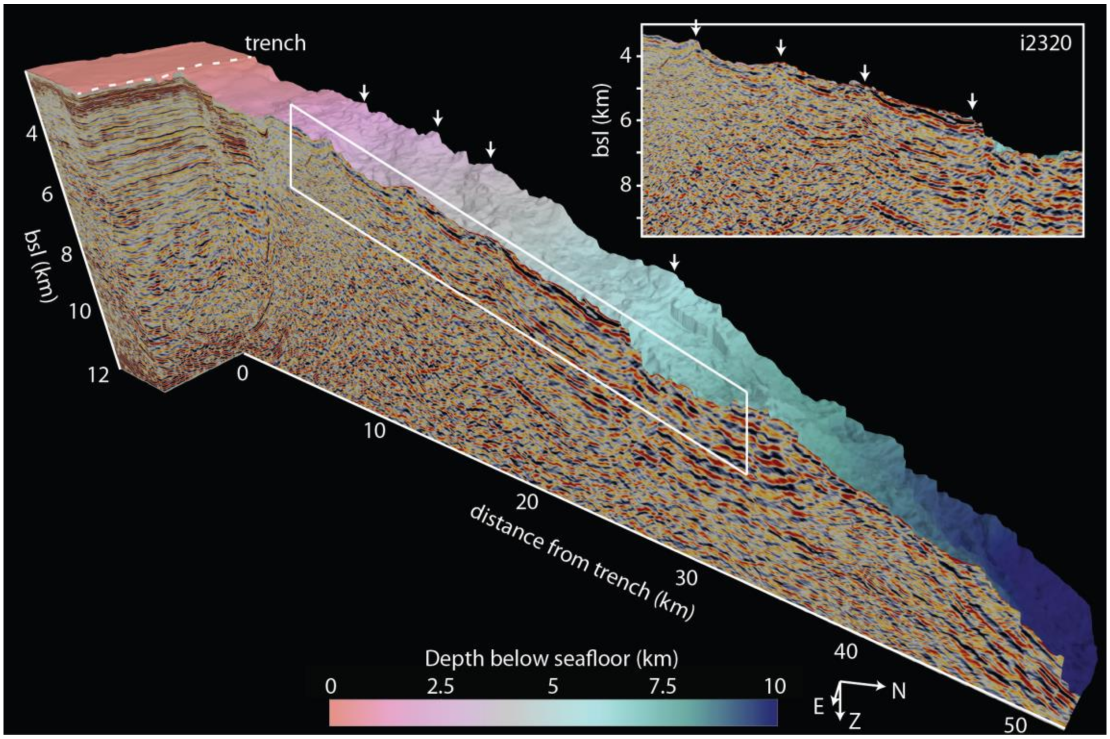

Figure B44 Plate bending faults at greater depths. 3D perspective of plate bending faults (denoted by arrows) and their morphologic expression across the megathrust (as ridges). Colors on megathrust show depth my seafloor, or thickness of overlying wedge. Inset is a snapshot of inline 2320 with dip-steered median filtered data generated by a 4 x 6 stepout (inline x crossline).

Bibliography

Abratis, M., and Worner, G., 2001, Ridge collision, slab-window formation and the flux of Pacific asthenosphere into the Caribbean realm: Geology, v. 29, no. 2, p. 127–130.

Adamek, S., and Tajima, F., 1987, Seismic rupture associated with subduction of the Cocos Ridge: Tectonics, v. 6, no. 6, p. 757–774.

Aki, K., 1984, Asperities, Barriers, Characteristic Earthquakes and Strong Motion Prediction: Journal of Geophysical Research, v. 89, p. 5867–5872.

Argus, D.F., Gordon, R.G., and Demets, C., 2011, Geologically current motion of 56 plates relative to the no-net-rotation reference frame: Geochemistry, Geophysics, Geosystems, v. 12, no. 11.

Arroyo, I.G., Grevemeyer, I., Ranero, C.R., and von Huene, R., 2014, Interplate seismicity at the CRISP drilling site: The 2002 Mw 6.4 Osa Earthquake at the southeastern end of the Middle America Trench: Geochemistry Geophysics Geosystems, v. 15, p. 3035–3050, doi: 10.1002/2014GC005359.Received.

Athy, L.F., 1930, Density, porosity, and compaction of sedimentary rocks: Am Assoc. Petrol. Geol. Bull., v. 14, p. 1–24.

Aubouin, J., and von Huene, R., 1985, Leg 84: Summary: Middle America Trench transect off Guatemala and Costa Rica: Initial Reports DSDP, v. 84, p. 939–957.

Azema, J., Bourgois, J., Baumgartner, P.O., Tournon, J., Desmet, A., and Aubouin, J., 1985, A Tectonic Cross-Section of the Costa Rican Pacific Littoral as a Key to the Structure of the Landward Slope of the Middle America Trench Off Guatemala: Initial Reports of the Deep Sea Drilling Project, v. 84, no. MAY, p. 831–850.

Backus, G.E., 1962, Long-wave elastic attenuation produced by horizontal layering: Journal of Geophysical Research, v. 67, no. 11, p. 4427–4440, doi: 10.1190/tle33060634.1.

Ballance, P.F., Scholl, D.W., Vallier, T.L., Stevenson, A.J., Ryan, H., and Herzer, R., 1989, Subduction of a Late Cretaceous seamount of the Louisville Ridge at the Tonga Trench: A model of normal and accelerated tectonic erosion: Tectonics, v. 8, no. 5, p. 953–962.

Bangs, N.L., 2018, The NZ3D Experiment - Adding a new dimension for understanding slow slip events: GeoPRISMS Newsletter, v. 40, no. Spring, p. 14–15.

Bangs, N.L., McIntosh, K.D., Silver, E.A., and Kluesner, J.W., 2016, A recent phase of accretion along the southern Costa Rican margin: Earth and Planetary Science

Letters, v. 443, p. 204–215, doi: 10.1016/j.epsl.2016.03.008.

Bangs, N.L., McIntosh, K.D., Silver, E.A., Kluesner, J.W., and Ranero, C.R., 2014, Fluid accumulation along the Costa Rica subduction thrust and development of the seismogenic zone: Journal of Geophysical Research, v. 120, p. 67–86, doi: 10.1002/2014JB011265.

Barckhausen, U., Ranero, C.R., von Huene, R., Cande, S.C., and Roeser, H.A., 2001, Revised tectonic boundaries in the Cocos Plate off Costa Rica: Implications for the segmentation of the convergent margin and for plate tectonic models: Journal of Geophysical Research, v. 106, no. B9, p. 207–220, doi: 10.1029/2001JB000238.

Bletery, Q., Thomas, A.M., Rempel, A.W., Karlstrom, L., Sladen, A., and Barros, L. De, 2016, Mega-earthquakes rupture flat megathrusts: Science, v. 354, no. 6315, p. 1027–1031.

Boston, B.B., Moore, G.F., Nakamura, Y., and Kodaira, S., 2014, Outer-rise normal fault development and influence on near-trench décollement propagation along the Japan Trench, off Tohoku: Earth, Planets and Space, v. 66, no. 1, p. 135, doi: 10.1186/1880-5981-66-135.

Brodsky, E.E., Kirkpatrick, J.D., and Candela, T., 2016, Constraints from fault roughness on the scale-dependent strength of rocks: Geology, v. 44, no. 1, p. 1–4, doi: 10.1130/G37206.1.

Buffler, R.T., 1982, Geologic structure of the forearc region off the west coast of Costa Rica in the vicinity of the Nicoya Peninsula - Results of a multifold seismic reflection survey: Univ Texas Bull, , no. 37, p. 56p.

Buiter, S.J.H., Govers, R., and Wortel, M.J.R., 2001, A modelling study of vertical displacements at convergent margins: Geophys. J. Int., v. 147, no. 2, p. 415–427, doi: 10.1046/j.1365-246X.2001.00545.x.

Burke, K., 1988, Tectonic evolution of the Caribbean: Ann. Rev. Earth Planet. Sci., v. 16, p. 201–230.

Calvert, A.J., 2004, Seismic reflection imaging of two megathrust shear zones in the northern Cascadia subduction zone: Nature, v. 428, no. March, p. 163–167, doi: 10.1038/nature02346.1.

Candela, T., and Brodsky, E.E., 2016, The minimum scale of grooving on faults: Geology, , no. 8, p. 1–4, doi: 10.1130/G37934.1.

Cann, J.R., Blackman, D., Smith, D.K., McAllister, E., Janssen, B., Mello, S., Avgerinos, E., Pascoe, A.R., and Escartín, J., 1997, Corrugated slip surfaces formed at ridge-transform intersections on the Mid-Atlantic Ridge: Nature, v. 385, p. 329–332.

Cartwright, J.A., and Huuse, M., 2005, 3D seismic technology: The geological "Hubble": Basin Research, v. 17, no. 1, p. 1–20, doi: 10.1111/j.1365-2117.2005.00252.x.

Catuneanu, O., 2002, Sequence stratigraphy of clastic systems: Concepts, merits, and pitfalls: Journal of African Earth Sciences, v. 35, no. 1, p. 1–43, doi: 10.1016/S0899-5362(02)00004-0.

Catuneanu, O., Galloway, W.E., Kendall, C.G.S.C., Miall, A.D., Posamentier, H.W., Strasser, A., and Tucker, M.E., 2011, Sequence Stratigraphy: Methodology and Nomenclature: Newsletters on Stratigraphy, v. 44, no. 3, p. 173–245, doi: 10.1127/0078-0421/2011/0011.

Chaves, E.J., Duboeuf, L., Schwartz, S.Y., Lay, T., and Kintner, J., 2017, Aftershocks of the 2012 Mw 7.6 Nicoya, Costa Rica, earthquake and mechanics of the plate interface: Bulletin of the Seismological Society of America, v. 107, no. 3, p. 1227–1239, doi: 10.1785/0120160283.

Chopra, S., and Marfurt, K.J., 2013, Preconditioning seismic data with 5D interpolation for computing geometric attributes: Interpreter's Corner, , no. December, p. 1456–1459.

Clark, C.D., 1993, Mega-scale glacial lineations and cross-cutting ice-flow landforms: Earth Surface Processes and Landforms, v. 18, p. 1–29.

Clark, C.D., Tulacyzk, S., Stokes, C.R., and Canals, M., 2003, A groove-ploughing theory for the production of mega-scale glacial lineations, and implications for ice-stream mechanics: Journal of Glaciology, v. 49, no. 165, p. 240–256.

Clift, P.D., and MacLeod, C.J., 1999, Slow rates of subduction erosion estimated from subsidence and tilting of the Tonga forearc: Geology, v. 27, no. 5, p. 411–414, doi: 10.1130/0091-7613(1999)027<0411:SROSEE>2.3.CO;2.

Clift, P.D., and Vannucchi, P., 2004, Controls on Tectonic Accretion Versus Erosion in Subduction Zones : Implications for the Origin and Recycling of the Continental Crust: American Geophysical Union, v. 42, p. 1–31, doi: 10.1029/2003RG000127.1.

Clift, P.D., Vannucchi, P., and Morgan, J.P., 2009, Crustal redistribution, crust-mantle recycling and Phanerozoic evolution of the continental crust: Earth-Science Reviews, v. 97, no. 1–4, p. 80–104, doi: 10.1016/j.earscirev.2009.10.003.

Collins, L.S., Coates, A.G., Jackson, J.B.C., and Obando, J.A., 1995, Timing and rates of emergence of the Limon and Bocas del Toro basins: Caribbean effects of Cocos Ridge subduction? GSA Special Papers, v. 295, p. 263–289.

Corrigan, J., Mann, P., and Ingle, J.C.J., 1990, Forearc response to subduction of the

Cocos Ridge, Panama-Costa Rica: Geological Society of America Bulletin, v. 102, no. 5, p. 628–652.

Coulbourn, W.T., 1982, 1. Introduction, Summary, and Explanatory Notes, the Middle America Trench, Deep Sea Drilling Project Leg 67: Initial Reports DSDP 67, p. 5–25.

DeMets, C., 2001, A new estimate for present-day Cocos-Caribbean plate motion: Implications for slip along the Central American volcanic arc: Geophysical Research Letters, v. 28, no. 21, p. 4043–4046, doi: 10.1029/2001GL013518.

Demets, C., Gordon, R.G., Argus, D.F., and Stein, S., 1994, Effect of recent revisions to the geomagnetic reversal time scale on estimates of current plate motions: Geophysical Journal International, v. 21, no. 20, p. 2191–2194.

DeMets, C., Gordon, R.G., Argus, D.F., and Stein, S., 2010, Geologically current plate motions: Geophysical Journal International, v. 181, no. 1, p. 1–80.

DeShon, H.R., Schwartz, S.Y., Bilek, S.L., Dorman, L.M., González, V., Protti, M., Flueh, E.R., and Dixon, T.H., 2003, Seismogenic zone structure of the southern Middle America Trench, Costa Rica: Journal of Geophysical Research, v. 108, no. B10, doi: 10.1029/2002JB002294.

Dickinson, W., 1970, Global Tectonics: Science, v. 168, no. 3936, p. 1250–1259.

Dieterich, J.H., and Smith, D.E., 2009, Nonplanar Faults: Mechanics of Slip and Off-fault Damage: Pure appl. geophys., v. 166, p. 1799–1815, doi: 10.1007/s00024-009-0517-y.

Dinter, D.A., 1998, Late Cenozoic extension of the Alpine collisional orogen , northeastern Greece : Origin of the north Aegean basin: GSA Bulletin, v. 110, no. 9, p. 1208–1226.

Dominguez, S., Lallemand, S.E., Malavieille, J., and Von Huene, R., 1998, Upper plate deformation associated with seamount subduction: Tectonophysics, v. 293, no. 3–4, p. 207–224, doi: 10.1016/S0040-1951(98)00086-9.

Dominguez, S., Malavieille, J., and Lallemand, S.E., 2000, Deformation of accretionary wedges in response to seamount subduction: Insights from sandbox experiments: Tectonics, v. 19, no. 1, p. 182–196, doi: 10.1029/1999TC900055.

Edwards, J.H., Kluesner, J.W., Silver, E.A., and Bangs, N.L., 2018a, Pleistocene vertical motions of the Costa Rican outer forearc from subducting topography and a migrating fracture zone triple junction: Geosphere, v. 14, no. 2, p. 1–25, doi: 10.1130/GES01577.1.

Edwards, J.H., Kluesner, J.W., Silver, E.A., Brodsky, E.E., Brothers, D.S., Bangs, N.L., Kirkpatrick, J.D., Wood, R., and Okamoto, K., 2018b, Corrugated megathrust revealed offshore from Costa Rica: Nature Geoscience, v. 11, p.

197–202, doi: 10.1038/s41561-018-0061-4.

Engelder, J.T., 1974, Microscopic Wear Grooves on Slickensides: Indicators of Paleoseismicity: Journal of Geophysical Research, v. 79, no. 29, p. 4387–4392.

Fang, Z., and Dunham, E.M., 2013, Additional shear resistance from fault roughness and stress levels on geometrically complex faults: Journal of Geophysical Research: Solid Earth, v. 118, no. June, p. 3642–3654, doi: 10.1002/jgrb.50262.

Fisher, D.M., Gardner, T.W., Sak, P.B., Sanchez, J.D., Murphy, K., and Vannucchi, P., 2004, Active thrusting in the inner forearc of an erosive convergent margin, Pacific coast, Costa Rica: Tectonics, v. 23, p. 1–13, doi: 10.1029/2002TC001464.

Fisher, D.M., Marshall, J.S., Sak, P.B., and Protti, M., 1998, Effect of subducting sea-floor roughness on fore-arc kinematics, Pacific coast, Costa Rica: Geology, v. 26, no. 5, p. 467–470.

Francis, A., 2005, Limitations of Deterministic and Inversion: CSEG Recorder, v. 5, no. February, p. 1–11.

Francis, A.M., 2003, Stochastic seismic inversion: solving large problems: International Association for Mathematical Geosciences, p. 1–2, doi: 10.1023/A:1025043530799.

Francis, A.M., 2006, Understanding stochastic inversion: Part 1: First Break, v. 24, no. 11, p. 2006.

Frisch, W., Meschede, M., and Sick, M., 1992, Origin of the Central American ophiolites : Evidence from paleomagnetic results: Geological Society of America Bulletin, v. 104, p. 1301–1314.

Furlong, K.P., Chapman, D.S., and Alfeld, P.W., 1982, Thermal modeling of the geometry of subduction with implications for the tectonics of the overriding plate: Journal of Geophysical Research Solid Earth, v. 87, no. B3, p. 1786–1802, doi: 10.1029/JB087iB03p01786.

Gardner, T.W., Marshall, J.S., Merritts, D.J., Bee, B., Burgette, R., Burton, E.O., Cooke, J., Kehrwald, N., and Protti, M., 2001, Holocene forearc block rotation in response to seamount subduction, southeastern Peninsula de Nicoya, Costa Rica: Geology, v. 29, no. 2, p. 151–154, doi: 10.1130/0091-7613(2001)029<0151:HFBRIR>2.0.CO;2.

Gardner, T.W., Verdonck, D., Pinter, N.M., Slingerland, R., Furlong, K.P., Bullard, F., and Wells, S.G., 1992, Quaternary uplift astride the aseismic Cocos Ridge, Pacific coast, Costa Rica: Geological Society of America Bulletin, v. 104, no. 2, p. 219–232.

Ghosh, A., Vidale, J.E., Sweet, J.R., Creager, K.C., Wech, A.G., Houston, H., and

Brodsky, E.E., 2010, Rapid, continuous streaking of tremor in Cascadia: Geochemistry Geophysics Geosystems, v. 11, no. 12, p. 1–10, doi: 10.1029/2010GC003305.

Haas, A., and Dubrule, O., 1994, Geostatistical inversion-a sequential method of stochastic reservoir modelling constrained by seismic data: First Break, v. 12, no. 11, p. 561–569, doi: 10.3997/1365-2397.1994034.

Hampson, D., and Russell, B., 1984, First-break interpretation using generalized linear inversion: Journal of the Canadian Society of Exploration Geophysicists, v. 20, no. 1, p. 40–54.

Harris, R.N., Sakaguchi, A., Petronotis, K., Malinverno, A., Baxter, A.T., Berg, R., Burkett, A., and Charpentier, D., 2012, Costa Rica Seismogenesis Project, Program A Stage 2 (CRISP-A2) Sampling and quantifying lithologic inputs and fluid inputs and outputs of the seismogenic zone: Proceedings of the Integrated Ocean Drilling Program, v. 344, no. December, doi: 10.2204/iodp.pr.344.2013.

Harris, R.N., Sakaguchi, A., Petronotis, K., and Scientists, I.E. 344 S., 2013a, Expedition 344 summary: Proceedings of the Integrated Ocean Drilling Program, v. 344, doi: 10.2204/iodp.proc.344.101.2013.

Harris, R.N., Sakaguchi, A., Petronotis, K., and Scientists, I.E. 344 S., 2013b, Frontal prism Site U1412: Integrated Ocean Drilling Program, v. 344, p. 1–62, doi: 10.2204/iodp.proc.344.105.2013.

Harris, R.N., Sakaguchi, A., Petronotis, K., and Scientists, I.E. 344 S., 2013c, Input Site U1414: Proceedings of the Integrated Ocean Drilling Program, v. 344, doi: 10.2204/iodp.proc.344.104.2013.

Harris, R.N., Sakaguchi, A., Petronotis, K., and Scientists, I.E. 344 S., 2013d, Mid-slope Site U1380: Proceedings of the Integrated Ocean Drilling Program, v. 344, doi: 10.2204/iodp.proc.344.106.2013.

Harris, R.N., Sakaguchi, A., Petronotis, K., and Scientists, I.E. 344 S., 2013e, Upper slope Site U1413: Proceedings of the Integrated Ocean Drilling Program, v. 344, doi: 10.2204/iodp.proc.344.107.2013.

Hey, R., 1977, Tectonic evolution of the Cocos-Nazca spreading center: Geological Society of America Bulletin, v. 88, p. 1404–1420.

Hilde, T., 1983, Sediment subduction versus accretion around the pacific: Tectonophysics, v. 99, no. 36, p. 381–397.

Van Hinte, J.E., 1978, Geohistory Analysis--Application of Micropaleontology in Exploration Geology: AAPG Bulletin, v. 62, no. 2, p. 201–222, doi: 10.1306/C1EA4815-16C9-11D7-8645000102C1865D.

Hinz, K., von Huene, R., and Ranero, C.R., 1996, Tectonic structure of the convergent Pacific margin offshore Costa Rica multichannel seismic reflection data: Tectonics, v. 15, no. 1, p. 54–66.

von Huene, R., Bialas, J., Flueh, E.R., Cropp, B., Csernok, T., Fabel, E., and Hoffman, J., 1995a, Morphotectonics of the Pacific convergent margin of Costa Rica: Spec. Pap. Geol. Soc. Am., v. 295, p. 291–308.

von Huene, R., Bialas, J., Flueh, E., Cropp, B., Csernok, T., Fabel, E., Hoffmann, J., Emeis, K., Holler, P., Jeschke, G., Leandro, C.M., Perez Fernandez, I., Chavarria, S., Florez, A.H., et al., 1995b, Morphotectonics of the Pacific convergent margin of Costa Rica: Geological Society of America Special Paper 295, p. 291–307.

von Huene, R., Langseth, M., Nasu, N., and Okada, H., 1980, 11. Summary, Japan trench transect: Initial Reports DSDP 56/57, v. 56/57, p. 473–488.

von Huene, R., and Ranero, C.R., 2003, Subduction erosion and basal friction along the sediment-starved convergent margin off Antofagasta, Chile: Journal of Geophysical Research, v. 108, no. B2, p. 2079, doi: 10.1029/2001JB001569.

von Huene, R., Ranero, C.R., and Vannucchi, P., 2004, Generic model of subduction erosion: Geology, v. 32, no. 10, p. 913–916, doi: 10.1130/G20563.1.

von Huene, R., Ranero, C.R., Weinrebe, W., and Hinz, K., 2000, Quaternary convergent margin tectonics of Costa Rica, segmentation of the Cocos Plate, and Central American volcanism: Tectonics, v. 19, no. 2, p. 314–334, doi: 10.1029/1999TC001143.

von Huene, R., and Scholl, D.W., 1991, Observations at convergent margins concerning sediment subduction, subduction erosion, and the growth of continental crust: Reviews of Geophysics, v. 29, no. 3, p. 279, doi: 10.1029/91RG00969.

Huiqi, L., McClay, K., and Powell, D., 1992, Physical models of thrust wedges: Thrust Tectonics, v. 1, p. 71–81.

Ikari, M.J., Kopf, A.J., Hüpers, A., and Vogt, C., 2018, Lithologic control of frictional strength variations in subduction zone sediment inputs: Geosphere, v. 14, no. 2, p. 604–625, doi: 10.1130/GES01546.1.

Isacks, B., and Molnar, P., 1969, Mantle Earthquake Mechanisms and the Sinking of the Lithosphere: Nature, v. 223, p. 1121–1124, doi: 10.1038/224488a0.

John, B.E., 1987, Geometry and evolution of a mid-crustal extensional fault system: Chemehuevi Mountains, southeastern California: Geological Society of London Special Publications, v. 28, p. 313–334.

Kallweit, R.S., and Wood, L.C., 1982, The limits of resolution of zero-phase wavelets: Geophysics, v. 47, no. 7, p. 1035, doi: 10.1190/1.1441367.

Karig, D.E., and Sharman, G.F., 1975, Subduction and accretion in trenches: Bulletin of the Geological Society of America, v. 86, no. 3, p. 377–389, doi: 10.1130/0016-7606(1975)86<377:SAAIT>2.0.CO;2.

Kimura, G., Silver, E.A., and Blum, P., 1997a, Leg 170: Proceedings of the Ocean Drilling Program, Initial Reports, Vol. 170, p. 7–17.

Kimura, G., Silver, E.A., and Blum, P., 1997b, Site 1042: Proceedings of the Ocean Drilling Program, v. 170, p. 189–213.

Kimura, H., Takeda, T., Obara, K., and Kasahara, K., 2010, Seismic Evidence for Active Underplating Below the Megathrust Earthquake Zone in Japan: Science, v. 329, no. July, p. 210–213.

King, E.C., Hindmarsh, R.C. a., and Stokes, C.R., 2009, Formation of mega-scale glacial lineations observed beneath a West Antarctic ice stream: Nature Geoscience, v. 2, no. 8, p. 585–588, doi: 10.1038/ngeo581.

Kirkpatrick, J.D., and Brodsky, E.E., 2014, Slickenline orientations as a record of fault rock rheology: Earth and Planetary Science Letters, v. 408, p. 24–34, doi: 10.1016/j.epsl.2014.09.040.

Kirkpatrick, J.D., Edwards, J.H., Verdecchia, A., Kluesner, J.W., Harrington, R.M., and Silver, E.A., 2018, How subduction megathrust structural variability impacts earthquakes: AGU Fall Meeting Abstracts,.

Kluesner, J.W., Silver, E.A., Bangs, N.L., McIntosh, K.D., Gibson, J.C., Orange, D., Ranero, C.R., and von Huene, R., 2013, High density of structurally controlled, shallow to deep water fluid seep indicators imaged offshore Costa Rica: Geochemistry, Geophysics, Geosystems, v. 14, no. 3, p. 519–539, doi: 10.1002/ggge.20058.

Kobayashi, D., LaFemina, P.C., Geirsson, H., Chichaco, E., Abrego, A.A., Mora, H., and Camacho, E., 2014, Kinematics of the western Caribbean: Collision of the Cocos Ridge and upper plate deformation: Geochemistry, Geophysics, Geosystems, , no. 15, p. 1671–1683, doi: 10.1002/2014GC005234.Received.

Kolla, V., Posamentier, H.W., and Eichenseer, H., 1995, Stranded parasequences and the forced regressive wedge systems tract: deposition during base-level fall - discussion: Sedimentary Geology, v. 95, no. 1–2, p. 139–145, doi: 10.1016/0037-0738(92)90052-S.

Krige, D.G., 1951, A Statistical Approach to Some Basic Mine Valuation Problems on the Witwatersrand: 159 p.

Kurzawski, R.M., Stipp, M., Niemeijer, A.R., Spiers, C.J., and Behrmann, J.H., 2016, Earthquake nucleation in weak subducted carbonates: Nature Geoscience, v. 9, no. August, p. 717–723, doi: 10.1038/NGEO2774.

Ladd, J.W., and Schroder, S., 1985, 40. Seismic stratigraphy of the continental shelf offshore Guatemala: implications for vertical tectonics related to subduction: Initial Reports DSDP 84, v. 84, p. 879–893, doi: 10.1017/CBO9781107415324.004.

LaFemina, P.C., Dixon, T.H., Govers, R., Norabuena, E., Turner, H.L., Saballos, A., Mattioli, G.S., Protti, M., and Strauch, W., 2009, Fore-arc motion and Cocos Ridge collision in Central America: Geochemistry, Geophysics, Geosystems, v. 10, no. 5, doi: 10.1029/2008GC002181.

Lallemand, S.E., and Pichon, X. Le, 1987, Coulomb wedge model applied to the subduction of seamounts in the Japan Trench: Geology, v. 15, no. November, p. 1065–1069.

Lancaster, S., and Whitcombe, D., 2000, Fast-track 'coloured' inversion: SEG Expanded Abstracts, v. 19, p. 3–6.

Lay, T., Ammon, C.J., Kanamori, H., Xue, L., and Kim, M.J., 2011, Possible large near-trench slip during the 2011 Mw 9.0 off the Pacific coast of Tohoku Earthquake: Earth, Planets and Space Letter, v. 63, p. 687–692, doi: 10.5047/eps.2011.05.033.

Lonsdale, P., 2005, Creation of the Cocos and Nazca plates by fission of the Farallon plate: Tectonophysics, v. 404, no. 3–4, p. 237–264, doi: 10.1016/j.tecto.2005.05.011.

Lonsdale, P., and Klitgord, K.D., 1978, Structure and tectonic history of the eastern Panama Basin: Geological Society of America Bulletin, v. 89, p. 981–999.

Lundberg, N., 1991, Detrital record of the early Central American magmatic arc: Petrography of intraoceanic forearc sandstones, Nicoya Peninsula, Costa Rica: Geological Society of America Bulletin, v. 103, p. 905–915.

MacMillan, I., Gans, P.B., and Alvarado, G., 2004, Middle Miocene to present plate tectonic history of the southern Central American Volcanic Arc: Tectonophysics, v. 392, no. 1–4, p. 325–348, doi: 10.1016/j.tecto.2004.04.014.

Marfurt, K.J., 2006, Robust estimates of 3D reflector dip and azimuth: Geophysics, v. 71, no. 4, p. P29–P40.

Marshall, J.S., and Anderson, R.S., 1995, Quaternary uplift and seismic cycle deformation, Peninsula de Nicoya, Costa Rica: GSA Bulletin, v. 107, p. 463–473.

Marshall, J.S., Fisher, D.M., and Gardner, T.W., 2000, Central Costa Rica deformed belt: Kinematics of diffuse faulting across the western Panama block: Tectonics, v. 19, no. 3, p. 468–492, doi: 10.1029/1999TC001136.

Marshall, J.S., Idleman, B.D., Gardner, T.W., and Fisher, D.M., 2003, Landscape evolution within a retreating volcanic arc, Costa Rica,Central America: Geology, v. 31, no. 5, p. 419–422, doi: Doi 10.1130/0091-7613(2003)031<0419:Lewarv>2.0.Co;2.

Martinod, J., Guillaume, B., Espurt, N., Faccenna, C., Funiciello, F., and Regard, V., 2013, Effect of aseismic ridge subduction on slab geometry and overriding plate deformation : Insights from analogue modeling: Tectonophysics, v. 588, p. 39–55, doi: 10.1016/j.tecto.2012.12.010.

Masson, D.G., 1991, Fault patterns at outer trench walls: Marine Geophysical Researches, v. 13, no. 3, p. 209–225, doi: 10.1007/BF00369150.

Matheron, G., 1963, Principles of geostatistics: Economic Geology, v. 58, p. 1246–1266.

McIntosh, K.D., and Silver, E.A., 1996, Using 3D seismic reflection data to find fluid seeps from the Costa Rica Accretionary Prism: Geophysical Research Letters, v. 23, no. 8, p. 895, doi: 10.1029/95GL02010.

McIntosh, K.D., Silver, E.A., and Shipley, T.H., 1993, Evidence and mechanisms for forearc extension at the accretionary Costa Rica convergent margin: Tectonics, v. 12, no. 6, p. 1380–1392.

Means, W.D., 1987, A newly recognized type of slickenside striation: Journal of Structural Geology, v. 9, no. 5, p. 585–590.

Meschede, M., Barckhausen, U., and Worm, H.U., 1998, Extinct spreading on the Cocos Ridge: Terra Nova, v. 10, no. 1977, p. 211–216, doi: 10.1046/j.1365-3121.1998.00195.x.

Moore, G.F., and Shipley, T.H., 1988, Mechanisms of Sediment Accretion in the Middle America Trench off Mexico: Journal of Geophysical Research, v. 93, no. 7, p. 8911–8927.

Moore, G.F., Shipley, T.H., and Lonsdale, P., 1986, Subduction erosion versus sediment offscraping at the toe of the Middle America off Guatemala: Tectonics, v. 5, no. 4, p. 513–523.

Moore, J.C., and Silver, E.A., 1987, Continental margin tectonics: submarine accretionary prisms: Reviews of Geophysics, v. 25, no. 6, p. 1305–1312.

Moore, J.C., and Vrolijk, P., 1992, Fluids in accretionary prisms: Reviews of Geophysics, v. 30, p. 113–135, doi: 10.1029/90EO00031.

Morell, K.D., 2015, Late Miocene to recent plate tectonic history of the southern Central America convergent margin: Geochemistry Geophysics Geosystems, p. 3362–3382, doi: 10.1002/2015GC005971.Received.

Morell, K.D., 2016, Seamount, ridge and transform subduction in southern Central

America: Tectonics, , no. 4, p. 357–385, doi: 10.1002/2015TC003950.

Morell, K.D., Fisher, D.M., and Gardner, T.W., 2008, Inner forearc response to subduction of the Panama Fracture Zone, southern Central America: Earth and Planetary Science Letters, v. 265, no. 1–2, p. 82–95, doi: 10.1016/j.epsl.2007.09.039.

Morell, K.D., Fisher, D.M., Gardner, T.W., LaFemina, P.C., Davidson, D., and Teletzke, A., 2011, Quaternary outer fore-arc deformation and uplift inboard of the Panama Triple Junction, Burica Peninsula: Journal of Geodynamics, v. 116, p. 1–24, doi: 10.1029/2010JB007979.

Morell, K.D., Gardner, T.W., Fisher, D.M., Idleman, B.D., and Zellner, H.M., 2013, Active thrusting, landscape evolution, and late Pleistocene sector collapse of Barú Volcano above the Cocos-Nazca slab tear, southern Central America: Geological Society of America Bulletin, v. 125, no. 7, p. 1301–1318, doi: 10.1130/B30771.1.

Morell, K.D., Kirby, E., Fisher, D.M., and Van Soest, M., 2012, Geomorphic and exhumational response of the Central American Volcanic Arc to Cocos Ridge subduction: Journal of Geophysical Research: Solid Earth, v. 117, no. 4, doi: 10.1029/2011JB008969.

Morris, J., Villinger, H.W., and Klaus, A., 2003, Leg 205 Summary: Proceedings of the Ocean Drilling Program, Initial Reports Volume 205,.

Pardo-Igúzquiza, E., and Chica-Olmo, M., 1993, The Fourier Integral Method: An efficient spectral method for simulation of random fields: Mathematical Geology, v. 25, no. 2, p. 177–217, doi: 10.1007/BF00893272.

Petit, J.P., 1987, Criteria for the sense of movement on fault surfaces in brittle rocks: Journal of Structural Geology, v. 9, no. 5, p. 597–608.

Pindell, J.L., and Barrett, S.F., 1990, Geological evolution of the Caribbean region; A plate-tectonic perspective:

Rafaelsen, B., Andreassen, K., Kuilman, L.W., Lebesbye, E., Hogstad, K., and Midtbo, M., 2002, Geomorphology of buried glacigenic horizons in the Barents Sea from three-dimensional seismic data: Geological Society of America, Special Publications, v. 203, p. 259–276.

Ranero, C.R., Grevemeyer, I., Sahling, H., Barckhausen, U., Hensen, C., Wallmann, K., Weinrebe, W., Vannucchi, P., von Huene, R., and McIntosh, K.D., 2008, Hydrogeological system of erosional convergent margins and its influence on tectonics and interplate seismogenesis: Geochemistry, Geophysics, Geosystems, v. 9, no. 3, doi: 10.1029/2007GC001679.

Ranero, C.R., and von Huene, R., 2000, Subduction erosion along the Middle

America convergent margin: Nature, v. 404, no. 6779, p. 748–752, doi: 10.1038/35008046.

Regalla, C., Fisher, D.M., Kirby, E., and Furlong, K.P., 2013, Relationship between outer forearc subsidence and plate boundary kinematics along the Northeast Japan convergent margin: Geochemistry, Geophysics, Geosystems, v. 14, no. 12, p. 5227–5243, doi: 10.1002/2013GC005008.

Roberts, A., 2001, Curvature Attributes and their Application to 3D Interpreted Horizons: First Break, v. 19, no. 2, p. 85–100.

Rubin, A.M., Gillard, D., and Got, J., 1999, Streaks of microearthquakes along creeping faults: Nature, v. 400, no. AUGUST, p. 635–641.

Rutland, R.W.R., 1971, Andean orogeny and ocean floor spreading: Nature, v. 233, no. September 24, p. 252–255.

Sagy, A., Brodsky, E.E., and Axen, G.J., 2007, Evolution of fault-surface roughness with slip: Geology, v. 35, no. 3, p. 283–286, doi: 10.1130/G23235A.1.

Sak, P.B., Fisher, D.M., and Gardner, T.W., 2004, Effects of subducting seafloor roughness on upper plate vertical tectonism: Osa Peninsula, Costa Rica: Tectonics, v. 23, p. 1–16, doi: 10.1029/2002TC001474.

Sak, P.B., Fisher, D.M., Gardner, T.W., Marshall, J.S., and LaFemina, P.C., 2009, Rough crust subduction, forearc kinematics, and Quaternary uplift rates, Costa Rican segment of the Middle American Trench: Bulletin of the Geological Society of America, v. 121, no. 7–8, p. 992–1012, doi: 10.1130/B26237.1.

Sallarès, V., 2003, Seismic structure of Cocos and Malpelo Volcanic Ridges and implications for hot spot-ridge interaction: Journal of Geophysical Research, v. 108, no. B12, p. 1–21, doi: 10.1029/2003JB002431.

Scholl, D.W., and von Huene, R., 2009, Implications of estimated magmatic additions and recycling losses at the subduction zones of accretionary (non-collisional) and collisional (suturing) orogens: Geological Society, London, Special Publications, v. 318, no. 1, p. 105–125, doi: 10.1144/SP318.4.

Scholz, C.H., 2002, The mechanics of earthquakes and faulting: Cambridge University Press, p. 496.

Seely, D.R., Vail, P.R., and G., W.G., 1974, Trench Slope Model: The Geology of Continental Margins, p. 249–259.

Shi, Z., and Day, S.M., 2013, Rupture dynamics and ground motion from 3-D rough-fault simulations: Journal of Geophysical Research, v. 118, p. 1122–1141, doi: 10.1002/jgrb.50094.

Shipley, T.H., McIntosh, K.D., Silver, E.A., and Stoffa, P.L., 1992, Three-dimensional seismic imaging of the Costa Rica accretionary prism: Structural diversity in a small volume of the lower slope: Journal of Geophysical Research, v. 97, no. B4, p. 4439, doi: 10.1029/91JB02999.

Shipley, T.H., and Moore, G.F., 1986, Sediment Accretion, Subduction, and Dewatering at the Base of the Trench Slope Off Costa Rica: A Seismic Reflection View of the Decollement: Journal of Geophysical Research, v. 91, p. 2019–2028.

Shipley, T.H., Stoffa, P.L., and Dean, D.F., 1990, Underthrust sediments, fluid migration paths, and mud volcanoes associated with the accretionary wedge off Costa Rica Middle America Trench: Journal of Geophysical Research, v. 95, p. 8743–8752.

Silver, E.A., 2000, Leg 170: Synthesis of fluid-structural relationships of the Pacific Margin of Costa Rica: Proceedings of the Ocean Drilling Program, Scientific Results Volume 205, v. 170, p. 1–11.

Silver, E.A., 1971, Transitional Tectonics and Late Cenozoic Structure of the Continental Margin off Northernmost California: Geological Society of America Bulletin, v. 82, p. 1–22.

Silver, E.A., Ellis, M.J., Breen, N.A., and Shipley, T.H., 1985, Comments on the growth of accretionary wedges: Geology, v. 13, p. 6–9.

Silver, E.A., Reed, D.L., Tagudin, J.E., and Heil, D.J., 1990, Implications of the North and South Panama Thrust Belts for the origin of the Panama Orocline: Tectonics, v. 9, no. 2, p. 261–281.

Sitchler, J.C., Fisher, D.M., Gardner, T.W., and Protti, M., 2007, Constraints on inner forearc deformation from balanced cross sections, Fila Costena thrust belt, Costa Rica: Tectonics, v. 26, no. 6, p. 1–11, doi: 10.1029/2006TC001949.

Stavenhagen, A., Flueh, E.R., Ranero, C.R., McIntosh, K.D., Shipley, T.H., Leandro, G., Schulze, A., and Danobeitia, J., 1997, Seismic wide-angle investigations in Costa Rica - a crustal velocity model from the Pacific to the Caribbean coast: Zbl. Geol. Palaont. Teil I, v. H. 3-6, p. 393–408.

Stern, C.R., 2011, Subduction erosion: Rates, mechanisms, and its role in arc magmatism and the evolution of the continental crust and mantle: Gondwana Research, v. 20, no. 2–3, p. 284–308, doi: 10.1016/j.gr.2011.03.006.

Stern, R.J., and Scholl, D.W., 2010, Yin and yang of continental crust creation and destruction by plate tectonic processes: International Geology Review, v. 52, no. 1, p. 1–31, doi: 10.1080/00206810903332322.

Stoffa, P.L., Shipley, T.H., Kessinger, W., Dean, D.F., Elde, R., Silver, E.A., Reed, D.L., and Aguilar, A., 1991, Three-Dimensional Seismic Imaging of the Costa

Rica Accretionary Prism: Field Program and Migration Examples: Journal of Geophysical Research, v. 96, p. 21693–21712.

Suess, E., and von Huene, R., 1988, 1. Introduction, Objectives, and Principal Results Leg 112, Peru Continental Margin: Initial Reports DSDP 112, p. 5–23.

Tingdahl, K.M., and de Groot, P., 2003, Post-stack dip- and azimuth processing: Journal of Seismic Exploration, v. 12, p. 113–126.

Tobin, H.J., Vannucchi, P., and Meschede, M., 2001, Structure, inferred mechanical properties, and implications for fluid transport in the decollement zone, Costa Rica convergent margin: Geology, v. 29, no. 10, p. 907–910, doi: 10.1130/0091-7613(2001)029<0907:SIMPAI>2.0.CO;2.

Tucholke, B.E., Lin, J., and Kleinrock, M.C., 1998, Megamullions and mullion structure defining oceanic metamorphic core complexes on the Mid-Atlantic Ridge: Journal of Geophysical Research, v. 103, p. 9857–9866.

Vail, P.R., and Mitchum, R.M., 1977, Seismic Stratigraphy and Global Changes of Sea Level , Part 1 : Seismic Stratigraphy - Application to Hydrocarbon Exploration: AAPG Memoir 26, p. 51–52.

Vail, P.R., Todd, R.G., and Sangree, J.B., 1977, Seismic stratigraphy and global changes of sea level, Part 5: chronostratigraphic significance of seismic reflections: Seismic Stratigraphy — Applications to Hydrocarbon Exploration, p. 99–116.

Vannucchi, P., Galeotti, S., Clift, P.D., Ranero, C.R., and von Huene, R., 2004, Long-term subduction-erosion along the Guatemalan margin of the Middle America Trench: Geology, v. 32, no. 7, p. 617–620, doi: 10.1130/G20422.1.

Vannucchi, P., Morgan, J.P., Silver, E.A., and Kluesner, J.W., 2016, Origin and dynamics of depositionary subduction margins: Geochemistry Geophysics Geosystems, v. 17, p. 1966–1974, doi: 10.1002/2016GC006406.

Vannucchi, P., Ranero, C.R., Galeotti, S., Straub, S.M., Scholl, D.W., and McDougall-Reid, K., 2003, Fast rates of subduction erosion along the Costa Rica Pacific margin: Implications for nonsteady rates of crustal recycling at subduction zones: Journal of Geophysical Research, v. 108, no. B11, p. 1–13, doi: 10.1029/2002JB002207.

Vannucchi, P., Sak, P.B., Morgan, J.P., Ohkushi, K., Ujiie, K., and Scientists, I.E. 334 S., 2013, Rapid pulses of uplift, subsidence, and subduction erosion offshore Central America: Implications for building the rock record of convergent margins: Geology, v. 41, p. 995–998, doi: 10.1130/G34355.1.

Vannucchi, P., Scholl, D.W., Meschede, M., and McDougall-Reid, K., 2001, Tectonic erosion and consequent collapse fo the Pacific margin of Costa Rica: Combined implications from ODP Leg 170, seismic offshore data, and regional geology of the Nicoya Peninsula: Tectonics, v. 20, no. 5, p. 649–668.

Vannucchi, P., Stroncik, N., Malinverno, A., and Scientists, I.E. 334 S., 2012, Site U1379: Integrated Ocean Drilling Program, v. 334, p. 1–83, doi: 10.2204/iodp.proc.334.104.2012.

Vannucchi, P., Ujiie, K., and Scientists, I.E. 334 S., 2011, Costa Rica Seismogenesis Project (CRISP) Sampling and quantifying input to the seismogenic zone and fluid output: Integrated Ocean Drilling Program, p. 1–78, doi: 10.2204/iodp.pr.334.2011.

Wang, K., and Bilek, S.L., 2011, Do subducting seamounts generate or stop large earthquakes? Geology, v. 39, no. 9, p. 819–822, doi: 10.1130/G31856.1.

Wang, K., and Hu, Y., 2006, Accretionary prisms in subduction earthquake cycles: The theory of dynamic Coulomb wedge: Journal of Geophysical Research: Solid Earth, v. 111, no. 6, p. 1–16, doi: 10.1029/2005JB004094.

White, R., and Simm, R., 2003, Tutorial: Good practice in well ties: First Break, v. 21, no. 10, p. 75–83.

Wright, L.A., Otton, J.K., and Troxel, B.W., 1974, Turtleback Surfaces of Death Valley Viewed as Phenomena of Extensional Tectonics: Geology, p. 53–54.

Ye, S., Bialas, J., Flueh, E.R., Stavenhagen, A., von Huene, R., and Leandro, G., 1996, Crustal structure of the Middle American Trench off Costa Rica from wide-angle seismic data: Tectonics, v. 15, no. 5, p. 1006–1021.

Yilmaz, O., 2001, Seismic Data Analysis: Processing, Inversion, and Interpretation of Seismic Data: Society of Exploration Geophysicists, v. 1, no. 10, p. 157.

Zeumann, S., and Hampel, A., 2015, Deformation of erosive and accretive forearcs during subduction of migrating and non-migrating aseismic ridges: Results from 3-D finite element models and application to the Central American, Peruvian, and Ryukyu margins: Tectonics, v. 26, no. March 2013, p. 6–9, doi: 10.1002/2015TC003867.